

**IMPROVED FLUORESCENCE-ENHANCED OPTICAL IMAGING  
AND TOMOGRAPHY BY ENHANCED EXCITATION LIGHT  
REJECTION**

A Dissertation

by

KIL DONG HWANG

Submitted to the Office of Graduate Studies of  
Texas A&M University  
in partial fulfillment of the requirements for the degree of

DOCTOR OF PHILOSOPHY

December 2006

Major Subject: Chemical Engineering

**IMPROVED FLUORESCENCE-ENHANCED OPTICAL IMAGING  
AND TOMOGRAPHY BY ENHANCED EXCITATION LIGHT  
REJECTION**

A Dissertation

by

KIL DONG HWANG

Submitted to the Office of Graduate Studies of  
Texas A&M University  
in partial fulfillment of the requirements for the degree of

DOCTOR OF PHILOSOPHY

Approved by:

Chair of Committee, Eva M. Sevick-Muraca

Committee Members, Daniel F. Shantz

Mahmoud El-Halwagi

Friedhelm Schroeder

Head of Department, Nagamangala K. Anand

December 2006

Major Subject: Chemical Engineering

## ABSTRACT

Improved Fluorescence-enhanced Optical Imaging and Tomography by Enhanced  
Excitation Light Rejection.

(December 2006)

Kil Dong Hwang, B.S., Chung-Ang University, Korea

Chair of Advisory Committee: Dr. Eva M. Sevick-Muraca

Fluorescence enhanced optical imaging and tomography studies involve the detection of weak fluorescent signals emanating from nano- to picomolar concentrations of exogenous or endogenously produced fluorophore concurrent with the rejection of an overwhelmingly large component of backscattered excitation light. The elimination of the back-reflected excitation light of the collected signal remains a major and often unrecognized challenge for further reducing the noise floor and increasing sensitivity of small animal fluorescence imaging.

In this dissertation, we adapted collimating and gradient index (GRIN) lenses in an existing frequency-domain system to improve excitation light rejection and enhance planar and tomographic imaging. To achieve this goal, we developed planar and tomographic imaging systems based upon ray tracing calculations for improved rejection of excitation light. The “out-of-band ( $S(\lambda_x)$ )” to “in-band ( $S(\lambda_m) - S(\lambda_x)$ )” signal ratio assessing excitation leakage was acquired with and without collimating optics. The addition of collimating optics resulted in a 51 to 75% reduction in the transmission ratio

of  $(S(\lambda_x)/ (S(\lambda_m) - S(\lambda_x)))$  for the phantom studies and an increase of target to background ratio (TBR) from 11% to 31% in animal studies. Additionally, we presented results demonstrating the improvement of model match between experiments and forward simulation models by adaptation of GRIN lens optics to a breast phantom study. In particular, 128 GRIN lenses on the fiber bundle face were employed to align the collected excitation and emission light normal to the filter surface in an existing frequency-domain system. As a result of GRIN lens collimation, we reduced the transmission ratio between 10 and 86 % and improved the model match for tomographic reconstruction of one ( $1 \text{ cm}^3$ ) and two ( $0.1 \text{ cm}^3$ ) targets in a  $1087 \text{ cm}^3$  of breast phantom.

Ultimately, this work improves the sensitivity of NIR fluorescence imaging by enhancing the rejection of excitation light and shows that the current sensitivity challenges for translating fluorescence-enhanced optical imaging into the clinic can be overcome.

**To my wife**

## ACKNOWLEDGEMENTS

This dissertation owes its successful completion to many people. Most of all, Dr. Eva M. Sevick-Muraca was not only my research advisor but also a role model for my academic growth. Specifically, she kept showing her faith in my ideas, teaching the timeless lessons of ethics, leadership, and teamwork. Help and support from John Rasmussen and Dr. Jessica Houston during the instrumentation set-up is unforgettable. Great advice from the tomography group, Dr. Amit Joshi, Dr. Jaehoon Lee, Dr. Ranadhir Roy, and Amit Sahu, in understanding forward simulation was invaluable. Discussion with Dr. Tianshu Pan was useful and greatly helpful in resolving my research gridlock. The encouragement and positive remarks provided by Feng Liang, Dr. Sarabjot Dali, Dr. Kristen Adams, Ruchi Sharma, Lakshmi Sampath, Sunkuk Kwon and other members of the Frenslay Molecular Imaging Center have been a great support.

My lovely daughter, Sarah, gave me such delight every day with her unexpected features and smiling face. I don't know how to express my gratitude to my honey, Dawoon. She was always with me when I lost courage and was having a hard time in life.

I thank my committee members, Dr. Daniel Shantz, Dr. Mahmoud El-Halwagi, and Dr. Friedhelm Schroeder, for reviewing this dissertation and providing helpful comments. I am grateful to Dr. Barbara Atshaves for agreeing to substitute for Dr. Friedhelm Schroeder at short notice. I would like to acknowledge the National Institute of Health (R01 CA112679) for funding my research. Finally, I really thank God for his endless love and enabling me to study in the USA.

## TABLE OF CONTENTS

	Page
ABSTRACT .....	iii
ACKNOWLEDGEMENTS .....	vi
TABLE OF CONTENTS .....	vii
LIST OF FIGURES .....	x
LIST OF TABLES .....	xiv
NOMENCLATURE .....	xvi
1. INTRODUCTION.....	1
1.1 Significance.....	5
2. BACKGROUND.....	6
2.1 Fluorescence enhanced optical imaging.....	7
2.1.1 Measurement techniques .....	9
2.1.2 Light propagation model using diffusion equation .....	11
2.1.3 Tomographic imaging (point source and point collection) .....	14
2.1.4 Planar imaging (area illumination and collection) .....	17
2.2 Excitation light leakage and optical filter performance .....	17
2.2.1 Problem of excitation light leakage.....	17
2.2.2 Angle of incidence and filter performance.....	19
2.2.3 Collimating lens and Gradient index (GRIN) lens.....	20
3. ENHANCED FLUORESCENT OPTICAL IMAGING WITH IMPROVED EXCITATION LIGHT REJECTION: PLANAR IMAGING .....	22
3.1 Introduction .....	22
3.2 Materials and methods .....	28
3.2.1 Phantom studies.....	28
3.2.2 Animal studies.....	28
3.2.3 Instrumentation.....	29
3.2.4 Analysis of FDPM measurements.....	31
3.2.5 Selection of optical filters and collimating optics .....	31

	Page
3.2.6 Experimental design and analysis .....	35
3.3 Results .....	36
3.3.1 Phantom studies.....	36
3.3.2 Images collected from molecularly targeted agents in animals .....	38
3.4 Discussion .....	40
4. INFLUENCE OF EXCITATION LIGHT REJECTION ON FORWARD MODEL MISMATCH IN OPTICAL TOMOGRAPHY: TOMOGRAPHIC IMAGING .....	44
4.1 Introduction .....	44
4.2 Materials and methods .....	48
4.2.1 Breast phantom.....	48
4.2.2 Instrumentation.....	51
4.2.3 Fiber calibration .....	54
4.2.4 Assessment of excitation light leakage .....	54
4.2.5 Assessment of model mismatch errors.....	55
4.3 Results and discussion.....	56
4.3.1 Influence of fiber length.....	56
4.3.2 Transmission ratio .....	58
4.3.3 Model mismatch errors.....	60
4.4 Summary .....	71
5. IMPROVEMENT OF MODEL MATCH IN TWO HETEROGENEITY SYSTEMS.....	73
5.1 Introduction .....	73
5.2 Materials and methods .....	74
5.2.1 Phantom and instrumentation.....	74
5.2.2 The forward problem.....	77
5.3 Results and discussion.....	77
6. CONCLUSIONS AND SUGGESTED FUTURE WORK .....	89
REFERENCES.....	93
APPENDIX A FDPM INSTRUMENTATION .....	107
APPENDIX B SOURCE AND COLLECTION FIBER LOCATIONS ON BREAST PHANTOM .....	113
APPENDIX C RAY TRACING OF GRIN LENS - DETECTOR FIBERS FOR BREAST PHANTOM SYSTEM .....	117



	Page
APPENDIX D SLOPES AND CORRELATION FACTORS OF LINEAR REGRESSION FOR THE MISMATCH ERRORS.....	121
APPENDIX E TRANSMISSION RATIO FOR 26 SOURCES .....	122
APPENDIX F RAYLEIGH RESOLUTION .....	154
VITA.....	155

## LIST OF FIGURES

	Page
Figure 1 Organization of dissertation.....	4
Figure 2 Schematic of the fluorescence-enhanced imaging process in a tissue medium (left) and its potential future clinical application (right) <sup>25</sup> .....	6
Figure 3 Schematic of optical imaging process using different measurement techniques (a) time domain photon migration, (b) frequency domain photon migration, and (c) continuous wave imaging.....	9
Figure 4 Schematic of different measurement geometries (a) point illumination and point collection and (b) area illumination and area collection geometry.....	15
Figure 5 Basic structure of a model based tomographic reconstruction scheme <sup>42</sup> .....	16
Figure 6 (a) Optical density of 830nm interference filter as a function of incident angle, (b) optical density of Kaiser Holographic filter as a function of incident angle <sup>52</sup> .....	19
Figure 7 Schematic of FDPM measurements used in NIR optical spectroscopy and tomography.....	30
Figure 8 Experimental setup employed for the improvement of excitation light leakage (a) with collimating optics and (b) without collimating optics. Numbered components include: (1) CCD camera, (2) laser diode, (3) image intensifier, (4) Holographic filter, (5) collimating lens, (6) Bandpass filter, (7) collimating lens, and (8) Holographic filter. $\theta$ represents angle of incidence on the filter plane.....	33
Figure 9 Transmission ratio of DC intensity ( $R(I_{DC})$ ) (a) and AC amplitude( $R(I_{AC})$ ) (b) computed from filter combination (holographic-bandpass-holographic filters) as a function of $r$ , the distance from the center of photocathode. Black and white bars indicate out-of-band to in-band ratio of imaging system with and without collimating optics respectively. Error bars represent standard deviations of intensity with region of interest.....	37
Figure 10 $I_{AC}$ image of an animal bearing 5mm diameter glioma lesion (a) with and (b) without collimating optics. $I_{DC}$ image of an animal bearing 5mm diameter glioma lesion (c) with and (d) without collimating optics. Color bars represented raw signals without referencing.....	38

- Figure 11 (a) 3D tissue-mimicking breast phantom and dimensions of the cup-shaped phantom; (b) x-y location of all 26 point illumination (filled circles) and 128 collection fiber locations (open circles) on the hemispherical portion of the breast phantom. S# and d# represent source and detector number respectively. Arrows (triangle) indicate numbering direction (counter-clockwise) of 128 collection fibers; (c) fiber bundle without grin lenses which was imaged onto the photocathode of the image intensifier. ....48
- Figure 12 Instrumentation set-up of the tomographic imaging system and phantom. ....53
- Figure 13 (a) Correlation of  $RPS_{error,i}$  from 1% liposyn versus that of 0.5% for the confirmation of systematic offset on breast phantom system. Comparison of RPS before (unfilled circles) and after (filled circles) fiber calibration as a function of collection fiber location based on a source position (source number 9). The dotted line represent RPS of forward model. Results are presented for data collected with GRIN lenses. ....57
- Figure 14 Comparison of transmission ratio with ((a),(c)) and without ((b),(d)) GRIN lens for  $I_{AC}$  ((a),(b)) and  $I_{DC}$  ((c),(d)) measurements based on a source position (source number 9). Filled and unfilled bars represent the transmission ratio with and without GRIN lens respectively. Error bars represent the standard deviation of transmission ratio with region of the collection fiber. ....58
- Figure 15 Comparison of amplitude ratio (ACR) ((a),(c),(e)) and relative phase difference (RPS) ((b),(d),(f)) between measurements (symbols) and forward model (dotted line) for a source location (source number 9) as a function of fiber position. The filled circles denote measurements with GRIN lenses while the unfilled symbols denote those without. Target centroid depth varied from 1.26 cm ((a), (b)), 2 cm ((c), (d)), and 3 cm ((e), (f)) at  $1 \mu M$  of target concentration. ....61
- Figure 16 Comparison of mean of ACR ((a)) and RPS ((b)) errors between with and without GRIN lens as a function of target depth. Filled and unfilled circles correspond to the mean mismatch errors with and without GRIN lens respectively. Error bars represent the standard deviation of mean mismatch errors. ....63
- Figure 17 Comparison of amplitude ratio (ACR) ((a),(c),(e)) and relative phase difference (RPS) ((b),(d),(f)) between measurements (symbols) and forward model (dotted line) for a source location (source number 9) as a function of

fiber position. The filled circles denote measurements with GRIN lenses while the unfilled symbols denote those without. Target ICG concentration varied to 1 $\mu\text{M}$ ((a), (b)), 0.5 $\mu\text{M}$ ((c), (d)), and 0.25 $\mu\text{M}$ ((e), (f)) at 1.26 cm of target depth.....	67
Figure 18 Comparison of mean summation of ACR ((a)) and RPS ((b)) errors between with and without GRIN lens as a function of target concentration. Filled and unfilled circles correspond to the mean mismatch errors with and without GRIN lens respectively. Error bars represent the standard deviation of mean mismatch errors.....	69
Figure 19 x-y location of all 26 point illumination (black circles), 128 collection fiber locations (open circles), and two target locations (green circles) on the hemispherical portion of the breast phantom. Center to center separations of targets are 2.45 (a), 2.0 (b), and 1.0 cm (c). S# and d# represent source and collection fiber number respectively. Arrows (triangle) indicate numbering direction (counter-clockwise) of 128 collection fibers. ....	75
Figure 20 Comparison of amplitude ratio (ACR) ((a),(c),(e)) and relative phase difference (RPS) ((b),(d),(f)) between measurements (symbols) and forward model (dotted line) for two target system as a function of fiber position.. The filled circles denote measurements with GRIN lenses while the unfilled symbols denote those without. Target centroid depth varied from 1.26 cm ((a), (b)), 2.0 cm ((c), (d)), and 2.55 cm ((e), (f)) at 2.45 cm of target to target distance.....	78
Figure 21 Comparison of mean of ACR ((a),(c), and (e)) and RPS ((b),(d), and (f)) errors between with and without GRIN lens as a function of target depth for 2.45 ((a),(b)), 2.0 ((c),(d)), and 1 cm ((e),(f)) of target to target separation. Filled and unfilled circles correspond to the mean mismatch errors with and without GRIN lenses respectively. Error bars represent the standard deviation of mean mismatch errors.....	80
Figure A1 FDPM instrumentation for fluorescence enhanced optical imaging.....	107
Figure A2 Transmission curve of holographic filter (a) and 830 nm interference filter (b) at zero incident angle.....	109
Figure A3 Calculation of incident angle to the GRIN lens from an optical fiber. $n_i$ , $\theta_{\text{max}}$ , and $\theta_t$ represent the refractive index of the 1% liposyn solution, maximum half of angle of incident light to the optical fiber from the 1% liposyn solution in breast phantom, and maximum incident angle to the GRIN lens respectively. ....	117

	Page
Figure A4 Ray height (r)(a) and gradient ( $\Phi$ )(b) through ray tracing calculation of the GRIN as a function of lens length (z).....	120
Figure A5 Definition of lateral resolution using Rayleigh's criterion <sup>53</sup> .....	154

## LIST OF TABLES

	Page
Table 1 Review of literature for efficient collection of fluorescence signal in phantom and animal studies.....	25
Table 2 Comparison of TBR of $I_{AC}$ and $I_{DC}$ images with and without collimation .....	39
Table 3 Comparison of SNR of average $I_{AC}$ and $I_{DC}$ images with and without collimation.....	39
Table 4 Literature review of application of GRIN lens to optical imaging and sensing system.....	47
Table 5 Mean summation of ACR and RPS errors of 128 detectors with GRIN lens as a function of target depth for 26 sources with GRIN lens .....	64
Table 6 Mean summation of ACR and RPS errors of 128 detectors without GRIN lens as a function of target depth for 26 sources without GRIN lenses .....	65
Table 7 Mean summation of ACR and RPS errors with GRIN lens as a function of target concentration for 26 sources with GRIN lenses.....	69
Table 8 Mean summation of ACR and RPS errors without GRIN lens as a function of target concentration for 26 sources without GRIN lenses.....	70
Table 9 $(x,y,z)$ coordinates of two targets.....	76
Table 10 Mean summation of ACR and RPS errors of 128 collection fibers with GRIN lenses as a function of target depth for 26 sources. (Target to target separation: 2.45 cm) .....	83
Table 11 Mean summation of ACR and RPS errors of 128 collection fibers without GRIN lenses as a function of target depth for 26 sources. (Target to target separation: 2.45 cm) .....	84
Table 12 Mean summation of ACR and RPS errors of 128 collection fibers with GRIN lenses as a function of target depth for 26 sources. (Target to target separation: 2.0 cm) .....	85

	Page
Table 13 Mean summation of ACR and RPS errors of 128 collection fibers without GRIN lenses as a function of target depth for 26 sources. (Target to target separation: 2.0 cm) .....	86
Table 14 Mean summation of ACR and RPS errors of 128 collection fibers with GRIN lenses as a function of target depth for 26 sources. (Target to target separation: 1.0 cm) .....	87
Table 15 Mean summation of ACR and RPS errors of 128 collection fibers without GRIN lenses as a function of target depth for 26 sources. (Target to target separation: 1.0 cm) .....	88

## NOMENCLATURE

### Abbreviations

2-D	Two-dimension
3-D	Three-dimension
ACR	Amplitude ratio
AOI	Angle of incidence
CCD	Charge coupled device
CT	Computed tomography
CW	Continuous wave
FDA	Food and Drug Administration
FDPM	Frequency domain photon migration
FFT	Fast Fourier Transform
FOV	Field of View
FWHM	Full width at half maximum
GRIN	Gradient index
ICCD	Intensified charge coupled device
ICG	Indocyanine green
MRI	Magnetic resonance imaging
NA	Numerical aperture
NIR	Near infrared
OD	Optical density
PET	Positron emission tomography
PMT	Photomultiplier Tube
RF	Radio frequency
RGD	Arginine-glycine-aspartic acid
ROI	Region of interest
RPS	Relative phase difference
SNR	Signal to noise ratio
SPECT	Single photon emission computed tomography



## Symbols

$\sigma_B$	Standard deviation of background signals
$D_x$	Optical diffusion coefficient at excitation wavelength
$A$	GRIN lens constant ( $\text{mm}^{-2}$ )
$\text{ACR}_{\text{error, sum}}$	Model mismatch error of ACR ACR value obtained from measurements
$\text{ACR}_{\text{exp},i}$	at collection fiber $i$ ACR value obtained from forward model
$\text{ACR}_{\text{sim},i}$	at collection fiber $i$
$B$	Background signal
$C$	Contrast
$c_m$	Velocity of light at emission wavelength
$c_x$	Velocity of light at excitation wavelength
$\delta$	Phase-delay relative to the incident light
$D_m$	Optical diffusion coefficient at emission wavelength
$\phi$	Quantum efficiency
$\gamma$	Index mismatch parameter
$g$	Anisotropy coefficient
$I_{\text{AC}}$	AC amplitude
$I_{\text{DC}}$	DC intensity
$\lambda$	Wavelength
$n_{\text{max}}$	Refractive index of the GRIN lens axis
$r$	Positional vector at given point
$R(I_{\text{AC}})$	Transmission ratio of AC amplitude
$R(I_{\text{DC}})$	Transmission ratio of DC intensity
$r_d$	Positional vector at the collection point
$\text{RPS}_{\text{exp},i}$	RPS value obtained from measurements at collection fiber $i$
$\text{RPS}_{\text{sim},i}$	RPS value obtained from forward model at collection fiber $i$
$\text{RPS}_{\text{error, sum}}$	Model mismatch error of RPS
$r_s$	Positional vector at the illumination point
$S$	Object distance
$S(\lambda_m)$	Average pixel intensity values associated with

	the measurements taken in the presence of ICG
$S(\lambda_x)$	Average pixel intensity values associated with the measurements taken in the absence of ICG
$S'$	Image distance
$SNR_c$	SNR with collimating lens
$SNR_{nc}$	SNR without collimating lens
$\tau$	Fluorescence lifetime (sec)
$T$	Target signal
$TBR_c$	TBR with collimating lens
$TBR_{nc}$	TBR without collimating lens
$\omega$	Modulation frequency (radians)
$\mu_a$	Absorption coefficient ( $\text{cm}^{-1}$ )
	Absorption coefficient due to fluorophore at emission wavelength
$\mu_{amf}$	Absorption coefficient due to chromophore at emission wavelength
$\mu_{ami}$	Absorption coefficient due to fluorophore at excitation wavelength
$\mu_{axf}$	Absorption coefficient due to chromophore at excitation wavelength
$\mu_{axi}$	Scattering coefficient ( $\text{cm}^{-1}$ )
$\mu_s$	Isotropic scattering coefficient ( $\text{cm}^{-1}$ )
$\mu_s'$	AC component of fluence at emission wavelength
$\Phi_m$	AC component of fluence at excitation wavelength
$\Phi_x$	Standard error of estimation for linear regression
$\hat{\sigma}^2$	

## 1. INTRODUCTION

With the advent of post genomics era<sup>1</sup>, molecular imaging in measurement and characterization of biological processes at the cellular and molecular level has become possible. Molecular imaging is defined as the non-invasive visualization, characterization and quantification of physiological processes in living organisms using optical, ultrasound, computed tomography (CT), magnetic resonance imaging (MRI), single photon emission computed tomography (SPECT), and positron emission tomography (PET). The nuclear imaging techniques such as SPECT and PET involve the application of radiolabeled tracers, as known as radiopharmaceuticals, to track biochemical pathways in the body. Furthermore, nuclear imaging techniques remain limited by several factors like time-consuming procedures, expensive equipment, relatively poor spatial resolution<sup>2</sup>, and requiring substantial amounts of contrast agents to generate sufficient signal in clinical imaging. On the other hand, fluorescence optical imaging offers real-time and high-resolution imaging of fluorophores embedded in diseased tissues<sup>3,4</sup>.

The development of indocyanine green (ICG) as a fluorescent agent, which is Food and Drug Administration (FDA) approved for the indications of assessing hepatic function<sup>5</sup> and retinal angiography<sup>6</sup>, promises a new clinical imaging modality

---

This dissertation follows the style of *Nature Biotechnology*.

(fluorescence optical imaging). ICG has been widely used in biomedical fields since it has attractive features of very low toxicity and high absorption in a wavelength range of 700 to 900 nm, which is a relatively transparent window for biological tissues. Near infrared (NIR) light (700-900 nm of wavelength) propagates deeply through tissues and provides a unique approach for molecularly-based diagnostic imaging. Over the past decades, NIR optical imaging approaches have been developed for cancer screening based upon the endogenous contrast<sup>7-12</sup> and exogenous<sup>13-17</sup> agents.

Deep tissue penetrations of light and ultra-low concentrations of fluorophore are the main factors required in fluorescence-enhanced tomography and molecular imaging studies. In animal and phantom studies found in the literature<sup>14, 15, 17-24</sup>, target depths range from 1 cm to 4 cm with 100 femtomolar concentrations of fluorophore in phantom studies and 1 picomole of dye per animal in *in vivo* studies at the lowest level. However, collection of accurate fluorescent signal measurements is limited by the high noise floor arising from the excitation light leakage through the band-rejection filters. In other words, eliminating the back-reflected excitation light remains a major challenge for sensitive fluorescence imaging. Hence, in this dissertation, we present development of an imaging system for efficient excitation light rejection by collimating the incident light on the optical filter planes. In other words, the ultimate goal of this work is to improve the sensitivity of near-infrared (NIR) fluorescence imaging and tomography by efficient excitation light rejection. This work seeks to improve efficient filter performance on both planar imaging and tomographic imaging. More specifically, we develop planar and tomographic imaging systems for improved rejection of excitation light by adapting

collimating lenses and Gradient index (GRIN) lenses into an existing frequency-domain optical imaging and tomography system. Using the developed planar system, we demonstrate improvement of TBR in molecular imaging. Finally, improvements of model match between simulations and measurements for one/two targets through the developed tomographic imaging system are presented.

In the following background sections, we outline advantage of fluorescence enhanced optical imaging, which can be performed using various measurement techniques and measurement geometries, over conventional imaging modalities. The main disadvantage of fluorescence imaging, which is problem of excitation light leakage, is addressed and concepts of collimating lens and GRIN lens are presented. In Section 3, we report how collimating optics for planar imaging affects the optical filter performance and can improve phantom and animal imaging by efficient rejection of excitation light. In Section 4, the influence of excitation light rejection on forward mismatch in tomographic imaging system is presented. Further studies for model mismatch for two heterogeneities are performed in Section 5. Finally, future work for the tomographic reconstruction including image resolution is briefly demonstrated. The organization of the entire dissertation is provided in Figure 1.

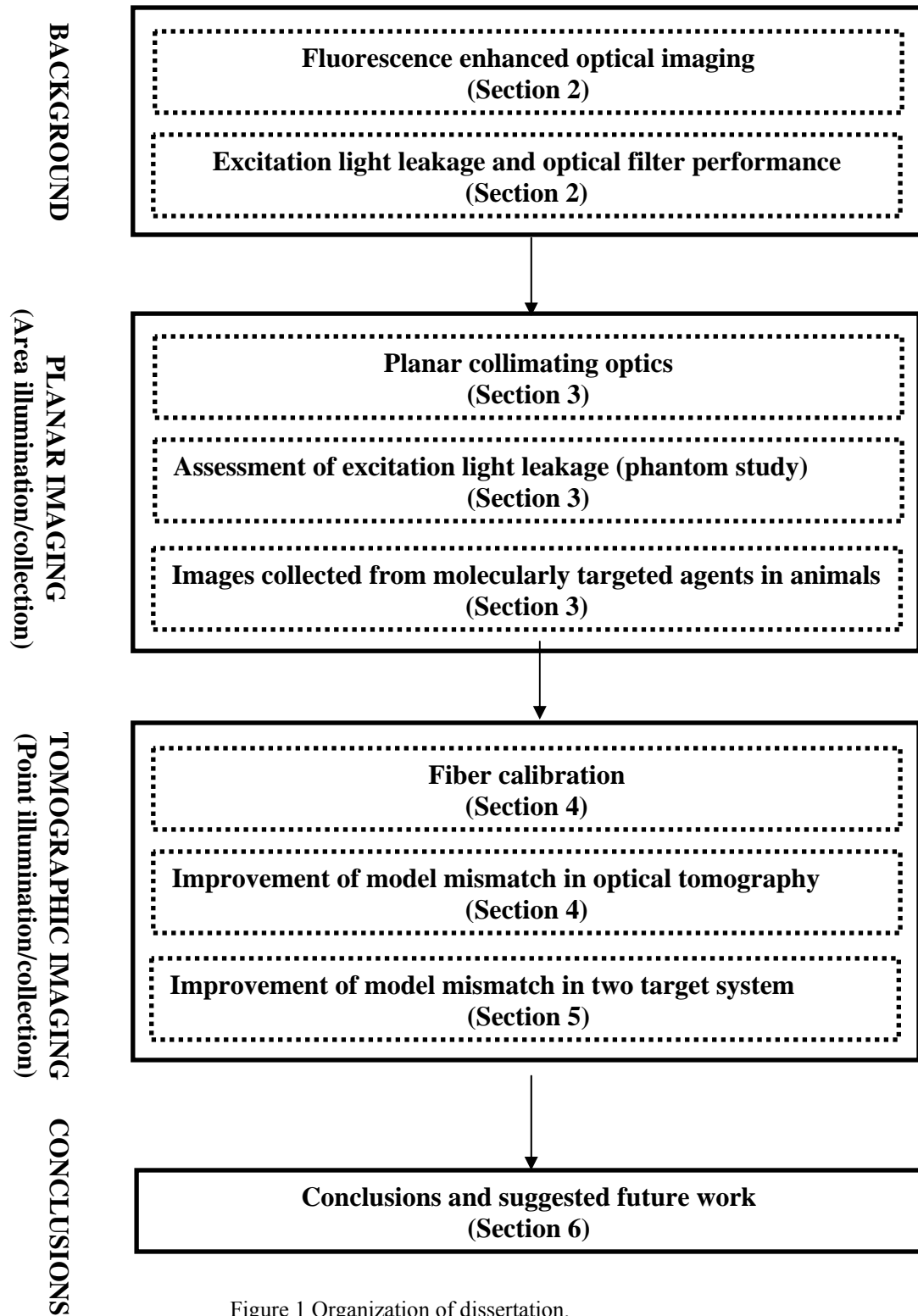


Figure 1 Organization of dissertation.

## 1.1 Significance

While molecular imaging using fluorescent agents is currently restricted to small animals and shallow penetration depths, when translated into the clinic, the issues of depth of penetration and amount of agent injected will crucially depend upon improved excitation light rejection. This work shows how improved excitation light rejection by proper optical design enhances the planar imaging. Also, this study seeks to improve model mismatch of clinically relevant tomographic imaging with heterogeneities at greater depths and with lower concentrations of fluorophores.

This work will impact the values of target to background values used to assess the molecular targeting of developed contrast agents as well as the image resolution of multiple targets through accurate reconstruction of the target location and size.

## 2. BACKGROUND

Near infrared (NIR) excitable fluorophores conjugated to proteins, peptides, and antibodies for *in vivo* targeting and reporting of tumor cells has opened opportunities for clinical diagnostic imaging in deep tissues as shown in Figure 2.

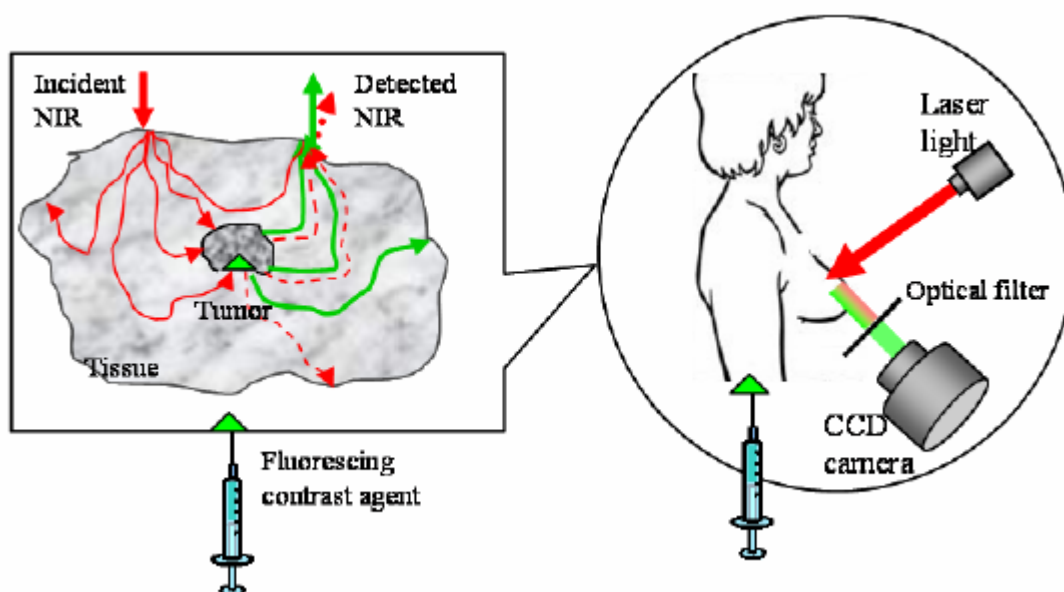


Figure 2 Schematic of the fluorescence-enhanced imaging process in a tissue medium (left) and its potential future clinical application (right)<sup>25</sup>.

A diagnostic imaging modality based upon near-infrared radiation offers several potential advantages over existing radiological techniques. First, the radiation is non-ionizing, and therefore reasonable contrast agent doses and light can be repeatedly employed without harm to the patient. Secondly, optical methods offer the potential to sensitively differentiate tissues based upon molecular markers of disease at pico-molar to nano-molar concentrations. Light in the UV-visible range does not enable deep



penetration for fluorescence imaging mainly because of autofluorescence and a high level of endogenous absorbers such as hemoglobin, deoxyhemoglobin, water, and lipids. The incident excitation light can be launched onto the tissue surface and emission light collected using various measurement geometries. Godavarty *et al.*<sup>23</sup> demonstrated experimental tomographic imaging results involving two distinct measurement geometries pertinent to diagnostic prognostic imaging of the breast. For tomographic evaluation of cancer within the breast, they employed a breast-shaped phantom and for tomographic evaluation of the depth of a sentinel lymph node and for mapping lymph flow, a semi-infinite phantom using area illumination and collection geometry was employed. In the following section, we outline the necessity for the differing measurement geometries with point illumination and collection and area illumination and collection. Also, I highlight the significant drawback of NIR fluorescence molecular imaging: the unsolved problem of excitation light leakage.

## 2.1 Fluorescence enhanced optical imaging

Fluorescence-enhanced optical imaging involves the use of fluorescent contrast agents in order to enhance the optical contrast between normal and diseased tissues. The process of emission of a photon, when a molecule relaxes from its excited state to the ground state is called as fluorescence. In this process, a molecule of significant aromaticity and conjugated double bonds absorbs light corresponding to a transitional energy level and becomes activated into a single state, from which it relaxes radiatively. Due to the loss of energy associated with the fluorescence process, the released energy

of the light, emission light is lower energy (higher wavelength) than the incident light which is excitation light.

In fluorescence-enhanced optical imaging process, when NIR light at the excitation wavelength is launched onto the tissue surface, the photon tends to propagate into deep tissues, during which is absorbed and scattered. On encountering a fluorescent molecule, the photons excite the electrons from their ground state to a higher orbital level. After residing at the higher energy orbital for a period defined as the fluorescence lifetime, the relaxation occurs and the fluorescent molecule emits a fluorescent signal along with the perturbed excitation signal propagates in the tissue. The fluorescent signal is detected at the tissue surface. The optical contrast in fluorescence-enhanced optical imaging can arise from absorption contrast or lifetime contrast. Absorption contrast is generally expressed in terms of the absorption coefficient, defined as the inverse of the mean distance a photon will travel before being absorbed. In endogenous optical contrast, absorption occurs primarily from the tissue chromophores of oxy- and deoxy-hemoglobin, fat, melanin, and water. Upon employing fluorescent contrast agents, the absorption contrast due to the fluorophore is the parameter of interest and it is based upon the concentration of the fluorophore accumulated in the target and background. Scattering is typically due to refractive index differences of extracellular and intracellular structures causing reflection, refraction, and diffraction of photons and for time-dependent fluorescence-enhanced imaging, optical contrast in terms of scattering is assumed negligible. Lifetime contrast is based on the difference in the lifetime of the fluorescing dye within the target and the background. This is achieved by using a single

fluorescing dye whose lifetime varies with respect to the surrounding environment, such that the diseased tissue exhibits a differing lifetime than that within the background. In either of the optical contrast approaches, the differences in the characteristics of the illuminated light signal and the detected signal, which is measured using time-dependent or time-independent measurement techniques, are employed to determine the location of the fluorescent molecule, and in turn the location of the diseased tissue. Details of the different measurement techniques used in performing the fluorescence-enhanced optical imaging process are described in the following section.

### 2.1.1 Measurement techniques

The two main techniques in photon migration include the 1) time-domain and 2) frequency-domain methods.

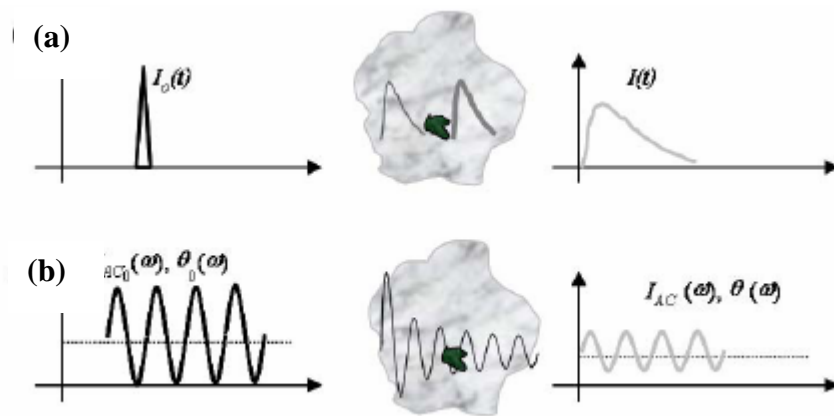


Figure 3 Schematic of optical imaging process using different measurement techniques (a) time domain photon migration, (b) frequency domain photon migration, and (c) continuous wave imaging.



Figure 3 continued

In the *time-domain* technique, picosecond or femtosecond impulse of light (full width at half maximum (FWHM)) is launched onto the scattering tissue surface and the intensity of the detected light is recorded. This detected light tends to broaden and attenuate as it travels through the scattering medium. The broadened pulse of light that is collected and detected represents the photon “times-of-flight” (see Figure 3 (a)) and can be described by the optical diffusion equation. From this equation and the “times-of-flight” data, the optical properties of the tissue can be recovered. In the frequency-domain technique, the intensity of the incident light is sinusoidally modulated and launched onto the tissue surface. Upon propagating through the scattering medium, this “photon density wave” experiences phase shift and amplitude attenuation relative to the incident light as shown in Figure 3(b). The detected phase shift and amplitude are related to the optical properties of the tissue, which in turn can be used to reconstruct an optical-property map using the optical diffusion equation. Both the time-domain and frequency-domain measurements are mathematically related to each other by the Fourier transform. However, the *frequency-domain* is preferable due to its inexpensive instrumentation compared to the time-domain and increased signal to noise ratio. Apart from these two approaches, a third technique termed *continuous-wave* (CW (See Figure 3(c)) *imaging*

involves the use of time-invariant intensity of incident light. In this approach, the exponential attenuation of light with increasing tissue depth is measured and used to detect the presence of diseased tissues. The simplicity of the technique is overcome by its inability to extract both the absorption and scattering uniquely from CW measurements<sup>26, 27</sup>. CW measurements also have limited information in fluorescence tomography since fluorescent lifetime, a parameter of contrast in time-dependent measurements is lost in CW measurements.

### 2.1.2 Light propagation model using diffusion equation

Light propagation based on the continuum approach using the transport phenomenon of light is given by the radiative transport equation of light<sup>28</sup>. Several assumptions have been made to this transport equation for computational simplicity in biological media. These assumptions are: (i) the source is isotropic which means that the source emits light with uniform angular distribution; (ii) the scattering length of the medium is much smaller than the mean free absorption length or  $\mu_s' \gg \mu_a$ ; and (iii) the distance between the point of illumination and collection is at least ten times the scattering length. With these assumptions, the photon diffusion equation can be derived and used to predict the light propagation in random media as well as in tissues<sup>28</sup>. In order to predict the fluorescent light generation and its propagation in tissues, we employ a coupled equation to predict the fluence, or the concentration of the photons times the speed of light. The coupled diffusion equation for light propagation at a given modulation frequency of light,  $f$  ( $\omega = 2\pi f$  rad) is given by<sup>29-31</sup>:

$$-\nabla \cdot [D_x(\vec{r})\nabla\Phi_x(\vec{r},\omega)] + \left[ \mu_{ax}(\vec{r}) + \frac{i\omega}{c_x} \right] \Phi_x(\vec{r},\omega) = \sum_{i=1}^n S\delta(\vec{r}-\vec{r}_s) \quad (1)$$

$$-\nabla \cdot [D_m(\vec{r})\nabla\Phi_m(\vec{r},\omega)] + \left( \mu_{am}(\vec{r}) + \frac{i\omega}{c_m} \right) \Phi_m(\vec{r},\omega) = \phi\mu_{a_{x \rightarrow m}} \frac{1}{1+i\omega\tau} \Phi_x(\vec{r},\omega) \quad (2)$$

In the above equations,  $\Phi_x$  and  $\Phi_m$  are the AC components of the excitation and emission fluence (photons/cm<sup>2</sup>), and are given by  $\Phi_{x,m} = I_{AC,x,m} \exp(-i\theta_{x,m})$ . The term  $\mu_{ax}$  is the sum of absorption coefficient that are due to the chromophores ( $\mu_{axi}$ , cm<sup>-1</sup>) (i.e. the endogenous chromophores in tissues) and the fluorophores or the exogenous fluorescing agents ( $\mu_{axf}$ , cm<sup>-1</sup>);  $\mu_{am}$  represents the sum of the absorption coefficients of the emission light due to the chromophores ( $\mu_{ami}$ , cm<sup>-1</sup>); and  $\phi$  and  $\tau$  denote the quantum efficiency and lifetime (nano-second) of the fluorophore, respectively. Also,  $c_x$  and  $c_m$  represent the velocity of light at excitation and emission wavelengths (cm/sec);  $\omega$  corresponds to the modulation frequency of propagating light ( $=2\pi f$  radians); and  $r$  and  $r_s$  are the positional vectors at the collection point and illumination point, respectively. The optical diffusion coefficients,  $D_x$  and  $D_m$  for the excitation and emission light (cm) are given by equation (3):

$$D_{x,m} = \frac{1}{3}(\mu_{ax,m} + \mu_{sx,m}(1-g)) \quad (3)$$

where  $\mu_{sx}$  and  $\mu_{sm}$  are the scattering coefficients at excitation and emission wavelengths(cm<sup>-1</sup>), respectively. Here,  $g$  represents the anisotropy coefficient, which is

defined as the average cosine of the scattering angle, and varies from 0 for an isotropic medium to 1 for a forward scattering medium (typically,  $g > 0.9$  for biological tissues). The term  $\mu_s(1-g)$  is also defined as the reduced scattering coefficient  $\mu_s'$ . Partial current boundary conditions will be employed to solve the coupled diffusion equations and are given by<sup>32</sup>

$$\Phi_{x,m}(r, \omega) + 2\gamma D_{x,m}(r) \frac{\partial \Phi_{x,m}(r, \omega)}{\partial n} = 0 \quad (4)$$

where  $\gamma$  is the index-mismatch parameter, which is a function of the effective refractive index ( $R_{eff}$ ) at the boundary surface, which is determined directly from Fresnel's reflections.<sup>32, 33</sup>

In the forward problem of fluorescence-enhanced optical tomography, the optical properties are assumed known for the entire tissue medium and the fluence is evaluated using analytical or numerical methods over the entire tissue medium. Analytical methods are employed for infinite medium or semi-infinite medium by making suitable assumptions and approximations in the medium. For a finite medium, it is difficult to solve the coupled equations analytically, and hence numerical methods such as the finite element method are employed. The finite element method involves the discretization into triangle elements in 2-D domain, or tetrahedral and hexahedral elements in the 3-D domain. In this method, if the mesh is not finely discretized, errors in the numerical solution of the coupled equations happen. However, the finite element method can be employed on curvilinear domains, such as the physiological tissue shapes, with minimum discretization errors and better computational efficiency in the inverse

problem upon appropriate coding<sup>34,35</sup>, and applicable to the coupled diffusion equations. Typically, the finite element method is formulated using the Galerkin approximation<sup>35</sup>, where the second order coupled diffusion equation is converted to first-order differential equations. The discretization level is selected based on knowledge of the domain and/or computational constraints. Image quality can be improved uniformly refining the level of discretization throughout the domain. However, this global refinement further increases the ill-posedness of the problem and results in insurmountable computational requirements by increasing the number of unknowns. On the contrary, adaptive mesh refinement<sup>36-38</sup> provides automatic fine mesh resolution around target locations with coarser resolution in other regions to improve image quality, while maintaining solution stability and computational economy.

### 2.1.3 Tomographic imaging (point source and point collection)

Basically, tomographic imaging employs the point source and collection geometry because it gives simple boundary conditions and relatively small measurement errors. The method of point illumination and point collection is achieved by illuminating excitation light at a single point and detecting the emitted fluorescent signal at a distance away from the point of illumination as shown in Figure 4(a).





Figure 4 Schematic of different measurement geometries (a) point illumination and point collection and (b) area illumination and area collection geometry.

Point illumination of excitation light from lasers or laser diodes is typically launched onto the tissue surface via optical fibers. The emitted fluorescent signal is collected via optical fibers and detected using a PMT or CCD. The incident excitation light spherically propagates and tends to attenuate exponentially with increased tissue depth, thus probing minimal tissue volume. Hence dense boundary surface measurements are required using this measurement geometry in order to locate the tumor. If the density of multiple point sources and detectors is high, its geometry is equivalent to that of area illumination and area detection below the tissue surface. However, due to the general sparseness of the point measurement geometry, point illumination may miss the fluorescent target region of interest during the imaging. Godavarty *et al.*<sup>39</sup> attempted to alleviate the sparseness of point illumination by using dual or multiple points of simultaneous excitation illumination. For optical tomography that employs endogenous contrast, measurement geometries are necessarily restricted to point illumination and point collection<sup>40</sup>. However, for fluorescence-enhance optical imaging, measurement geometries can include area illumination and collection<sup>41</sup>.

Regardless of geometry, optical tomography studies usually contain three major components as shown in Figure 5.

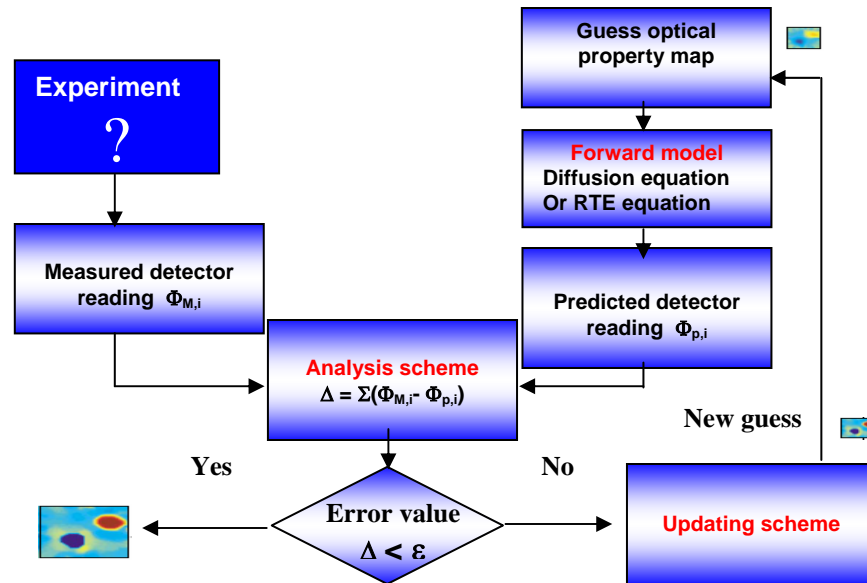


Figure 5 Basic structure of a model based tomographic reconstruction scheme<sup>42</sup>.

The first component of tomography is a so-called forward model that provides a prediction of the measurements based on a guess of the system parameters such as spatial distribution of  $\mu_a$  and  $\mu_s'$  and given source position. The second element, the analysis scheme, compares the predicted data with the measured data, which results in some sort of error function. The third part is an updating scheme that provides a new set of system parameters for the forward model, depending on the mismatch between predicted and measured data. With this set of new system parameters a new forward calculation is performed. The set of spatially varying  $\mu_a$  and  $\mu_s'$  values for which error function is minimized constitutes the final image. For fluorescence imaging, the values of absorption owing to fluorophore or life time constitute the system parameters which constitute the final image.

#### 2.1.4 Planar imaging (area illumination and collection)

Our previous work for fluorescence imaging on semi-infinite phantom uses the method of area illumination and area collection (See Figure 4(b)) which is achieved by illuminating a given area of the tissue surface and detecting the same or different area of the tissue surface<sup>41</sup>. Area illumination is achieved by using an expanded beam of excitation light from lasers or laser diodes, and the area detection is typically achieved using charge coupled device (CCD) cameras or by photography. For *in vivo* fluorescence-enhanced optical imaging of small animals, area detection is accomplished using incident powers typically ranging from  $\mu\text{W}/\text{cm}^2$  –  $\text{mW}/\text{cm}^2$ .<sup>40</sup> The area illumination and area collection technique not only increases the density of acquired boundary surface measurements, but also enhances the data acquisition rates, since a greater area of the tissue is scanned in a given time in comparison to the area scanned using point illumination and point collection geometry. Additionally, tomographic reconstruction studies for area illumination geometry has been carried out by Roy *et al.*<sup>22, 41</sup> using diffusion based algorithm. Thus, tomography from fluorescence measurement can be performed irrespective of measurement geometry.

### 2.2 Excitation light leakage and optical filter performance

#### 2.2.1 Problem of excitation light leakage

Deep tissue penetrations of light and ultra-low concentrations of fluorophore are required for fluorescence-enhanced tomography and molecular imaging studies. However, collection of accurate fluorescent light measurements is limited by the high

noise floor that arises due to the excitation light leakage through optical filters. Typically, excitation light leakage occurs if the difference between the excitation and emission wavelength maxima of the fluorescence contrast (i.e., the Stoke's shift) is very small. UV-visible excitable fluorophores show the large Stoke's shift compared to the NIR dyes. However, they have significant drawbacks for *in vivo* applications as previously mentioned. Theoretical calculation by Ntziachristos et al.<sup>43</sup> indicate that, in the NIR window, 7-14 cm of tissue penetration can be achieved using sensitive photon collection system. Yet, there has been no recognition of the limitation of the noise floor due to excitation light leakage through interference filters in these speculative published articles. The excitation light leakage problem is due to the inefficiency of the optical filters to reject the excitation light completely for accurate detection of the weak fluorescent signal. Band-pass and band-rejection interference filters have been employed extensively in near-infrared (NIR) fluorescent imaging studies in order to reject excitation light and enable efficient collection of weak fluorescent signals<sup>14-24, 39, 44-50</sup>. Target depths range from 1 cm to 4 cm with fluorophore concentrations ranging from 100 femtomoles to 2.5 micromoles in phantom studies and 1 picomole to 5.4 micromoles of dye per animal in *in vivo* studies as shown in Table 1 (see Section 3). The fluorescent imaging of deeper tissues at lower concentrations of fluorophore requires effective blockage of excitation light. In other words, eliminating the back-reflected excitation light remains a major challenge for sensitive fluorescence imaging.

### 2.2.2 Angle of incidence and filter performance

While increased depth penetration and lower fluorophore concentrations depend upon improved excitation light rejection in both time-dependent and time-invariant measurements, few investigators recognize that interference filter performance deteriorates as the angle of incident light deviates from zero degrees<sup>51, 52</sup>. Most fluorescence imaging and tomography studies do not collimate light for the normal incidence that is required for efficient excitation light rejection.

The transmission property of the interference filter and holographic filter is dependent upon its angle of incident light. Figure 6 (a) plots the transmittance of the

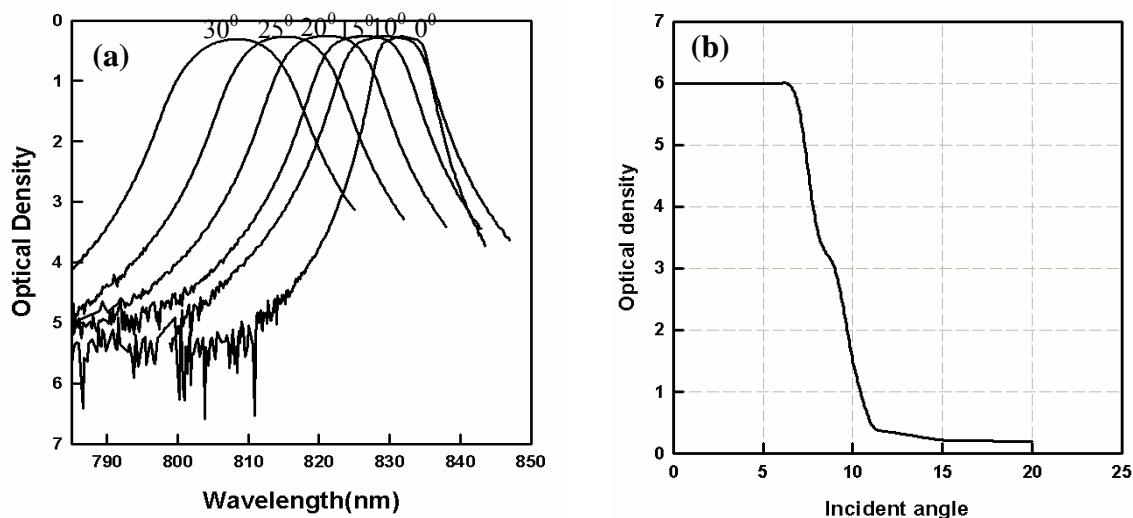


Figure 6 (a) Optical density of 830nm interference filter as a function of incident angle, (b) optical density of Kaiser Holographic filter as a function of incident angle<sup>52</sup>.

interference filter as a function of angle of incidence (AOI) provided by manufacturer (Andover Corporation). As the AOI increases, the peak of the transmittance curve shifts to shorter wavelengths, optical density increases at excitation wavelength (785 nm) and decreases at emission wavelength (830 nm). The same trend is also found in a holographic filter as shown in Figure 6 (b). In other words, excitation light with larger incident angles will not be effectively blocked and emission light from the dye may not be accurately measured. Consequently, the performance of optical filters deteriorates as the angle of incidence deviates from zero.

### 2.2.3 Collimating lens and Gradient index (GRIN) lens

In order to direct collimated, normal incident light on the interference filters, collimating lenses should be positioned based upon a ray tracing calculation. Typically, positive and negative distortion happens to simple convex and concave lenses respectively because different areas of the lens have different focal lengths and different magnification<sup>53</sup>. Consequently, they are not desirable to be used as collimating lenses in internal optical design of imager. Therefore, combination of two simple lenses which is doublet lens will be employed to give the better focused image in collimating imaging system.

GRIN lenses use a negative gradient in the refractive index of glass from the center of the lens to the outside edge to bend and focus light. GRIN lenses are characterized by a length, or pitch, and a numerical aperture (NA). The pitch of GRIN lens determines how many internal images are formed within the lens. A 0.25-pitch lens focuses a

parallel beam incident on the front surface of the lens to a point on the back surface. GRIN lenses are commercially available in lengths of up to several tens of centimeters, long enough, in principle, to access deep brain structures in large animals and humans. GRIN lenses have been used for fiber bundle-coupled confocal microscopy<sup>54</sup>, *in vivo* epi-fluorescence micro-endoscopy<sup>55</sup>, and multiphoton microscopy<sup>56, 57</sup>. GRIN lenses focus light through a precisely controlled radial variation of the lens material's index of refraction from the optical axis to the edge of the lens. Most GRIN lenses have a parabolic index profile<sup>53, 58, 59</sup> typically expressed as;

$$n(r) = n_{\max} (1 - Ar^2 / 2) \quad (5)$$

where  $n_{\max}$  is the refractive index of the GRIN lens axis and  $A$  is the GRIN lens property constant which is a function of wavelength and depends on the specific GRIN material.

In this dissertation, we seek to adapt collimating and GRIN lenses in an existing frequency-domain system to improve excitation light rejection and enhance planar and tomographic imaging.

### 3. ENHANCED FLUORESCENT OPTICAL IMAGING WITH IMPROVED EXCITATION LIGHT REJECTION: PLANAR IMAGING\*

#### 3.1 Introduction

Fluorescence-enhanced tomography and planar imaging studies for *in vivo* molecular imaging require deep tissue penetration of light for activation of ultra-low concentrations of fluorophore. However, the collection of accurate fluorescent light measurements requires the separation of weak fluorescent signals from an overwhelmingly large component of scattered excitation light. Consequently, fluorescence enhanced imaging is limited by the high noise floor that arises due to the excitation light leakage through the band-pass and band-rejection interference filters that have been employed extensively in near-infrared (NIR) fluorescent imaging studies<sup>14-24, 39, 44, 46-49, 60, 61</sup>. Yet the rejection of excitation light for fluorescence enhanced imaging in small animals easily rivals the stringent requirements for removal of excitation light in Raman spectroscopy, which employs holographic filters for removal of collimated excitation light. Table 1 provides a listing of reported efforts for *in vivo* fluorescence imaging in animals<sup>15-17, 19, 24, 44, 46-48, 60, 61</sup> and tissue phantoms<sup>14, 18, 20-23, 39, 49</sup> which shows that few investigators, inclusive of our own group, employ collimation and

---

\*Reprinted with permission from “Improved excitation light rejection enhances small-animal fluorescent optical imaging” by Kildong Hwang, Jessica Houston, John Rasmussen, Amit Joshi, Chun Li, Shi Ke, and Eva Sevick-Muraca, 2005, *Molecular Imaging*, 4, 194-204. Copyright 2005 by BC Decker.



appropriate filters with sufficient optical densities for collection of weak fluorescent signals. Despite the non-optimal excitation light rejection, studies nonetheless report fluorescent target depths ranging from 1 cm to 4 cm with fluorophore concentrations ranging from 100 femtomoles to 2.5 micromoles in phantom studies and 1 picomole to 5.4 micromoles of dye per animal in *in vivo* small animal imaging studies. The fluorescent imaging of deeper tissues at lower concentrations of fluorophore requires improved effective blockage of excitation light.

In a first attempt to address the problem of excitation light leakage for fluorescence imaging in tissues, Houston *et al*<sup>14</sup> reported the efficiency of excitation light rejection using bandpass and holographic notch filters, which retained high fluorescence signals arising from 100 femtomoles located as deep as 4 cm in tissue mimicking phantoms using time-dependent, frequency domain photon migration (FDPM) measurements. FDPM measurements refer to the propagation of intensity-modulated light through tissue-like scattering media and the measurements of the re-emitted amplitude,  $I_{AC}$ , phase-delay relative to the incident light,  $\delta$ , and the average intensity,  $I_{DC}$ , which is analogous to continuous wave or conventional intensity-based imaging. While increased depth penetration and lower fluorophore concentrations depend upon improved excitation light rejection in both time-dependent and time-invariant measurements, few investigators recognize that interference filter performance deteriorates as the angle of incident light deviates from zero degrees<sup>51,52</sup>. As detailed in Table 1, most fluorescence imaging and tomography studies do not collimate light for the normal incidence that is required for efficient excitation light rejection. Recently, Chen *et al*<sup>49</sup> employed a

convex lens to collimate the detected light delivered via a fiber optic prior to its passing through an interference in order to overcome the excitation light leakage. Unfortunately, the assessment of excitation light leakage was not addressed. Herein, we report a study to illustrate the impact of collimation and excitation light leakage upon fluorescence imaging.

In this study, we employ collimating lenses between interference filters in order to align the collected excitation and fluorescent light normal to the filter surfaces for efficient rejection of excitation light. To quantitate filter performance, we compute the ratio of “out-of-band ( $S(\lambda_x)$ )” to “in-band ( $S(\lambda_m) - S(\lambda_x)$ )” signals registered on a gain-modulated intensified charge coupled device (ICCD) used to image a tissue-mimicking phantom in the presence of and in the absence of ten nanomolar concentration of indocyanine green (ICG). To quantitate image improvement owing to improved excitation light rejection, we imaged the molecular targeting of the integrin  $\alpha_v\beta_3$  receptor with an arginine-glycine-aspartic acid (RGD) peptide-dye conjugate in xenografts of human glioma<sup>62</sup> and assessed improvement in TBR and signal to noise ratio (SNR). Using both phantom and animal imaging, we demonstrate the importance of proper optical design when employing interference filters to reject excitation light.

Table 1 Review of literature for efficient collection of fluorescence signal in phantom and animal studies

Reference	Type	Dye, dose or target concentration and depth	$\lambda_x$	$\lambda_m$	Filter	OD at $\lambda_x$	Collimated light
Weissleder <i>et al</i> <sup>15</sup> -1999	<i>in vivo</i> (mouse)	Cy5.5, 10 $\mu$ mol/mouse	675 nm	694 nm	610-650 nm bandpass filter (Omega optical) 700 nm bandpass filter (Omega optical)	5.0	No
Achilefu <i>et al</i> <sup>17</sup> -2000	<i>In vivo</i> (rat)	ICG, 5.4 $\mu$ mol, 0.5 ml Cypate, 5.0 $\mu$ mol, 0.5 ml	780 nm	830 nm	830nm interference filter (CVI Laser Corp.)	4.0	No
Gurfinkel <i>et al</i> <sup>44</sup> -2000	<i>In vivo</i> (dog)	ICG, 1.0 mg/kg HPPH-car, 0.3 mg/kg	785 nm 660 nm	830 nm 710 nm	bandpass interference filter 830 nm, 710 nm (CVI Laser Corp.)	4.0	No
Achilefu <i>et al</i> <sup>60</sup> -2002	<i>In vivo</i> (rat)	ICG, 5.4 $\mu$ mol, 0.5ml Cytate, 6.0 $\mu$ mol, 0.5ml	795 nm	830 nm	830 nm Interference filter (CVI Laser Corp.)	4.0	No
Eppstein <i>et al</i> <sup>18</sup> -2002	Phantom (4*8*8 cm <sup>3</sup> )	ICG, 0.02 $\mu$ M Target depth (3-4 cm)	785 nm	830 nm	830 nm band-pass filter (CVI Laser Corp.)	4.0	No
Mahmood <i>et al</i> <sup>46</sup> -2002	<i>In vivo</i> (mouse)	Cy5.5, 10 nmol, 100 $\mu$ l GFP, 10 nmol, 100 $\mu$ l ICG, 10 nmol, 100 $\mu$ l	615-645 nm 406-450 nm 716-756 nm	680-720 nm 495-525 nm 780-820 nm	Five cavity band-pass for each emission wave (Omega Optical)	5.0	No
Ntziachristos <i>et al</i> <sup>19</sup> -2002	Phantom (tube with capillary) <i>In vivo</i> (mouse)	1 $\mu$ M cathepsin B probe Target depth (on the surface of tube) Cy5.5, 2 nmol/mouse	675 nm	710 nm	Bandpass filter (Andover corp.)	*	No
Tung <i>et al</i> <sup>47</sup> -2002	<i>In vivo</i> (mouse)	NIR-2folate conjugate 2 nmol	630 nm	700 nm	630, 700 nm bandpass (Omega Optical)	5.0	No
Shives <i>et al</i> <sup>20</sup> -2002	Cylindrical phantom (3 cm in diameter)	SCCN, 10mg/l target depth(7-9mm)	635 nm	694 nm	700 nm bandpass	*	No

Table 1 continued

Reference	Type	Dye, dose or target Concentration and depth	$\lambda_x$	$\lambda_m$	Filter	OD at $\lambda_x$	Collimated light
Kircher <i>et al</i> <sup>18</sup> -2002	<i>In vivo</i> (mouse)	Cy3.5, 120 $\mu$ g/150 $\mu$ l	520 nm	600 nm	Excitation, emission bandpass (Omega Optical)	5.0	No
		Cy5.5, 60 $\mu$ g/150 $\mu$ l	630 nm	700 nm			
Houston <i>et al</i> <sup>14</sup> -2003	Phantom (10*10*10 cm <sup>3</sup> )	ICG, 1 $\mu$ M, 100 femto mole Target depth (1-4 cm)	785 nm	830 nm	830 nm bandpass (CVI ) 785 nm holographic notch (Kaiser) 812 nm long pass (Omega)	> 10	No
					830 nm, 710 nm bandpass (Andover Corp.)		
Ke <i>et al</i> <sup>16</sup> -2003	<i>in vivo</i> (mouse)	ICG, 1nmol/mouse	785 nm	830 nm	785nm , 660 nm holographic notch (Kaiser optical system)	> 10	No
		Cy5.5, 2.9nmol/mouse	660 nm	710 nm			
Thompson <i>et al</i> <sup>21</sup> -2003	Phantom (22 cm in diameter, 12 cm In height)	ICG, 0.1 $\mu$ M Target depth(1cm)	785 nm	830 nm	830 nm band-pass filter (CVI Laser Corp.)	4.0	No
					830 nm band-pass filter (Andover Corp.)		
Thompson <i>et al</i> <sup>22</sup> -2003	Phantom (8*8*8 cm <sup>3</sup> )	ICG, 1 $\mu$ M DTTCI, 1.42 $\mu$ M Target depth(1cm)	785 nm	830 nm	785 nm holographic notch filter (Kaiser optical system)	> 10	No
Chen <i>et al</i> <sup>49</sup> -2003	Phantom (18*18*12 cm <sup>3</sup> )	ICG, 1 $\mu$ mol, 250 $\mu$ l Target depth (2-3 cm)	780 nm	830 nm	Two 830 nm interference (Omega Optical)	>6.0	Yes
Chen <i>et al</i> <sup>24</sup> 2004	<i>in vivo</i> (mouse)	RGD-Cy5.5, 0.1-3 nmol/mouse	633 nm	685-765 nm	Cy5.5 filter set	*	No
Funovics <i>et al</i> <sup>61</sup> -2004	<i>In vivo</i> (mouse)	Cy5.5	*	*	690-800 nm six cavity bandpass 670 nm excitation short pass filter (Omega Optical)	5.0	No
		1-10 pmol/mouse					

Table 1 continued

Reference	Type	Dye, dose or target Concentration and depth	$\lambda_x$	$\lambda_m$	Filter	OD at $\lambda_x$	Collimated light
Godavarty <i>et al</i> <sup>39</sup> -2004	Breast Phantom (1087cm <sup>3</sup> )	ICG, 1 $\mu$ M Target depth (1.4-2.8cm)	785 nm	830 nm	830 nm band-pass filter (Andover Corp.)	> 10	No
					785 nm holographic notch filter (Kaiser optical system)		
Godavarty <i>et al</i> <sup>23</sup> -2004	Breast Phantom (1087cm <sup>3</sup> )	ICG, 1-2.5 $\mu$ M Target depth	785 nm	830 nm	830 nm band-pass filter (Andover Corp.)	> 10	No
	Phantom (8*8*8cm <sup>3</sup> )	(1.2-1.4cm)			785 nm holographic notch filter (Kaiser optical system)		

\* : Not given

## 3.2 Materials and methods

### 3.2.1 Phantom studies

The phantom consisted of a 1 liter black cubic box filled with 1% Liposyn, a fat emulsion whose scattering properties mimic those of tissue. The 1% solution was prepared by volumetric dilution of 20% stock solution (Abbott Lab., North Chicago, Illinois) using deionized, ultra filtered water. ICG (Sigma-Aldrich Co., St. Louis, Missouri) was initially dissolved in deionized, ultra filtered water and then added to 1 liter of 1% Liposyn to formulate a 0.01  $\mu\text{M}$  solution. Sodium polyaspartate (PASP) (Sigma-Aldrich Chemical Co., St. Louis, Missouri) was added at 5.2 molar excess of ICG to stabilize the dye from non-covalent interactions.<sup>63</sup> The surface of the phantom was illuminated with excitation light at 785 nm and emission from ICG was collected at 830 nm.

### 3.2.2 Animal studies

For the *in vivo* imaging studies, six to eight week-old female athymic nude mice (nu/nu:18-22g) were purchased from Harlan Sprague Dawley, Inc. (Indianapolis, IN). Animals were maintained in a specific pathogen-free mouse colony in the Department of Veterinary Medicine (The University of Texas M.D. Anderson Cancer Center). The animal protocol was approved by the American Association for Laboratory Animal Care and all experiments were conducted in accordance with guidelines of the Institutional Animal Care and Use Committee.

$1 \times 10^6$  cells of human glioma U87 were implanted subcutaneously into the thigh region of mice. Tumor mass was allowed to grow approximately 1-5 mm diameter in size. IRDye<sup>TM</sup>800 (LI-COR, Biotechnology, NE, USA) bound to RGD peptide<sup>62</sup> was injected into tail vein of an anesthetized mouse at a dose of 20 nmol per animal. The RGD peptide is known to target the integrin  $\alpha_v\beta_3$  receptor which is over expressed in the U87 tumor model. IRDye<sup>TM</sup> 800 has similar excitation and emission spectra as ICG and was excited at 785 nm and its fluorescence was collected at 830 nm. Twenty-four hours following the intravenous administration of peptide conjugated dye, the mice were anesthetized by 1.5-2.0 vol. % of isoflurane (Isoflo, Abbott Laboratories, North Chicago, Illinois) using mechanical ventilation and imaged using an ICCD camera.

### 3.2.3 Instrumentation

FDPM measurements of the phantom and tumor bearing mice were conducted using the homodyned ICCD camera system, which has been described in Appendix A. The CCD camera (Photometrics Ltd., series AT200, model SI512B, Tucson, AZ) is comprised of a  $512 \times 512$ -array of potential wells (pixels) that convert incident photons into electrons. The size of a pixel is  $24 \times 24 \mu\text{m}$  and active imaging area of CCD chip is  $12.3 \times 12.3 \text{ mm}$ . FDPM consists of employing an incident, intensity-modulated light excitation source that creates a “photon-density wave” that propagates continuously throughout the tissue to produce a fluorescent “photon density wave” that propagates to the surface for collection by a gain modulated ICCD imaging system.

Figure 7 illustrates the detected intensity (solid line) at one point in the image field in response to source intensity (dotted line). The measurable quantities in typical frequency domain data are the phase shift,  $\delta$ , the intensity amplitude,  $I_{AC}$ , and average value of intensity,  $I_{DC}$ , which is analogous to conventional intensity-based imaging.

The modulated excitation light was expanded over the region of interest using an optical diffuser<sup>64</sup> and a convex lens to illuminate the phantom surface uniformly. The area of illumination was 64 cm<sup>2</sup> and field of view (FOV) was 16 cm<sup>2</sup> for phantom studies. In animal studies, the FOV was 30.25 cm<sup>2</sup>.

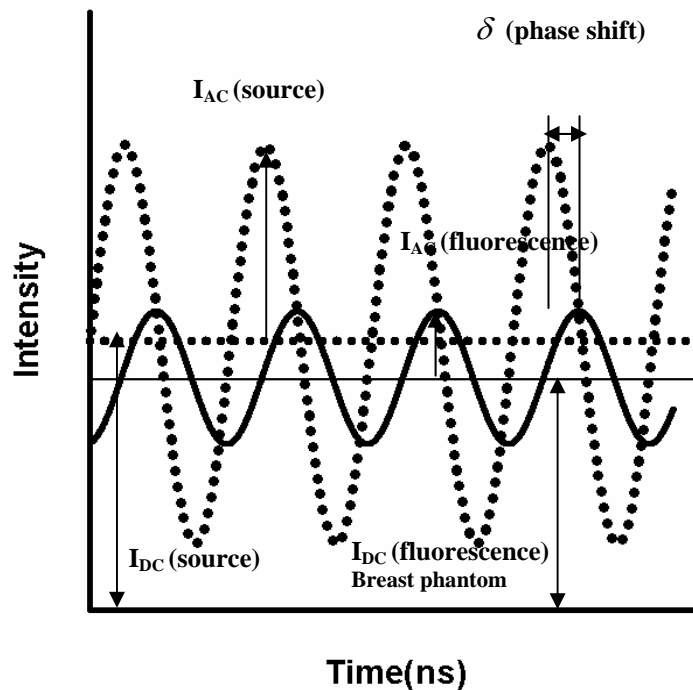


Figure 7 Schematic of FDPM measurements used in NIR optical spectroscopy and tomography.



### 3.2.4 Analysis of FDPM measurements

FDPM images of  $I_{AC}$ ,  $\delta$ , and  $I_{DC}$  were gathered using homodyne procedures and computer acquisition programs (PMIS Image processing Software, Photometrics Ltd., Tucson, Arizona for phantom studies and V++ Digital Imaging System Software, Digital Optics, Auckland, New Zealand for animal studies) as previously described.<sup>22</sup> Five binned images (128 x 128 pixels) were acquired each with 0.8 sec of integration time as a function of phase delay between the image intensifier and the laser diode operated in homodyne mode. From the average of the phase-sensitive images acquired by the CCD camera, both  $I_{AC}$  and  $\delta$  were computed using Fast Fourier Transform (FFT) analysis of zero-averaged data. For  $I_{DC}$  measurements, a dark noise obtained without laser excitation was subtracted from the images.

### 3.2.5 Selection of optical filters and collimating optics

The schematics of the optical measurements employed for investigating the improvement of excitation light rejection by collimation are illustrated in Figure 2. In order to reject off-axis light with angle of incidence greater than  $27^\circ$  on to the interference filters, one inch lens tubes (Thorlabs, Inc., NJ ) housed the combination of lenses and filters between the Nikon focusing lens and the photocathode of the image intensifier.

A three-cavity 830nm band-pass filter with 10.33 nm full width at half maximum (830FS10-25, Andover corporation, Salem, NH: optical density, OD =5.5 at 785 nm) and a holographic super notch filter (HSPF785.0-1.0, Kaiser Optical System Inc., Ann Arbor, MI : OD>6.0 at 785 nm) were employed to provide direct rejection of the 785 nm excitation light and to selectively pass emission light. As shown in Figure 3, the performance of interference filters deteriorates as the angle of incidence deviates from zero. In order to direct collimated, normal incident light on the interference filters, two collimating lenses (NIR Achromatic doublets; focal length,  $f' = 40$  mm; 1 inch of diameter; Thorlabs, Inc., NJ) were positioned based upon a ray tracing calculation (Optics Lab Optical Ray Tracing Software, Science Lab software, Carlsbad, CA) which modeled the doublet lens as thin lens. Since the diameter of the doublet lenses was greater than their thickness, this is an appropriate assumption<sup>53</sup>. The inserts to Figures 8 (a) and 8 (b) provide ray tracings from a single point on the image plane formed from the

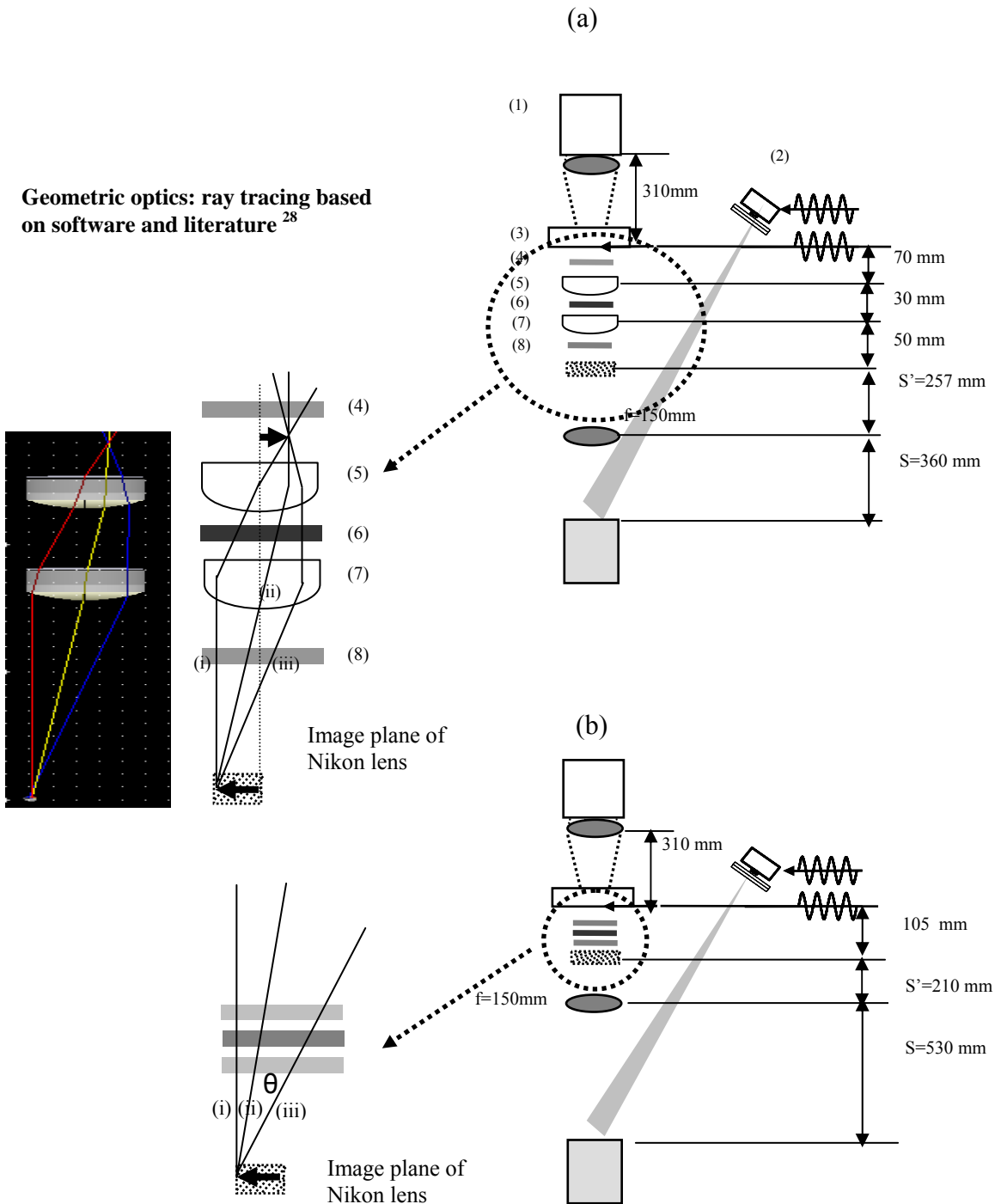


Figure 8 Experimental setup employed for the improvement of excitation light leakage (a) with collimating optics and (b) without collimating optics. Numbered components include: (1) CCD camera, (2) laser diode, (3) image intensifier, (4) Holographic filter, (5) collimating lens, (6) Bandpass filter, (7) collimating lens, and (8) Holographic filter.  $\theta$  represents angle of incidence on the filter plane.

Nikon lens in order to illustrate the impact of collimation. Typically as denoted in the insert in Figure 8 (a), there are three classifications of light directed into the first lens (7): (i) incident parallel light rays; (ii) light rays passing through the center of lens; and (iii) light rays passing through the focal point of first lens. All light incident upon the lens can be expected to be bounded by the light ray tracings (a), (b), and (c) as illustrated in the insert to Figure 8 (a). Initially consider the incident parallel ray (a) which arrives at zero incident angle on the holographic filter (8). Since it is at zero incident angle, excitation light within this ray will be blocked and not travel further for detection. Fluorescent light will pass. Excitation light in ray (b) may pass through holographic filter (8) and interference filter (6) owing to its non-zero angle of incidence, but will be blocked from detection owing to collimation by lenses (7) and (5) and its zero angle of incidence on holographic filter (4). Finally, excitation light in ray (c) may pass through holographic filter (6) but will be collimated by lens (7) to have zero angle incidence on interference filter (6). Emission light, but no excitation light in ray (c) will be detected. The distance between object and image plane of Nikon focusing lens is based upon equation (6);

$$\frac{1}{f} = \frac{1}{S} + \frac{1}{S'} \quad (6)$$

where  $f$  is effective focal length of the focusing lens;  $S$  is object distance; and  $S'$  is image distance, as noted in Figure 8. The Nikon focusing lens creates an image on the plane lying on the focus plane of the collimating lenses, as denoted by the dotted plane in Figure 8.

The insert to Figure 8 (b) shows uncollimated image delivery to the interference filters in which only excitation light in parallel ray (a) is blocked from detection and excitation light in all other rays may pass through the filters in varying amounts, dependent upon their incident angle.

### 3.2.6 Experimental design and analysis

The image of the surface of the tissue phantom in the presence and absence of uniformly distributed ICG provided a method to assess excitation light leakage. Excitation light leakage is defined as the signal,  $S(\lambda_x)$ , or average pixel intensity values associated with the image of the scattering surface taken in the absence of ICG in the solution while using bandpass and holographic filters. The fluorescence signal,  $S(\lambda_m)$ , is likewise averaged from the pixel intensity values associated with the image taken in the presence of ICG in the solution. Measurement parameters such as the intensifier gain were held constant for  $S(\lambda_x)$  and  $S(\lambda_m)$ . The  $S(\lambda_x)$  signal represents “out of band” transmission signals, whereas the difference,  $S(\lambda_m) - S(\lambda_x)$ , represents the “in-band” transmission signal. The transmission ratio of the filter and lens combination,  $R$ , is given by:

$$R(I_{DC}) \text{ or } R(I_{AC}) = \frac{S(\lambda_x)}{S(\lambda_m) - S(\lambda_x)} \quad (7)$$

where  $S$  is the signal measured either by the average intensity,  $I_{DC}$ , or the amplitude of intensity,  $I_{AC}$ . The ratio was calculated with and without collimation for the comparative performance of excitation light leakage in an annular area corresponding to 700 pixels at increasing distance,  $r$ , away from the center of the photocathode. A decrease in  $R(I_{DC})$  or

$R(I_{AC})$  signifies improved excitation light rejection which leads to increased measurement sensitivity and lower noise floors. For animal imaging, TBR and SNR were computed:

$$TBR = \frac{T}{B} = C + 1 ; SNR = \frac{T - B}{\sigma_B} \quad (8)$$

where T is target signal provided by the average  $I_{AC}$  or  $I_{DC}$  values over the tumor region of interest (ROI); B is background signal chosen to be the contralateral normal region of same area; C is contrast; and  $\sigma_B$  is standard deviation of background signals for the background ROI. Target signals T are averaged pixel intensity values for one hundred pixels of tumor tissue region and background signals B represent those of normal tissue region. Improved image quality owing to efficient excitation light rejection results in increased TBR, contrast, and SNR.

### 3.3 Results

#### 3.3.1 Phantom studies

The transmission ratios of average  $I_{DC}$  and  $I_{AC}$  images acquired with (solid bars) and without (non-shaded bars) collimating optics are shown in Figures 9 (a) and (b) as a function of distance, r, from the center of the 18 mm diameter photocathode.

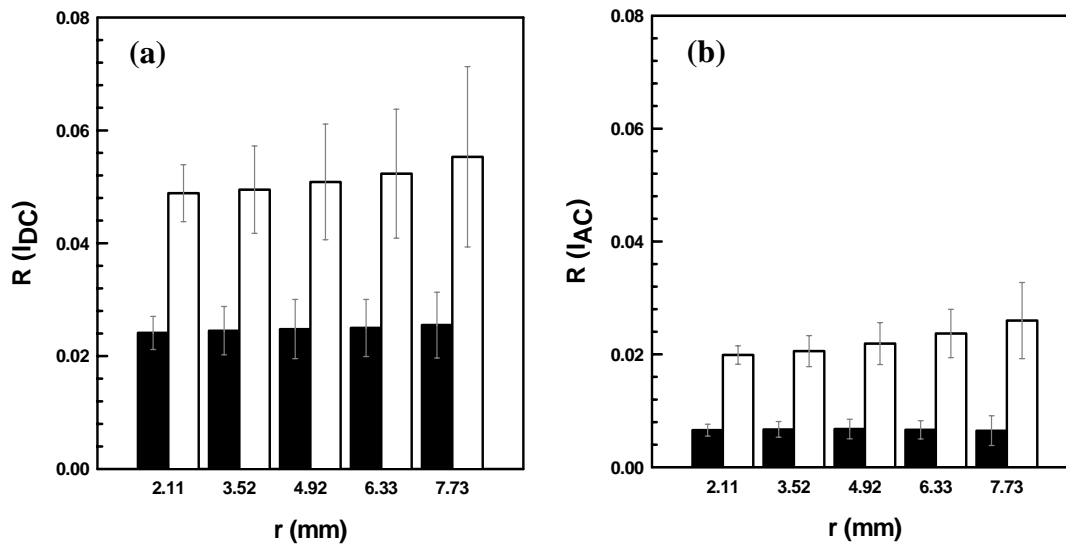


Figure 9 Transmission ratio of DC intensity ( $R(I_{DC})$ ) (a) and AC amplitude ( $R(I_{AC})$ ) (b) computed from filter combination (holographic-bandpass-holographic filters) as a function of  $r$ , the distance from the center of photocathode. Black and white bars indicate out-of-band to in-band ratio of imaging system with and without collimating optics respectively. Error bars represent standard deviations of intensity with region of interest.

In all cases, a reduction of 51 – 75 % of transmission ratio,  $R(I_{DC})$  and  $R(I_{AC})$ , occurred when collimating optics were employed. Additionally, for uncollimated images, a departure of the incident angle from normal increases the transmission ratios,  $R(I_{DC})$  and  $R(I_{AC})$ , with increasing distance from the center of the image intensifier as shown in the insert of Figure 8 (b). Without collimation, the largest off-axis incident angle of light occurred at the edge of image intensifier which corresponds to ratios at radius 7.73 mm. Significant differences at a confidence level of 0.05 occurred between the mean transmission ratio computed from collimated and uncollimated light as predicted by the hypothesis t-test<sup>65</sup>. Consistent with our previous reports<sup>14</sup>, measurements of  $I_{AC}$  have a reduced out of band transmission in comparison to  $I_{DC}$  owing to the natural frequency-filtering of ambient, out-of-band light.

### 3.3.2 Images collected from molecularly targeted agents in animals

To translate the implication of our phantom results for *in vivo* imaging, we extended experiments of excitation light leakage to animal imaging. Figure 10 (a)-(d) show the posterior view of a xenograft bearing a 5 mm diameter glioma (U87) provided by  $I_{AC}$  and  $I_{DC}$  collected with ((a) and (c)) and without ((b) and (d)) collimation optics respectively.

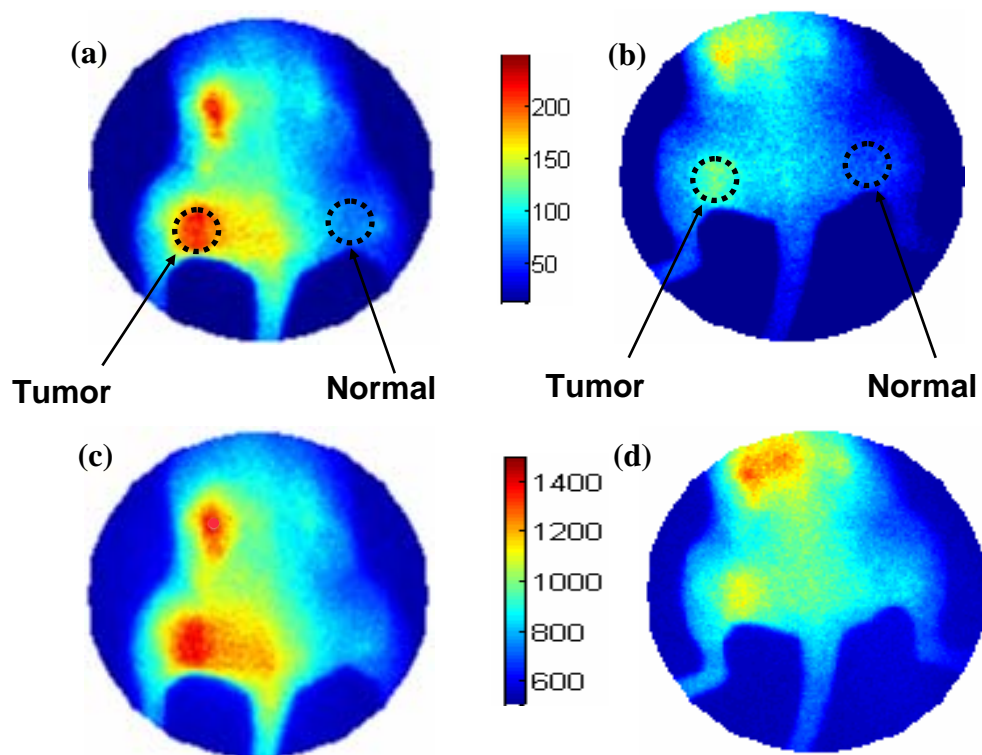


Figure 10  $I_{AC}$  image of an animal bearing 5mm diameter glioma lesion (a) with and (b) without collimating optics.  $I_{DC}$  image of an animal bearing 5mm diameter glioma lesion (c) with and (d) without collimating optics. Color bars represented raw signals without referencing.



Images in Figures 10 (a) and (b) and in Figures 10 (c) and (d) are displayed on the raw color scale without referencing each image was acquired without any alteration of the illumination source.

Tables 2 and 3 list the TBR and SNR for two animals bearing a <1 mm and 5 mm diameter glioma imaged with both  $I_{AC}$  and  $I_{DC}$  24 hours after administration of 20 nmol of the RGD-IRDye800.

Table 2 Comparison of TBR of  $I_{AC}$  and  $I_{DC}$  images with and without collimation

Dosage, tumor size	AC amplitude		DC intensity	
	Collimation	No collimation	Collimation	No collimation
20 nmol (0.2 ml), <1mm	6.55±2.265	5.90±2.763	10.76±2.731	4.45±1.945
20 nmol (0.2 ml), 5mm	15.13±2.325	11.56±2.576	17.81±2.014	12.44±1.871

Table 3 Comparison of SNR of average  $I_{AC}$  and  $I_{DC}$  images with and without collimation

Dosage, tumor size	AC amplitude		DC intensity	
	Collimation	No collimation	Collimation	No collimation
20 nmol (0.2 ml), <1mm	1.82±0.277	1.39±0.146	1.30±0.058	1.17±0.067
20 nmol (0.2 ml), 5mm	2.66±0.325	2.04±0.229	1.61±0.074	1.29±0.041

TBR obtained from the images acquired with a collimating lens improved from 11% to 31% over that of uncollimated images. The SNR of  $I_{AC}$  and  $I_{DC}$  from collimated images increased from 11 to 142% over that derived from the corresponding uncollimated images. To clarify the statistical meaning of TBR and SNR improvement, statistical formula was shown in Equation (9).

$$\frac{TBR_c \text{ or } SNR_c - TBR_{nc} \text{ or } SNR_{nc}}{TBR_{nc} \text{ or } SNR_{nc}} \times 100 \quad (9)$$

Where  $TBR_c$ ,  $SNR_c$ ,  $TBR_{nc}$ ,  $SNR_{nc}$  are TBR and SNR with and without collimating optics respectively. Differences were statistically determined using the Hypothesis Test for a difference in means with known variance method<sup>65</sup> at a significance level of 0.05.

### 3.4 Discussion

Molecular imaging using conjugated fluorescent agents requires registration of a weak fluorescent signal within the efficient rejection of an overwhelming large excitation light signal. In small animal fluorescence optical imaging, the requirements for excitation light rejection exceed or rival that of Raman spectroscopy. Improved imaging sensitivity depends upon better rejection of excitation light in order to reduce the noise floor for evaluating deeper and smaller amounts of dye. While molecular imaging using fluorescent agents is currently restricted to small animals and shallow penetration depths, when translated into the clinic, the issues of depth of penetration and amount of agent injected will crucially depend upon improved excitation light rejection. Reduction of the noise floor should be accomplished both through (i) the judicious choice of a fluorophore with a large Stoke's shift (as done herein with the choice of IRDye800 and ICG), (ii) selective illumination of the tissue with narrow spectral sources close to the excitation of the fluorophore, (iii) proper selection of combinational optical filter sets with  $OD > 6$  at  $\lambda_x$ , and (iv) by collimating the image incident upon interference filters. Optical density O.D. at the excitation wavelength describes the attenuation characteristics, i.e., a filter with  $OD = 3$  transmits 0.001 times the amount of the normally incident excitation light. Few investigators (including in the past,

ourselves) focus upon the importance of collimated excitation light rejection in their studies and few employ filters with  $OD > 6$ . While we have demonstrated the improvement of filter sets and light collimation using FDPM measurements through measurement of out-of-band to in-band transmission, TBR, and SNR, the retrofitting of conventional optical cameras with collimating lenses before the placement of interference filters can have similar impact on intensity-based images.

We have presented our TBR and SNR measurements primarily for  $I_{AC}$  which requires no background subtraction since only the modulated light is registered in the measurement. Since both the excitation and generated emission light is modulated, excitation light leakage is as problematic for FDPM as it is for conventional intensity based imaging. While one could conceivably create “difference” images prior to and following administration of molecularly targeting fluorescent agents, the problems of co-registration of images especially after long times after administration (such as imaging 24 hours following administration of agent as shown herein) and the propagation of measurement error limits the sensitivity of a “differencing” approach. Thus, excitation light rejection is paramount for molecular imaging with fluorescence. For example, consider the signal generated from a femtomolar dose of fluorescent agent whose signal is collected with an interference filter of OD 3. The collected signal levels at the emission wavelength can be six orders of magnitude less than the reflected and scattered excitation light. In this case, the signal acquired before administration (comprised mainly of non-rejected excitation light) and after the administration of the agent (whose signal is may still be predominantly comprised of non-rejected excitation light but with a

small fluorescent component) differs by a small signal level, which can be within standard error of the measured intensity values.

Intensity measurements or  $I_{DC}$  images have the added complication of ambient and dark noise counts added into the measurements which require back-subtraction while FDPM measurements eliminate the need for back-subtraction since only the modulated signal is measured.<sup>14</sup> Consistent with our past work, Figure 4 shows that transmission ratio is higher for  $I_{DC}$  than for  $I_{AC}$  images. Nonetheless, upon proper filtering and through the use of collimation optics, improvement occurs in both  $I_{DC}$  and  $I_{AC}$  images of the phantom surface.

In addition to assessing “out-of-band” signal in a controlled phantom study, we translated these results into improvements in *in vivo* small animal planar imaging. While the performance of emerging, molecularly targeting optical agents is typically assessed using CCD based imaging of the values of TBR and SNR, Tables 2, 3, and Figure 5 show that these figures of merit may be a function of excitation light rejection capabilities as well as the performance of the targeting agent. From visual comparison of Figures 10(a) with 10(b) and 10(c) with 10(d), one can see that collimation reduces the background in the tissue contralateral to the tumor region. In small animal fluorescent imaging, excitation light leakage through interference filters can therefore reduce TBRs which are used as the figure of merit for reporting the specificity of targeting fluorescent conjugates. As shown in the study by Kwon *et al*<sup>66</sup>, the dose dependent response of integrin targeting agent reported in terms of TBR did not correlate

with the dose dependent rate of conjugate uptake obtained from dynamical imaging measurements, which are less impacted by excitation light leakage than TBR. Table 2 also shows that collimation increases the TBR of  $I_{AC}$  and  $I_{DC}$  images and TBR of  $I_{AC}$  images are greater than those of  $I_{DC}$  images regardless of collimation. These *in vivo* imaging results confirm the conclusions for target phantom work which show that  $I_{AC}$  images may be more sensitive than  $I_{DC}$  images owing to reduced ambient photon noise<sup>14</sup>.

Table 3 shows that the SNR of collimated  $I_{AC}$  and  $I_{DC}$  images were greater than those of uncollimated  $I_{AC}$  and  $I_{DC}$  images for all animals due to reduced background signal. The larger background signal in the uncollimated image causes high out-of-band to in-band ratio in phantom studies and a low TBR in animal studies when compared to the images made with collimated light. The contrast (defined as TBR-1) for the collimated images was approximately 1.6 to 2.1 times that demonstrated in the uncollimated images, suggesting that serious consideration of excitation light rejection capabilities be taken into account when assessing the specificity of fluorescent, targeting agents.

## 4. INFLUENCE OF EXCITATION LIGHT REJECTION ON FORWARD MODEL MISMATCH IN OPTICAL TOMOGRAPHY: TOMOGRAPHIC IMAGING

### 4.1 Introduction

The development of near-infrared (NIR) wavelength excitable imaging agents promises a new approach for molecular imaging that could rival the “gold-standards” provided by scintigraphy, single photon emission computed tomography (SPECT), and positron emission tomography (PET). Recently, a number of cyanine dyes<sup>13, 17, 67, 68</sup>, which represent the most prominent class of NIR fluorophore, have been synthesized, and a few are commercially available. Fluorophores such as non-specific indocyanine green (ICG) and conjugatable NHS esters are stable, non-radioactive, and do not possess a physical half-life, making imaging agent design, synthesis, and implementation convenient. Furthermore, Houston *et al.*<sup>69</sup> recently employed dual-labeled RGD peptide to show the superior signal to noise (SNR) of optical over nuclear imaging in a subcutaneous xenograft model of human melanoma. The results can be explained by the ability to repeatedly re-excite the fluorophore with tissue-propagating NIR excitation light enabling as many as  $10^9$  imaging photon events per second per fluorophore as opposed to one relaxation for each nuclear isotope. However, owing to light attenuation, the comparison of NIR fluorescence with nuclear imaging techniques becomes less convincing when target tissues of interest are located deep within tissues.

Recently, we demonstrated that the excitation light leakage through bandpass rejection filters creates a “noise” floor that could restrict detection of emission light from picomolar amounts of fluorescent target deep within tissues<sup>14, 70</sup>. Using planar, small animal imaging, we recently showed that by collimating the image plane onto interference and holographic filters, target to background ratios (TBRs) improved by 1.3-fold<sup>70</sup>. The result can be explained by the deteriorating rejection performance of interference filter and holographic filters as incident light deviates from the normal direction into the filter. By collimating the image plane before passing through the rejection filters, TBR, a figure of merit of imaging agent selectivity, increased due to the improved filter performance and the enhanced efficiency collecting for weak fluorescent signals.

For detection of target tissues in clinically relevant volumes, three-dimensional optical tomography using point illumination of excitation light and fiber optic collection of generated fluorescence is employed. Since time-dependent methods provide the greatest contrast<sup>71, 72</sup> and are less impacted by changes in endogenous optical properties<sup>73, 74</sup>, herein we focus on fiber optic delivery of intensity modulated excitation light and fiber optic collection of generated fluorescence to experimentally demonstrate the use of

Gradient index (GRIN) lenses for efficient collection of weak fluorescence signals and rejection of excitation light. Table 4 provides a listing of reported application areas of GRIN lens. Typically, GRIN lenses are used for focusing and collimating light from a fiber optic,<sup>59, 75, 76</sup> microscope elements,<sup>54, 57</sup> optical imaging,<sup>77-79</sup> and sensing<sup>80, 81</sup>. Consequently, GRIN lens usage should improve registration of fluorescent signals with minimized corruption owing to excitation light leakage. In this study, we adapt GRIN lenses into an existing frequency-domain tomography system to detect fluorescence signals from a clinically relevant breast phantom in the presence and absence indocyanine green (ICG). To quantitate the improvement of tomographic information content, we compute the model mismatch errors of amplitude ratio (ACR) and relative phase difference (RPS) between fluorescent measurements with and without GRIN collimation and that predicted from a diffusion-based forward model under conditions of varying the target depth and fluorophore concentration. This work shows that model match is improved by proper adaptation of GRIN lens as collimating optics in fluorescence enhanced optical imaging.



Table 4 Literature review of application of GRIN lens to optical imaging and sensing system

Reference (year)	Lens size (Diameter / Length)	Ray tracing	Tomographic imaging	Application	Comments
Sun et al <sup>77</sup> (2004)	2 mm / 37.9 mm	Yes	No	CCD imaging	The refractive index parameters of GRIN lens by using focus test at different imaging location
Levene et al <sup>57</sup> (2004)	350 $\mu$ m / 16 mm	No	No	Multiphoton microscopy	To focus the deep brain tissue in multiphoton microscopy using GRIN lens
Vassiliev et al <sup>80</sup> (2003)	0.25 pitch	No	No	Piezo actuator sensing	To make compact high-coherent light source comprising a diode laser coupled to a resonator using GRIN lens
Buren et al <sup>76</sup> (2003)	0.25 pitch	Yes	No	Collimator	Foundations for low-loss fiber GRIN lens pair coupling with the self-imaging mechanism
George et al <sup>78</sup> (2001)	3 mm / 100 mm	No	No	CCD imaging	Scattered-light imaging <i>in vivo</i> tracks fast and slow processes of neurophysiological activation through GRIN lens
Knittel et al <sup>54</sup> (2001)	1 mm / 7.8 mm	Yes	No	Confocal microscopy	GRIN lens projects a magnified image on a distal end of a fiber-optic imaging bundle, which transfers the image to a CLSM
Rouke et al <sup>81</sup> (2001)	$\geq$ 0.25 pitch	No	No	Interferometer sensing	GRIN lens was employed to examine the polarization effects on the tilt fringes
Rector et al <sup>82</sup> (1999)	3 mm / 100 mm	No	No	CCD imaging	GRIN lens served as a relay lens from tissue to a microscope objective which projected an image onto a CCD camera
Michael et al <sup>79</sup> (1999)	350 $\mu$ m / *	No	No	GRIN scope	GRIN lens was coupled to optical imaging fiber for far-field-viewing
Suparno et al <sup>83</sup> (1994)	2 mm / 0.25 pitch	No	No	Dynamic light scattering	GRIN lens and single-micron fiber coupling was employed for light scattering measurements

\* Not given

## 4.2 Materials and methods

### 4.2.1 Breast phantom

Tomographic studies were performed using a large breast phantom of  $\sim 1087 \text{ cm}^3$  volume as shown in Figure 11 (a) and as used previously<sup>39,84</sup>. The hemispherical portion (10-cm inner diameter) of the phantom structure represents the breast tissue and the cylindrical portion (20-cm inner diameter and 10-cm height) of the phantom represents the extended chest wall regions and the tissues beneath the breast. A 0.5-cm phantom wall thickness enables the firm placement of illuminating source and collection fibers.

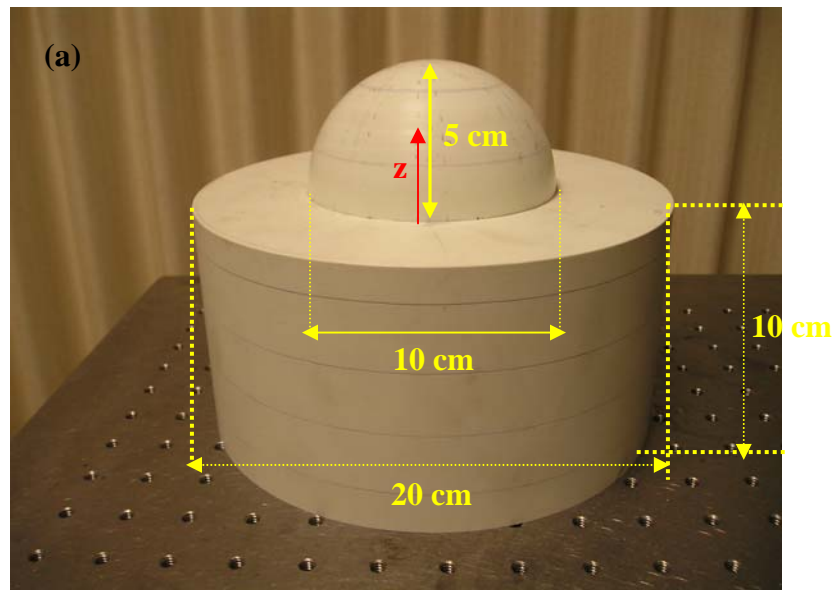


Figure 11 (a) 3D tissue-mimicking breast phantom and dimensions of the cup-shaped phantom; (b) x-y location of all 26 point illumination (filled circles) and 128 collection fiber locations (open circles) on the hemispherical portion of the breast phantom. S# and d# represent source and detector number respectively. Arrows (triangle) indicate numbering direction (counter-clockwise) of 128 collection fibers; (c) fiber bundle without grin lenses which was imaged onto the photocathode of the image intensifier.

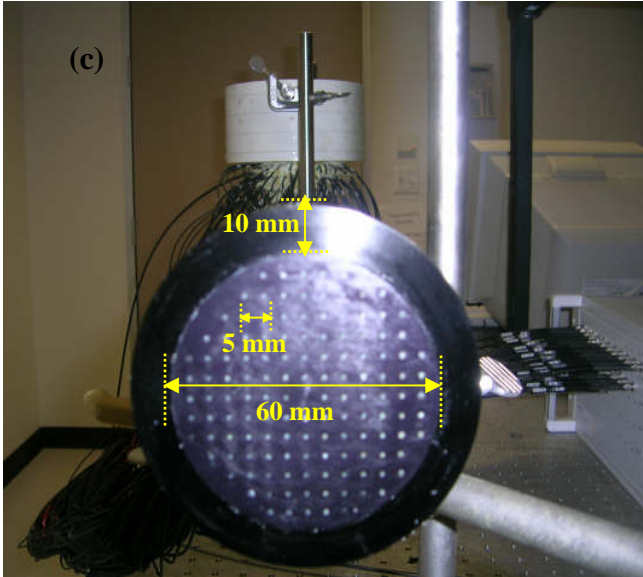
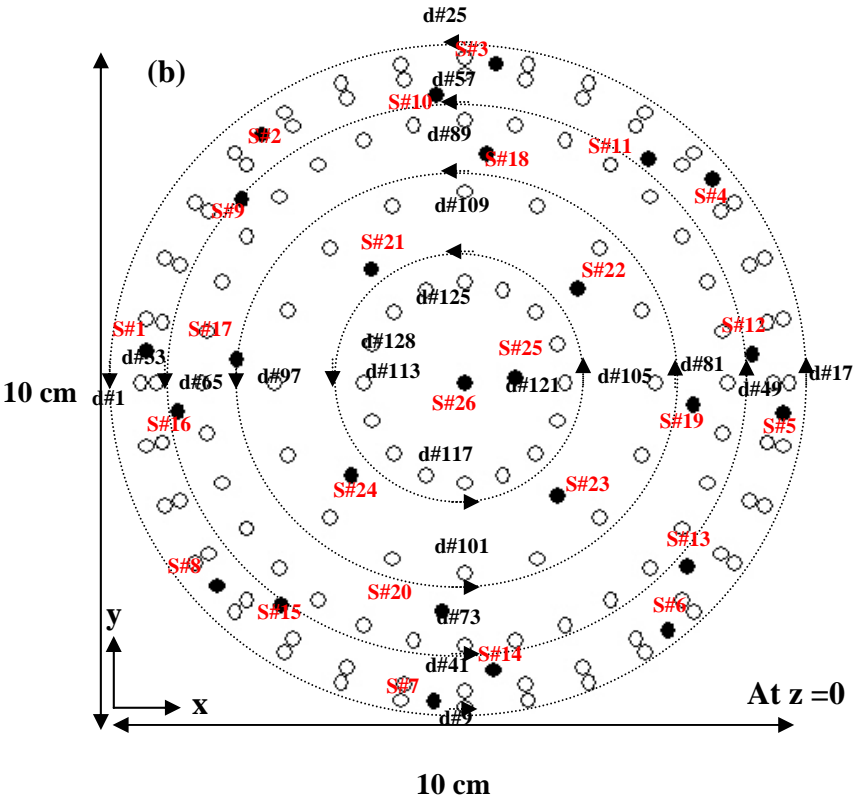


Figure 11 continued

Multimode optical fibers (model FT-1.0-EMT, Romack Inc., NJ) of 1000  $\mu\text{m}$  diameter and of 0.51 numerical aperture were used to illuminate and collect the excitation and emission light. A total of 26 sources and 128 collector fibers were glued (Mr. Sticky's underwater glue, Advanced Adhesion Inc., CA) symmetrically in concentric rings along the hemispherical portion of the phantom. Figure 11 (b) shows the locations of 128 collection fibers and 26 source fibers mounted on the hemispherical portion of the phantom. Collection and source fiber numbers are for the results presented herein and three dimensional locations of 26 source and 128 collection fibers were tabulated in Appendix B. The collection fibers terminated at a fiber bundle whose diameter is 80 mm and 128 collection fiber ends are evenly spaced by 5 mm in 60 mm of bundle face as shown in Figure 11(c) for area imaging using an ICCD camera.

An optical switch (LT 1100 Multi-Channel Switch, LIGHTech Fiberoptics, Inc., CA) was used to sequentially direct excitation light into each of twenty-six illuminating source fibers. These fibers were placed intermittently between the concentric rings of collection fibers as shown in Figure 11 (b). The phantom was filled with 1% (by volume) Liposyn (Abbott Laboratories, North Chicago, IL) solution with measured optical properties of  $\mu'_s = 10.31 \text{ cm}^{-1}$  and  $\mu_a = 0.025 \text{ cm}^{-1}$  at an excitation wavelength of 785 nm and of  $\mu'_s = 9.56 \text{ cm}^{-1}$  and  $\mu_a = 0.022 \text{ cm}^{-1}$  at an emission wavelength of 830 nm . Frequency domain photon migration (FDPM) measurements were acquired at all detectors at an emission wavelength of 830 nm for each source of excitation light. The target consisted of a  $1 \text{ cm}^3$  spherical glass bulbs with its centroid located 1.26, 2, to 3

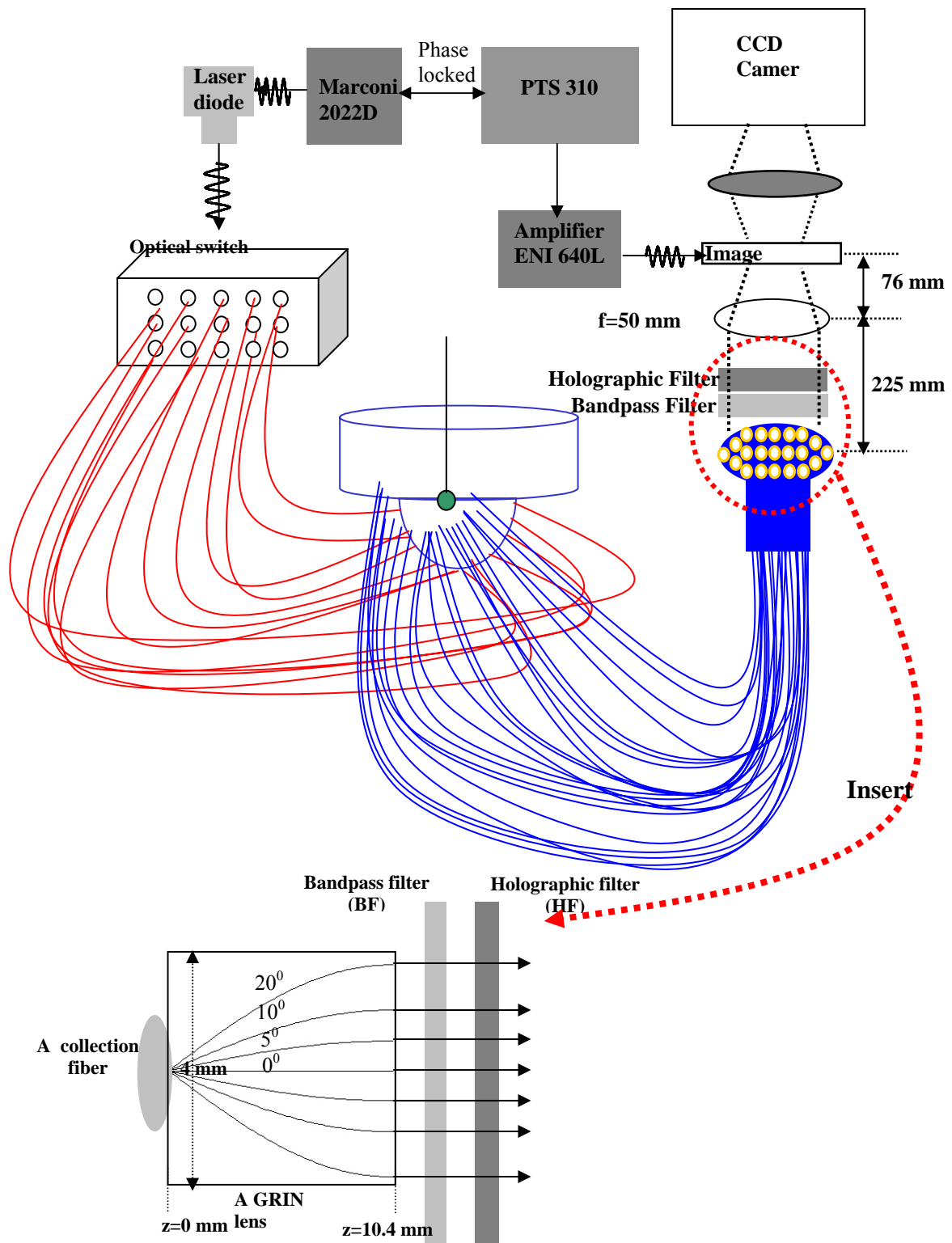
cm deep from the phantom surface at (x,y,z) coordinates of (2,1,3),(2,1,2), and (0,0,2). Varying ICG target concentrations of 0.25 to 1  $\mu$ M were investigated at a target depth of 1.26 cm. Measurement of  $I_{AC}$  and phase were acquired under TBR of 100:1.

#### 4.2.2 Instrumentation

Frequency domain photon migration (FDPM) measurements were conducted using the ICCD homodyne detection system which is described in Appendix A. As illustrated in Figure 12, a 785 nm laser diode (HPD1105-9mm-D-78505 model, maximum power of 530 mW, High Power Devices Inc., NJ), typically operated at 200 mW, was modulated at 100 MHz by a signal generator (Marconi Instrument Ltd., model 2022D, Hertfordshire, England) to generate an intensity modulated excitation source. The source was delivered sequentially via an optical switch (LT 1100 Multi-Channel Switch, LIGHTech Fiberoptics, Inc., CA) and one of the 26 source fibers to the phantom surface. The collecting fibers deliver propagated excitation and emission light to the fiber bundle faceplate where a lens (50 mm f/1.8D AF NIKKOR, Nikon Inc, New York) focuses the collected light on to the photocathode of an image intensifier (ITT Industries Night Vision, model FS9910C, Roanoke, Virginia). The photocathode of the image intensifier is modulated at 100 MHz by an amplified (amplifier model 604L, ENI Technology, Inc., Rochester, New York) sinusoidal signal from a PTS 310 (Programmed Test Sources, Inc., model 310, Littleton, Massachusetts) which is phase locked with Marconi 2022D. The intensified signal emitted from the image intensifier is focused onto a 16 bit cooled CCD camera (Photometrics Ltd., Series AT200, model SI512B, Tucson, Arizona) where

images are stored onto a computer and subsequently processed to obtain the amplitude ( $I_{AC}$ ) and phase ( $\theta$ ) of each collection fiber.  $I_{AC}$  and  $\theta$  were then referenced to the fiber with the maximum amplitude.

A three-cavity 830 nm band-pass filter with 10.33 nm full width at half maximum (830FS10-50, Andover, Salem, NH: optical density (OD) = 5.5 at 785 nm) and a holographic super notch plus filter (HSPF785.0-2.0, Kaiser Optical System, Ann Arbor, MI: OD >6.0 at 785 nm) were positioned prior to the photocathode of the image intensifier to reject the 785-nm excitation light and to selectively detect emission light. In order to collimate the light emerging out from the 128 collection fibers on the fiber bundle, custom-made gradient index (GRIN) lenses (SLW type, NSG America Inc., New Jersey) were glued to collection fibers using optical adhesives (OP series, refractive index~1.49, DYMAX Corporation, Torrington, CT). The GRIN lenses were designed from Eikonal equation<sup>85</sup> for an optimal length of 10.4 mm and a diameter of 4 mm (detailed descriptions were presented in Appendix C). The schematic of the instrumentation employed for investigating the improvement of excitation light rejection for optical tomography of the breast phantom is illustrated in Figure 12. The insert of Figure 12 shows ray tracing result of one collection fiber-GRIN lens obtained from Eikonal equation.



**< Ray tracing of a collection fiber-GRIN lens >**

Figure 12 Instrumentation set-up of the tomographic imaging system and phantom.

### 4.2.3 Fiber calibration

We found that small differences in fiber lengths made reproducible contributions to phase measurements while amplitude values were unaffected. To correct the systematic phase offsets, FDPM measurements were performed on the phantom filled with a homogeneous for 1% and 0.5% of Liposyn with 0.01 $\mu$ M ICG added respectively. The FDPM phase measurements were compared with forward model predictions and the difference between their relative phase shifts (RPS) was calculated as:

$$RPS_{errors,i} = RPS_{exp,i} - RPS_{sim,i} \quad (10)$$

where  $RPS_{exp,i}$  and  $RPS_{sim,i}$  are relative phase shift of experiments and simulations for each collection fiber,  $i$ . The  $RPS_{error,i}$  was determined with and without GRIN lenses and fiber calibration was performed by removing the  $RPS_{error,i}$  from the phase measurements obtained when the target was present. Unless otherwise stated, all phase measurements are reported as “calibrated values.”

### 4.2.4 Assessment of excitation light leakage

Measurements at the surface of target-free breast phantom containing intralipid with and without ICG provide a method to assess excitation light leakage. Excitation light leakage is defined as the signal,  $S(\lambda_x)$ , or average pixel intensity values associated with the measurements taken in the absence of ICG in the solution when bandpass and holographic filters are used. The fluorescence signal,  $S(\lambda_m)$ , is likewise averaged from the pixel intensity values associated with the measurements taken in the presence of ICG in the solution. The  $S(\lambda_x)$  signal represents “out of band” transmission signals, whereas



the difference,  $S(\lambda_m) - S(\lambda_x)$ , when taken at the same intensifier gain, represents the “in-band” transmission signal. The transmission ratio for each collection fiber is given by  $R(I_{DC})$  or  $R(I_{AC})$ ,

$$R(I_{DC}) \text{ or } R(I_{AC}) = \frac{S(\lambda_x)}{S(\lambda_m) - S(\lambda_x)} \quad (11)$$

where  $S$  is the signal measured either by the average intensity,  $I_{DC}$ , or the amplitude of intensity,  $I_{AC}$ . FDPM images of the fiber bundle enabled measurements of  $I_{AC}$  and  $I_{DC}$  at the ends of each collecting fiber using the homodyne procedure as described by Thompson *et al.*<sup>21</sup> Three binned images ( $128 \times 128$  pixels) were acquired each with 0.4 sec of integration time as the phase delay between the RF driving the image intensifier and the laser diode was changed from 0 to 360 degrees. Since the entire fiber bundle end was imaged, five pixels corresponding to each of the ends of collecting fibers were identified and processed for  $I_{AC}$  and  $I_{DC}$ . The values of  $R(I_{DC})$  and  $R(I_{AC})$  were calculated for each collection fiber with and without GRIN lenses.

#### 4.2.5 Assessment of model mismatch errors

The acquired fluorescence measurements of  $I_{AC}$  and phase for each collection fiber were referenced with respect to collection fiber which exhibited maximum amplitude value for each source illumination. The referenced values at collection fiber (i) were calculated as equation 12-13.

$$ACR_i = I_{ACi}/I_{AC,ref} \quad (12)$$

$$RPS_i = \theta_i - \theta_{ref} \quad (13)$$

Where  $ACR_i$  is amplitude ratio,  $RPS_i$  is relative phase difference, and  $I_{AC, ref}$  and  $\theta_{ref}$  are the maximum amplitude and calibrated phase values respectively for each source illumination. Values of phase were calibrated as described in section 4.2.3.

Simulations of  $I_{ACi}$  and  $\theta_i$  were obtained from the forward model of the coupled diffusion equations using an adaptive finite element method<sup>36-38</sup> to provide solution on a mesh with 35000 hexahedral elements. The difference between the referenced measurement and simulated data is called the “model mismatch error,” and which was determined in terms of the error in relative phase shift ( $RPS_{error, sum}$ ) and  $I_{AC}$  ratio ( $ACR_{error, sum}$ );

$$ACR_{error, sum} = \sum_{i=1}^{128} |ACR_i_{exp} - ACR_i_{sim}| \quad (14)$$

$$RPS_{error, sum} = \sum_{i=1}^{128} |RPS_i_{exp} - RPS_i_{sim}| \quad (15)$$

where  $ACR_{exp,i}$ ,  $ACR_{sim,i}$ ,  $RPS_{exp,i}$ , and  $RPS_{sim,i}$  are amplitude ratio, relative phase shift of experiments and simulations respectively for each collection fiber,  $i$ .

## 4.3 Results and discussion

### 4.3.1 Influence of fiber length

The correlation plot as shown in Figure 13 (a) reports  $RPS_{error,i}$  measured in 1% (y-axis) and 0.5% (x-axis) liposyn solution arising from small differences in fiber length

measured for each collecting fiber with a GRIN lens. The data were collected for illumination of excitation light at source fiber number 9. The slopes of linear regression for the correlation plot with was 1.008 ( $R = 0.990, \hat{\sigma}^2 = 0.154$ ) and Analysis of Variance (ANOVA)<sup>65</sup> method was employed to determine the linear regression parameters. From the correlation plot, we found that systematic offset is reproducible and predictable. For other source positions, similar trends of systematic offset were found and their statistics were summarized in Appendix D.

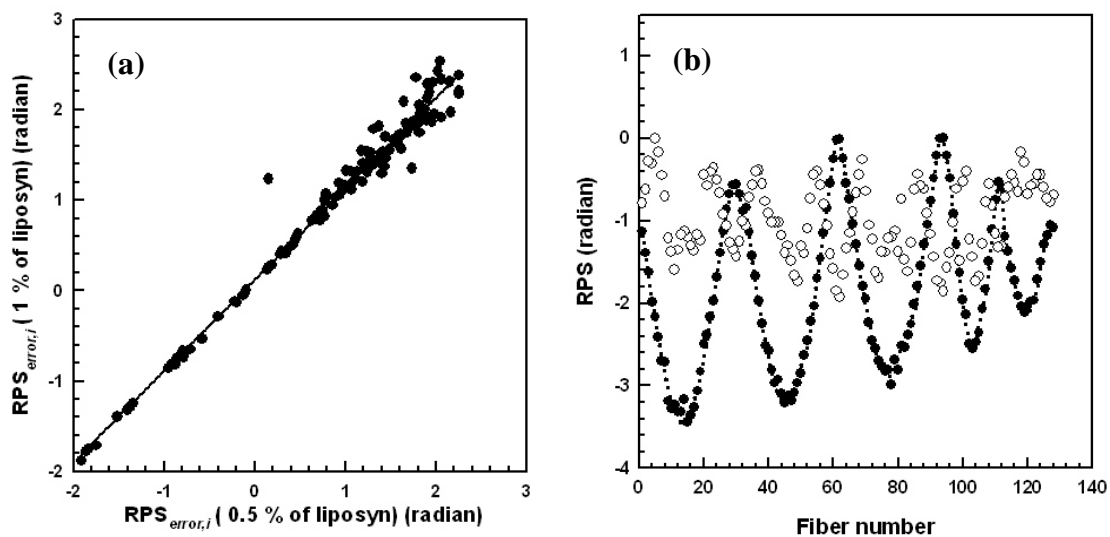


Figure 13 (a) Correlation of  $RPS_{error,i}$  from 1% liposyn versus that of 0.5% for the confirmation of systematic offset on breast phantom system. Comparison of RPS before (unfilled circles) and after (filled circles) fiber calibration as a function of collection fiber location based on a source position (source number 9). The dotted line represent RPS of forward model. Results are presented for data collected with GRIN lenses.

Figure 13 (b) reports typical measurements RPS at each collection fiber before (open symbols) and after (filled symbols) the removal of the systematic offset as found from

equation 10. The data were collected with the GRIN lenses attached and are presented for excitation illumination at source number 9 for a target of  $1\mu\text{M}$  ICG concentration at 1.26 cm depth. In all future data presented, the systematic phase offsets were subtracted from the measurements to investigate the improvement of filter performance using GRIN lens. Since fiber length does not significantly impact amplitude, no correction was made on  $I_{AC}$  and  $I_{DC}$  values.

#### 4.3.2 Transmission ratio

Figure 14 shows typical transmission ratio,  $R(I_{AC})$  ((a) and (b)) and  $R(I_{DC})$  ((c) and (d)) with and without attached GRIN lenses as a function of fiber location on the breast phantom when source fiber number 9 provided the modulated excitation illumination.

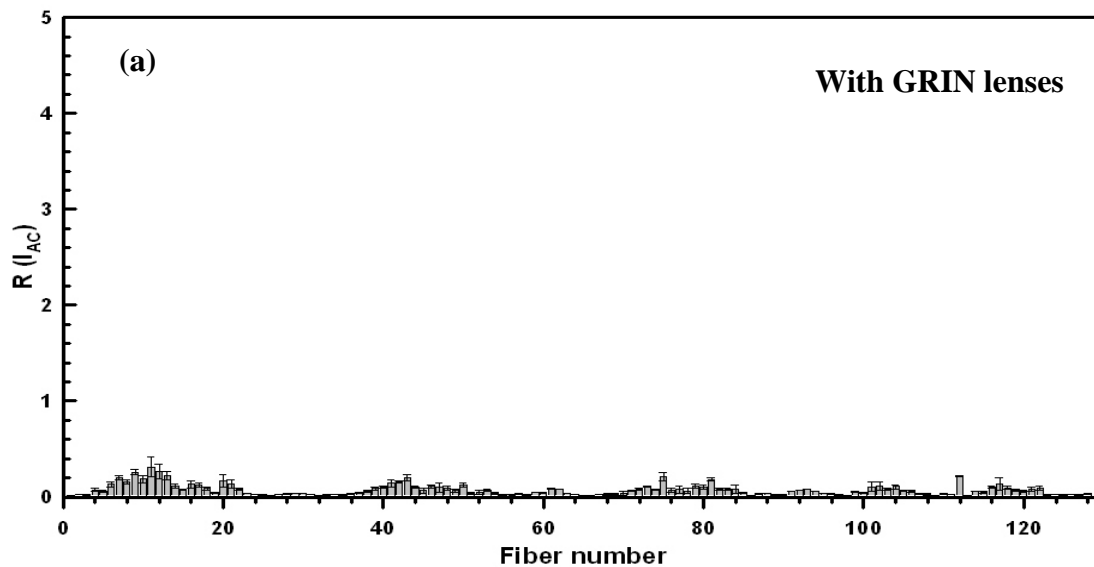


Figure 14 Comparison of transmission ratio with ((a),(c)) and without ((b),(d)) GRIN lens for  $I_{AC}$  ((a),(b)) and  $I_{DC}$  ((c),(d)) measurements based on a source position (source number 9). Filled and unfilled bars represent the transmission ratio with and without GRIN lens respectively. Error bars represent the standard deviation of transmission ratio with region of the collection fiber.

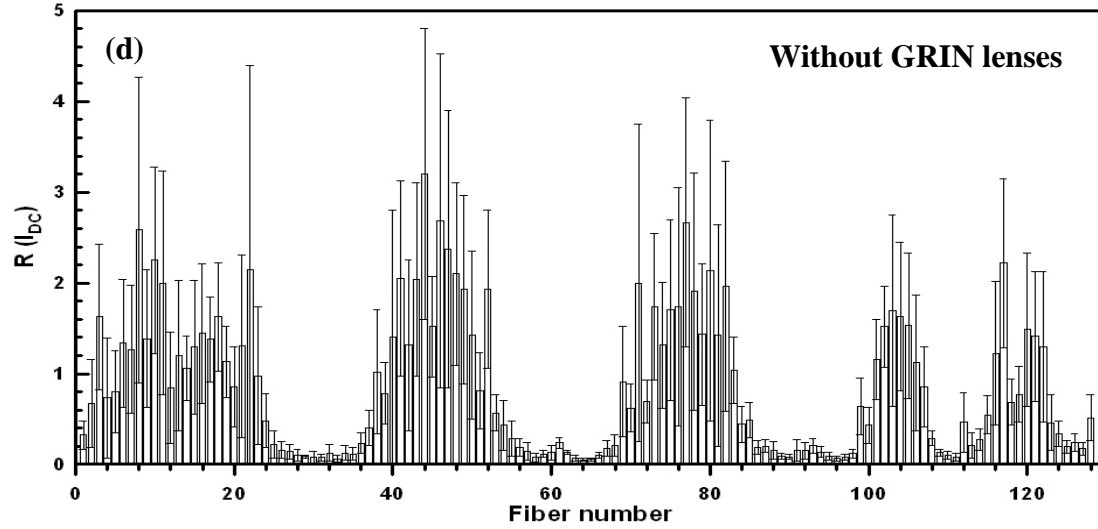
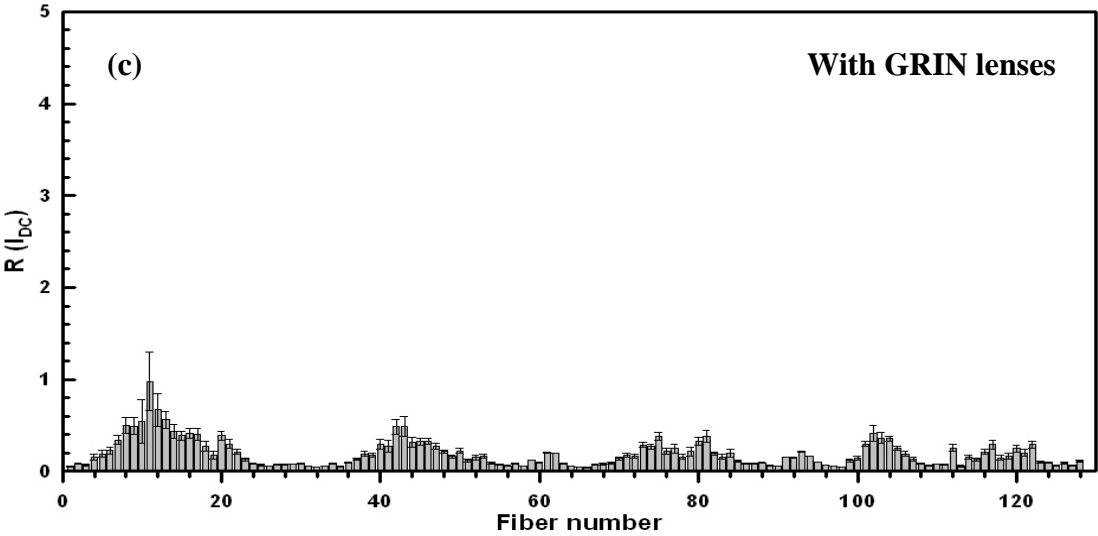
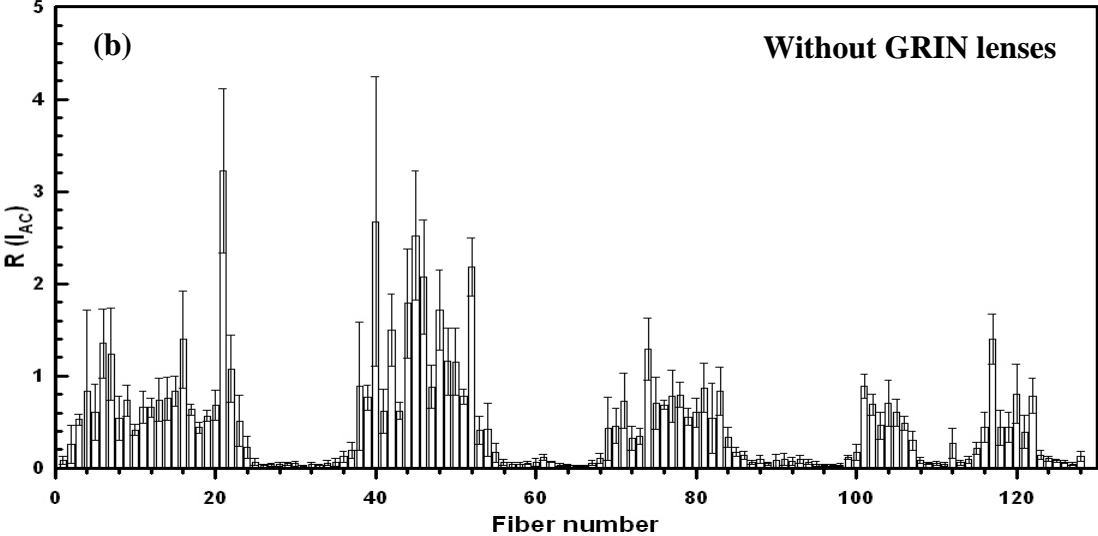


Figure 14 continued

At all collecting fiber locations, the transmission ratios for  $I_{AC}$  and  $I_{DC}$  with GRIN lens were significantly lower than those without GRIN lens due to the reduction of excitation light leakage. Significant differences at a confidence level of 0.05 occurred between the mean transmission ratio computed from measurements made with and without GRIN lens ( $p < 0.001$ ). Similar trends were found in the remaining 25 source locations and summarized in Appendix E (We do not report the signals in which the modulation depth ( $I_{AC}/I_{DC}$ ) was less than 0.025 for brevity).

#### 4.3.3 Model mismatch errors

##### 4.3.3.1 Target depth study

Figure 15 shows a typical data sets for the ACR ((a), (c), and (e)) and calibrated RPS ((b), (d), and (f)) corresponding to each collection fiber with and without GRIN lenses for source number 9 and for target depths of 1.26, 2, and 3 cm and ICG concentration on 1  $\mu\text{M}$ . The filled symbols denote data taken with GRIN lenses while open symbols denote that taken without GRIN lenses. The dotted curves represent lines connecting simulated ACR and RPS at each fiber position.

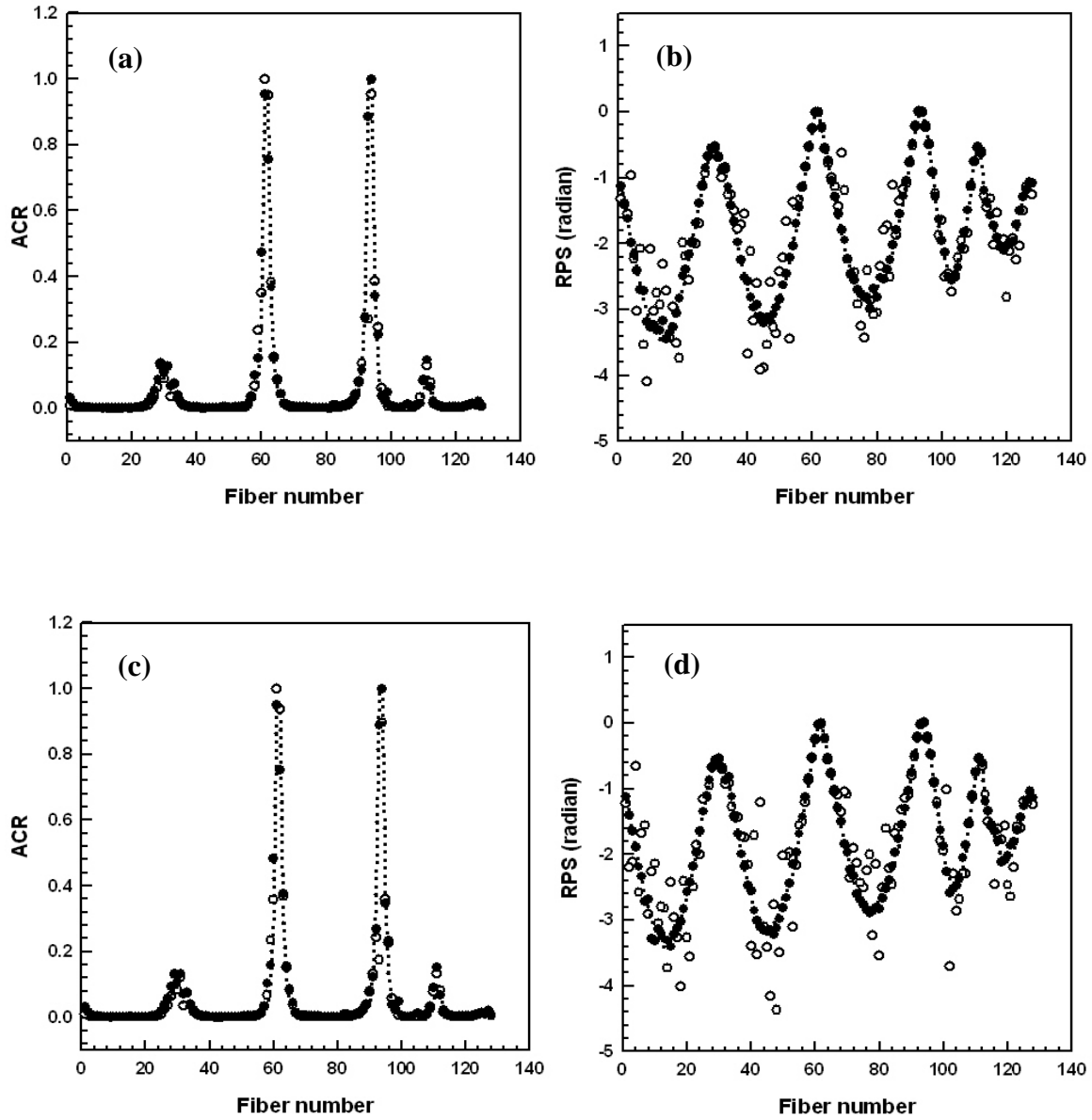


Figure 15 Comparison of amplitude ratio (ACR) ((a),(c),(e)) and relative phase difference (RPS) ((b),(d),(f)) between measurements (symbols) and forward model (dotted line) for a source location (source number 9) as a function of fiber position. The filled circles denote measurements with GRIN lenses while the unfilled symbols denote those without. Target centroid depth varied from 1.26 cm ((a), (b)), 2 cm ((c), (d)), and 3 cm ((e), (f)) at  $1 \mu\text{M}$  of target concentration.

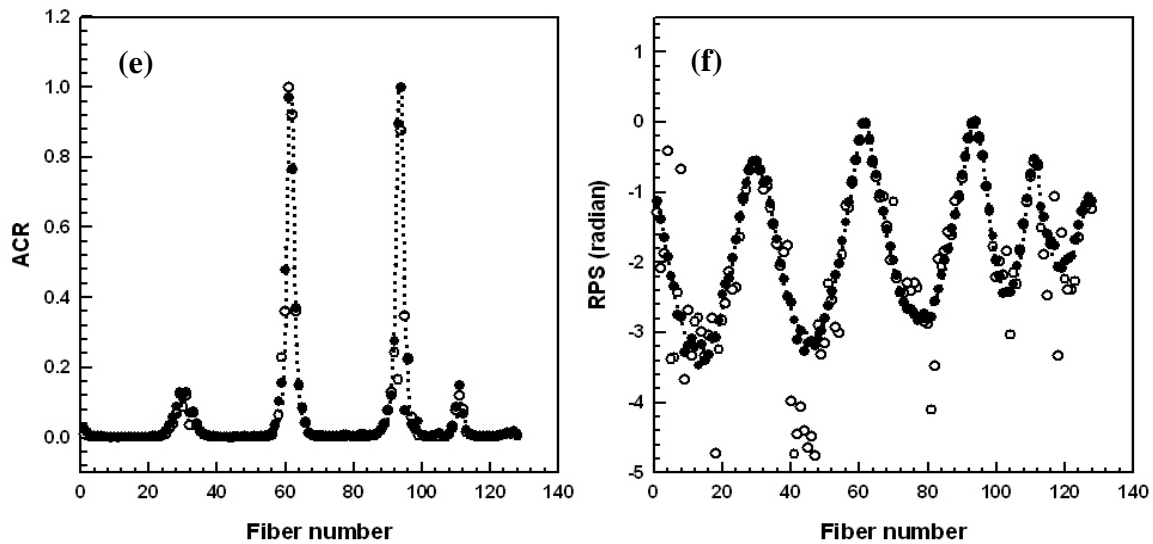


Figure 15 continued

For ACR, a good model match was observed between referenced measurements and simulations for all target depths. However as shown in Figure 15 (b), (d), and (f), large model mismatch errors were found in RPS when GRIN lenses were not used. Because systematic offsets were already removed using fiber calibration technique as described in section 4.3.1, these errors can be assumed to be a result of excitation light leakage. Figure 16 reports the mean error of ACR ((a)) and corrected RPS ((b)) for 128 collection fibers with (filled circles) and without (open circles) GRIN lenses as a function of target depth. The error bars represent the standard deviations of the summation errors of three sets of measurements resulting from illumination with source 9.



Significant differences ( $p < 0.005$ ) at a confidence level of 0.05 occurred between the mean  $ACR_{error, sum}$  and mean  $RPS_{error, sum}$  computed from equations 14 and 15 with and without GRIN lens as predicted by the hypothesis t-test.<sup>65</sup> For the remaining 25 fiber sources, similar trends were found and summarized in Table 5-6.

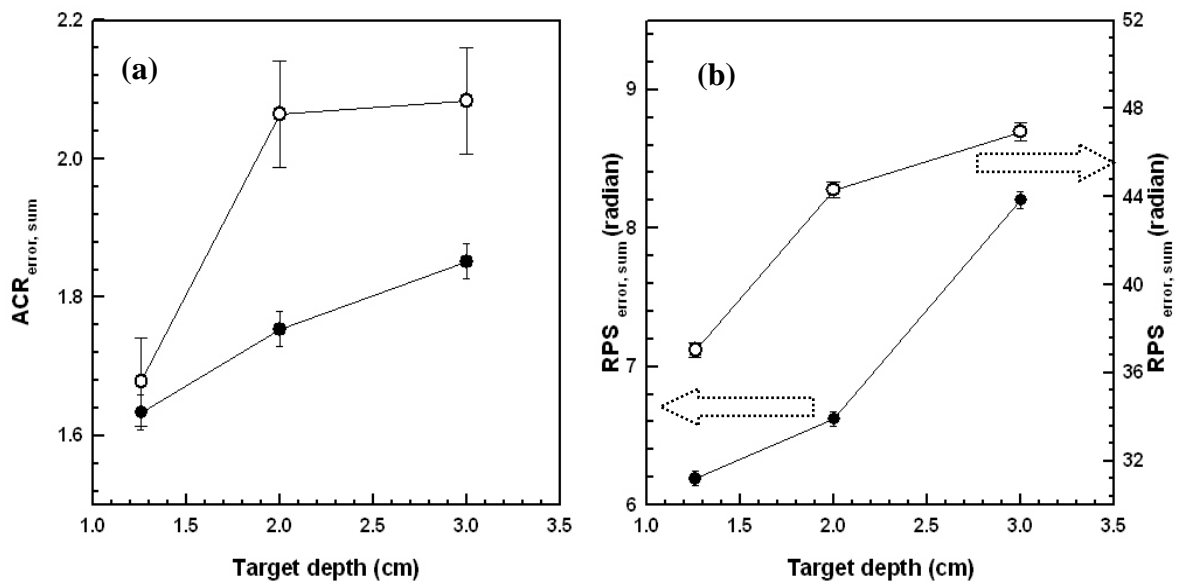


Figure 16 Comparison of mean of ACR ((a)) and RPS ((b)) errors between with and without GRIN lens as a function of target depth. Filled and unfilled circles correspond to the mean mismatch errors with and without GRIN lens respectively. Error bars represent the standard deviation of mean mismatch errors.

Table 5 Mean summation of ACR and RPS errors of 128 detectors with GRIN lens as a function of target depth for 26 sources with GRIN lens

S# Dep	ACR <sub>error, sum</sub>			RPS <sub>error, sum</sub> (radian)		
	1.26cm	2.0cm	3.0cm	1.3cm	2.0cm	3.0cm
1	1.95±.038	1.98±.037	2.10±.038	6.13±.052	6.31±.051	7.55±.063
2	1.82±.051	1.84±.051	1.86±.051	7.77±.061	8.52±.062	10.53±.064
3	2.12±.051	2.11±.051	2.15±.051	8.42±.074	10.64±.090	9.01±.075
4	1.60±.026	1.97±.026	2.09±.038	12.53±.114	16.79±.115	21.90±.422
5	1.51±.026	1.92±.038	1.92±.038	8.46±.091	10.58±.164	11.30±.204
6	2.15±.077	2.18±.064	2.28±.064	7.96±.076	9.00±.090	9.64±.178
7	2.05±.038	2.07±.038	2.09±.038	7.36±.075	7.88±.078	7.82±.063
8	1.66±.038	1.93±.051	1.96±.051	6.60±.050	6.84±.154	7.55±.062
9	1.64±.026	1.75±.038	1.86±.026	6.20±.052	6.62±.128	8.20±.064
10	1.79±.026	2.16±.051	2.18±.051	7.74±.077	8.29±.076	9.09±.067
11	1.68±.051	1.91±.077	1.82±.038	14.36±.075	18.25±.152	20.26±.307
12	1.91±.064	1.93±.051	1.95±.051	18.38±.051	23.17±.138	20.45±.281
13	2.50±.038	2.57±.038	2.59±.077	7.32±.050	8.46±.063	17.06±.282
14	3.65±.038	3.75±.077	3.79±.051	4.91±.051	5.41±.063	7.41±.064
15	1.97±.051	2.47±.051	2.49±.037	4.67±.053	4.93±.037	6.62±.051
16	2.15±.038	2.20±.064	2.21±.052	5.52±.056	5.81±.063	7.05±.064
17	2.44±.064	2.66±.038	2.60±.062	5.10±.054	5.57±.064	7.17±.052
18	2.37±.064	2.38±.038	2.41±.033	13.93±.112	14.94±.231	17.43±.370
19	3.74±.038	3.76±.077	3.94±.050	22.90±.115	21.22±.256	25.22±.446
20	2.31±.026	2.38±.051	2.41±.034	14.55±.153	15.26±.204	26.70±.499
21	2.53±.038	3.43±.064	3.30±.062	9.38±.141	8.18±.128	12.75±.231
22	1.84±.026	3.08±.038	3.56±.036	16.74±.154	17.50±.218	20.63±.294
23	3.76±.051	4.10±.077	4.28±.052	10.39±.091	10.88±.192	10.74±.179
24	5.15±.102	5.20±.102	5.43±.101	6.89±.078	9.75±.269	17.38±.282
25	9.29±.166	10.41±.205	10.94±.204	8.05±.269	9.43±.256	9.87±.192
26	8.74±.128	9.01±.128	9.81±.126	9.91±.103	10.42±.231	12.52±.218

Table 6 Mean summation of ACR and RPS errors of 128 detectors without GRIN lens as a function of target depth for 26 sources without GRIN lenses

S#	Dep	ACR <sub>error_sum</sub>			RPS <sub>error_sum</sub> (radian)		
		1.26cm	2.0cm	3.0cm	1.3cm	2.0cm	3.0cm
1		2.69±.064	3.08±.090	3.08±.090	50.62±.410	56.65±.474	62.37±.499
2		2.25±.051	2.39±.064	2.37±.064	54.40±.499	58.42±.499	57.42±.474
3		2.24±.064	2.44±.077	2.46±.075	45.16±.435	48.79±.435	57.48±.486
4		2.47±.062	2.59±.062	2.65±.064	54.87±.525	61.58±.525	76.08±.614
5		2.06±.057	2.14±.063	2.09±.065	46.32±.461	50.79±.461	53.12±.512
6		1.91±.064	2.01±.063	2.04±.064	59.23±.422	48.29v.422	67.29±.523
7		2.38±.063	2.41±.064	2.41±.063	55.88±.576	61.07±.576	61.56±.538
8		2.01±.061	2.14±.065	2.15±.064	42.14±.410	46.55±.410	46.47±.435
9		1.68±.037	2.06±.064	2.09±.077	37.06±.371	44.31±.371	46.95±.385
10		2.20±.039	2.20±.077	2.32±.052	39.67±.422	45.84±.422	47.08±.475
11		1.69±.031	1.73±.051	1.69±.052	45.64±.421	48.47±.423	49.70±.371
12		1.85±.062	1.91±.050	1.86±.051	36.65±.359	40.46±.359	41.87±.432
13		2.00±.038	2.11±.052	2.06±.038	39.58±.397	40.31±.448	40.46±.320
14		3.87±.091	3.99±.038	4.04±.091	43.88±.448	44.13±.397	50.78±.651
15		2.50±.062	2.82±.090	2.89±.078	34.68±.397	43.62±.445	42.06±.384
16		1.88±.038	2.00±.036	2.03±.034	44.62±.435	44.66±.435	46.22±.586
17		1.91±.025	2.02±.035	2.05±.036	34.46±.422	43.06±.422	39.14±.396
18		1.97±.026	1.93±.036	1.98±.091	49.14±.576	60.29±.576	69.89±.656
19		3.67±.077	4.22±.078	4.98±.051	46.25±.461	49.95±.461	50.48±.385
20		2.29±.054	2.33±.052	2.39±.051	47.71±.525	66.70±.525	73.65±.586
21		3.71±.052	3.83±.051	4.11±.062	29.24±.474	47.77±.474	45.25±.460
22		3.84±.068	5.44±.077	5.56±.102	40.79±.448	45.96±.448	44.12±.461
23		4.15±.065	4.16±.064	4.33±.067	42.79±.384	53.43±.384	53.63±.421
24		4.68±.102	4.77±.102	4.71±.101	27.55±.397	37.39±.397	41.73±.435
25		11.07±.192	12.21±.230	12.68±.230	30.18±.499	50.70±.499	45.00±.448
26		7.26±.102	11.34±.166	11.72±.166	43.47±.421	44.70±.422	54.08±.358

As might be anticipated, the model mismatch was always higher when GRIN lenses were not used as compared to when they were used. Model mismatch errors increased for both ACR and RPS as a function of target depth, probably because weak fluorescent signals at deep target locations were increasingly dominated by the noise floor of excitation light leakage, however minimized by the use of the GRIN lenses.

Due to the fluorophore lifetime, the phase of collected emission light was found to be substantially larger than that collected at the excitable wavelength. Consequently, excitation light leakage results in an artificial lowering of phase measurements at the emission wavelength. Depending upon the excitation fluence at the collecting fiber, the error in RPS can vary. It is noteworthy that across all the sources employed, we noted that the degree of model mismatch errors predicted by  $|RPS_{exp,i} - RPS_{sim,i}|$  was correlated to the transmission ratio computed from equation 11. In statistics, The slope of linear regression for the correlation plot between  $RPS_{error}$  from Figure 15(f) and  $R(I_{AC})$  was 0.68 (correlation coefficient = 0.62, p-value<0.0001) and Analysis of Variance (ANOVA)<sup>65</sup> method was employed to determine the linear regression parameters, supporting the conclusion that the accuracy of measurements depended upon leakage of excitation light. In general, the attachment of GRIN lens for collimation of collected light significantly improved the model match.

#### 4.3.3.2 Target concentration study

Figure 17 illustrates ACR ((a),(c),(e)) and calibrated RPS ((b), (d), (f)) as a function of collecting fiber location with (filled symbols) and without (open symbols) GRIN lenses for a typical source location (source number 9) as the target concentration was changed from 1, 0.5, and 0.25  $\mu\text{M}$  in the 1.26 cm beneath the surface.

A good model match in ACR was observed between referenced measurements and simulations for all target concentrations. Conversely, large mismatches were observed in RPS without GRIN lens were not employed.

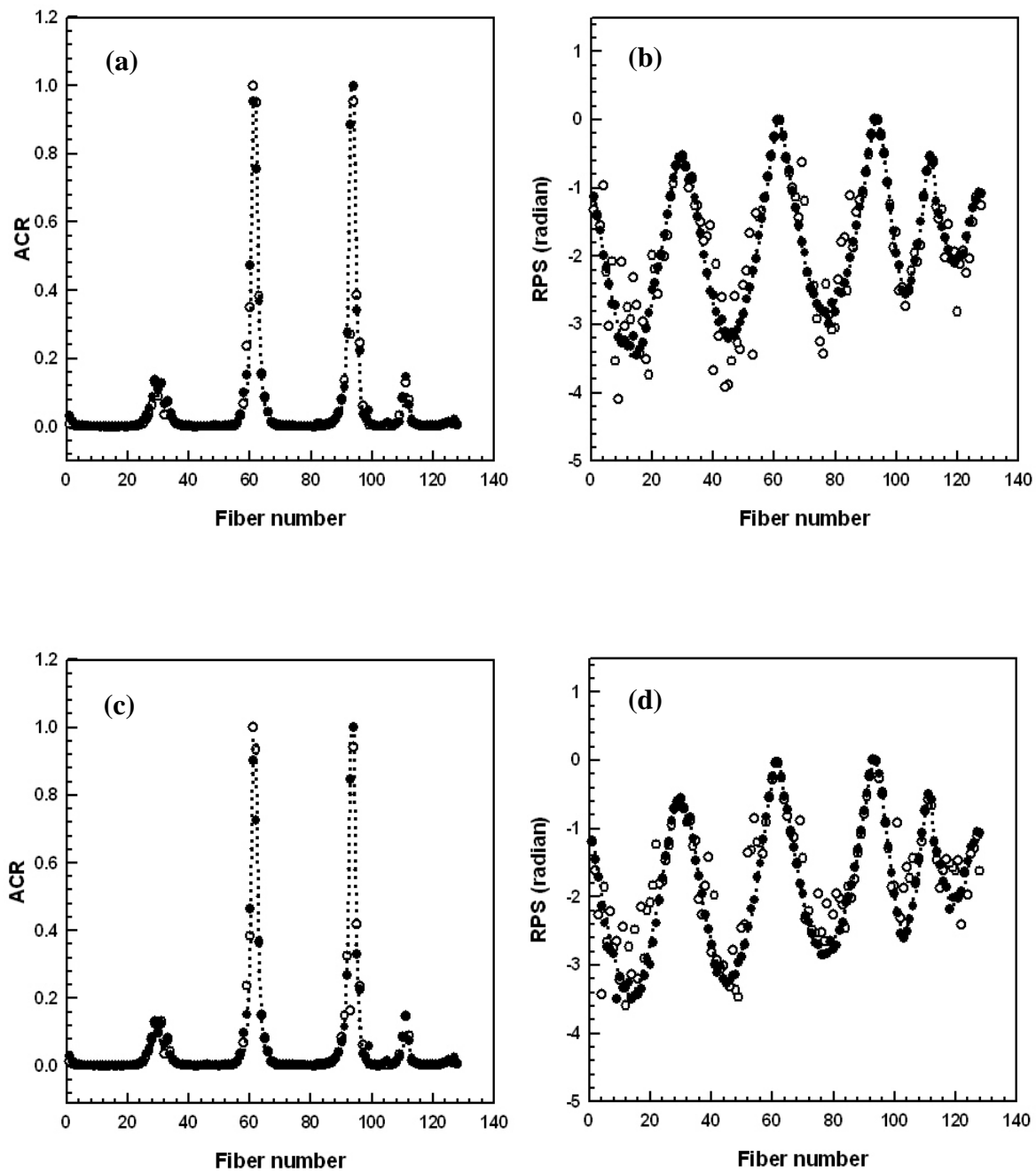


Figure 17 Comparison of amplitude ratio (ACR) ((a),(c),(e)) and relative phase difference (RPS) ((b),(d),(f)) between measurements (symbols) and forward model (dotted line) for a source location (source number 9) as a function of fiber position. The filled circles denote measurements with GRIN lenses while the unfilled symbols denote those without. Target ICG concentration varied to 1  $\mu\text{M}$  ((a), (b)), 0.5  $\mu\text{M}$  ((c), (d)), and 0.25  $\mu\text{M}$  ((e), (f)) at 1.26 cm of target depth.

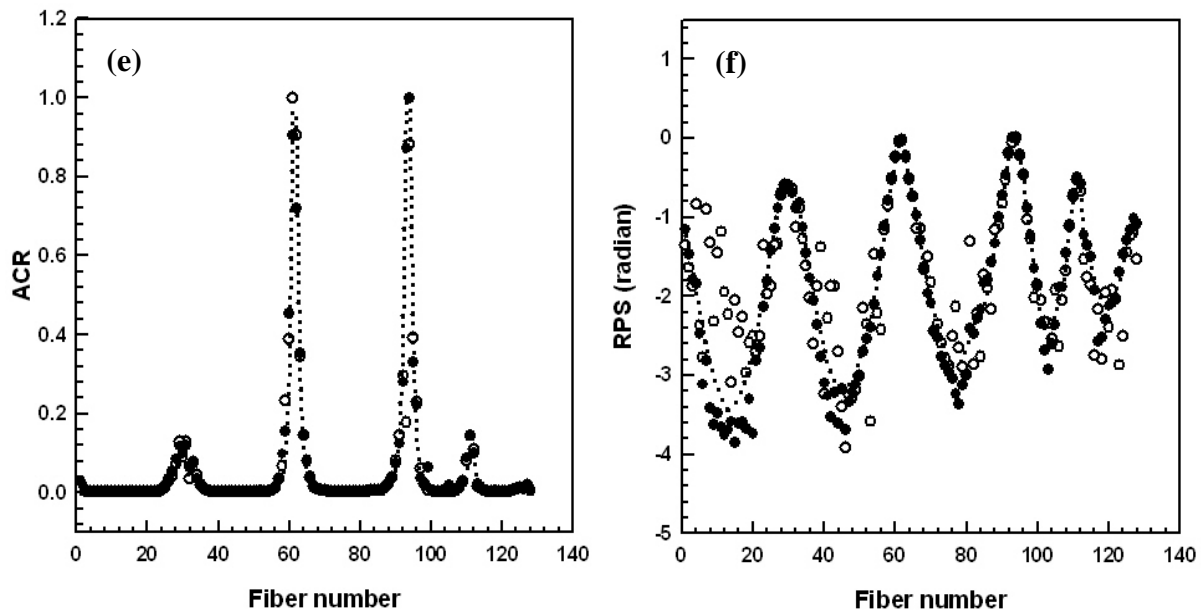


Figure 17 continued

As shown in Figure 18, model mismatch errors increased as target concentration decreased for both ACR and RPS. Additionally, the model match associated with measurements made using the GRIN lens (filled symbols) was improved when compared to that without the GRIN lens (open symbols). Addition of GRIN lenses was more effective in improving model match of RPS than that of ACR.

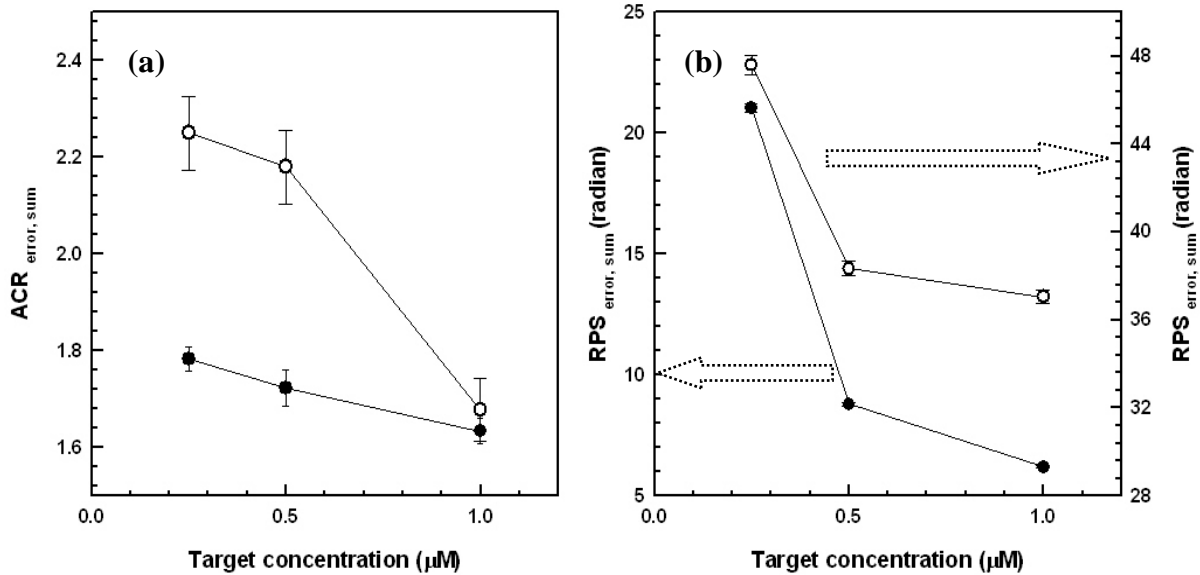


Figure 18 Comparison of mean summation of ACR ((a)) and RPS ((b)) errors between with and without GRIN lens as a function of target concentration. Filled and unfilled circles correspond to the mean mismatch errors with and without GRIN lens respectively. Error bars represent the standard deviation of mean mismatch errors.

For other sources, similar trends were found and summarized in Table 7-8.

Table 7 Mean summation of ACR and RPS errors with GRIN lens as a function of target concentration for 26 sources with GRIN lenses

S# Dep	ACR <sub>error, sum</sub>			RPS <sub>error, sum</sub> (radian)		
	1μM	0.5μM	0.25μM	1μM	0.5μM	0.25μM
1	1.95±.038	1.96±.038	2.11±.037	6.13±.052	11.62±.115	35.17±.304
2	1.82±.051	1.83±.052	2.00±.051	7.77±.061	11.65±.114	22.21±.204
3	2.12±.051	2.06±.051	2.15±.053	8.42±.074	19.00±.154	38.84±.281
4	1.60±.026	2.07±.026	2.48±.037	12.53±.114	21.27±.192	29.40±.243
5	1.51±.026	1.96±.038	2.23±.035	8.46±.091	17.40±.166	25.56±.230
6	2.15±.077	2.21±.075	2.41±.077	7.96±.076	17.66±.165	27.67±.281
7	2.01±.038	2.02±.038	2.06±.051	7.36±.075	10.75±.102	26.00±.281
8	1.66±.038	1.93±.052	2.05±.064	6.60±.050	15.64±.154	44.38±.321
9	1.64±.026	1.73±.038	1.78±.026	6.20±.052	8.79±.077	21.03±.191
10	1.79±.026	2.25±.051	2.29±.052	7.74±.077	13.49±.115	20.85±.190
11	1.68±.051	2.67±.052	2.69±.053	14.36±.075	19.85±.154	29.53±.231
12	2.01±.064	2.82±.053	2.56±.062	18.38±.051	21.57±.152	35.79±.218
13	2.60±.038	2.56±.051	2.69±.051	9.32±.050	12.71±.102	23.54±.154
14	3.65±.038	3.66±.077	3.83±.077	6.91±.051	7.90±.064	13.31±.178

Table 7 continued

S# Dep	1 $\mu$ M	0.5 $\mu$ M	0.25 $\mu$ M	1 $\mu$ M	0.5 $\mu$ M	0.25 $\mu$ M
15	1.97 $\pm$ .051	2.39 $\pm$ .051	2.69 $\pm$ .090	5.67 $\pm$ .053	8.92 $\pm$ .090	22.78 $\pm$ .177
16	2.05 $\pm$ .038	2.16 $\pm$ .038	2.09 $\pm$ .038	6.52 $\pm$ .056	9.65 $\pm$ .091	40.65 $\pm$ .316
17	2.44 $\pm$ .064	2.53 $\pm$ .051	2.82 $\pm$ .052	5.70 $\pm$ .054	8.04 $\pm$ .092	17.88 $\pm$ .214
18	2.47 $\pm$ .064	2.61 $\pm$ .053	2.68 $\pm$ .064	13.93 $\pm$ .112	20.36 $\pm$ .230	27.38 $\pm$ .304
19	3.74 $\pm$ .038	4.35 $\pm$ .078	4.53 $\pm$ .071	22.90 $\pm$ .115	35.07 $\pm$ .242	49.32 $\pm$ .281
20	2.31 $\pm$ .026	2.33 $\pm$ .052	2.39 $\pm$ .052	14.55 $\pm$ .153	23.17 $\pm$ .370	31.09 $\pm$ .358
21	2.53 $\pm$ .038	3.38 $\pm$ .063	3.62 $\pm$ .063	9.38 $\pm$ .141	12.04 $\pm$ .154	15.33 $\pm$ .179
22	1.84 $\pm$ .026	4.36 $\pm$ .065	3.97 $\pm$ .067	26.74 $\pm$ .154	50.64 $\pm$ .230	59.00 $\pm$ .285
23	3.76 $\pm$ .051	4.49 $\pm$ .064	4.03 $\pm$ .061	10.39 $\pm$ .091	15.30 $\pm$ .191	21.56 $\pm$ .217
24	5.15 $\pm$ .102	5.71 $\pm$ .101	6.28 $\pm$ .103	6.89 $\pm$ .078	9.42 $\pm$ .102	13.59 $\pm$ .128
25	9.29 $\pm$ .166	10.80 $\pm$ .194	12.97 $\pm$ .216	15.05 $\pm$ .269	19.30 $\pm$ .263	19.79 $\pm$ .256
26	8.74 $\pm$ .128	9.42 $\pm$ .140	9.93 $\pm$ .142	9.91 $\pm$ .103	14.14 $\pm$ .217	17.93 $\pm$ .243

Table 8 Mean summation of ACR and RPS errors without GRIN lens as a function of target concentration for 26 sources without GRIN lenses

S# Dep	ACR <sub>error, sum</sub>			RPS <sub>error, sum</sub> (radian)		
	1 $\mu$ M	0.5 $\mu$ M	0.25 $\mu$ M	1 $\mu$ M	0.5 $\mu$ M	0.25 $\mu$ M
1	2.69 $\pm$ .064	3.12 $\pm$ .077	3.19 $\pm$ .090	50.62 $\pm$ .410	55.81 $\pm$ .397	62.08 $\pm$ .474
2	2.25 $\pm$ .051	2.37 $\pm$ .065	2.38 $\pm$ .064	54.40 $\pm$ .499	55.36 $\pm$ .474	65.56 $\pm$ .396
3	2.24 $\pm$ .064	2.46 $\pm$ .064	2.48 $\pm$ .063	45.16 $\pm$ .435	46.46 $\pm$ .435	63.08 $\pm$ .474
4	2.47 $\pm$ .062	2.78 $\pm$ .052	3.06 $\pm$ .052	54.87 $\pm$ .525	52.58 $\pm$ .486	63.35 $\pm$ .461
5	2.06 $\pm$ .057	2.24 $\pm$ .064	2.39 $\pm$ .051	46.32 $\pm$ .461	60.77 $\pm$ .512	68.99 $\pm$ .575
6	1.91 $\pm$ .064	2.09 $\pm$ .063	2.30 $\pm$ .077	59.23 $\pm$ .422	61.18 $\pm$ .538	64.04 $\pm$ .482
7	2.38 $\pm$ .063	2.41 $\pm$ .061	2.39 $\pm$ .075	55.88 $\pm$ .576	63.87 $\pm$ .525	59.48 $\pm$ .472
8	2.01 $\pm$ .061	2.16 $\pm$ .064	2.23 $\pm$ .063	42.14 $\pm$ .410	60.26 $\pm$ .576	59.97 $\pm$ .499
9	1.68 $\pm$ .037	2.18 $\pm$ .077	2.25 $\pm$ .077	37.06 $\pm$ .371	38.34 $\pm$ .320	47.60 $\pm$ .422
10	2.20 $\pm$ .039	2.82 $\pm$ .052	2.76 $\pm$ .051	39.67 $\pm$ .422	40.69 $\pm$ .435	49.84 $\pm$ .410
11	1.69 $\pm$ .031	2.19 $\pm$ .051	2.37 $\pm$ .052	45.64 $\pm$ .421	48.20 $\pm$ .397	46.30 $\pm$ .358
12	1.95 $\pm$ .062	2.14 $\pm$ .038	2.52 $\pm$ .054	36.65 $\pm$ .359	43.96 $\pm$ .410	57.93 $\pm$ .448
13	2.00 $\pm$ .038	2.05 $\pm$ .077	2.30 $\pm$ .055	39.58 $\pm$ .397	39.95 $\pm$ .384	40.21 $\pm$ .371
14	3.81 $\pm$ .091	3.83 $\pm$ .075	3.85 $\pm$ 0.91	43.88 $\pm$ .448	41.45 $\pm$ .411	52.74 $\pm$ .410
15	2.50 $\pm$ .062	2.55 $\pm$ .052	2.55 $\pm$ .075	34.68 $\pm$ .397	49.55 $\pm$ .410	51.78 $\pm$ .398
16	1.88 $\pm$ .038	2.01 $\pm$ .037	2.11 $\pm$ .051	40.62 $\pm$ .435	39.24 $\pm$ .320	47.24 $\pm$ .413
17	1.91 $\pm$ .025	2.16 $\pm$ .037	2.48 $\pm$ .054	34.46 $\pm$ .422	34.79 $\pm$ .551	52.29 $\pm$ .474
18	1.97 $\pm$ .026	2.27 $\pm$ .038	2.47 $\pm$ .051	49.14 $\pm$ .576	59.61 $\pm$ .410	57.86 $\pm$ .473
19	2.67 $\pm$ .077	2.87 $\pm$ .064	3.43 $\pm$ .058	46.25 $\pm$ .461	58.44 $\pm$ .422	60.72 $\pm$ .475
20	2.29 $\pm$ .054	2.32 $\pm$ .051	2.68 $\pm$ .053	47.71 $\pm$ .525	50.09 $\pm$ .346	68.02 $\pm$ .483
21	3.71 $\pm$ .052	4.06 $\pm$ .052	3.87 $\pm$ .052	29.24 $\pm$ .474	42.62 $\pm$ .414	47.33 $\pm$ .422
22	3.84 $\pm$ .068	4.11 $\pm$ .038	3.94 $\pm$ .063	40.79 $\pm$ .448	57.28 $\pm$ .371	63.16 $\pm$ .357
23	4.15 $\pm$ .065	4.27 $\pm$ .064	4.47 $\pm$ .064	42.79 $\pm$ .384	50.14 $\pm$ .474	56.28 $\pm$ .483
24	4.68 $\pm$ .102	5.48 $\pm$ .102	5.27 $\pm$ .102	27.55 $\pm$ .397	39.80 $\pm$ .371	48.58 $\pm$ .422
25	10.07 $\pm$ .192	10.98 $\pm$ .192	12.77 $\pm$ .218	30.18 $\pm$ .499	46.64 $\pm$ .332	58.47 $\pm$ .384
26	7.26 $\pm$ .102	10.30 $\pm$ .166	10.23 $\pm$ .141	43.47 $\pm$ .421	45.84 $\pm$ .384	61.89 $\pm$ .435



#### 4.4 Summary

In general, the accuracy of fluorescence-enhanced optical imaging and tomography depends on extracting a small fluorescent signal from an overwhelming and multiply scattered excitation signal. Factors such as fluorophore concentration and target depth which impact the relative amount of fluorescence and excitation light collected. While the use of NIR excitable fluorophores minimizes the background owing to endogenous fluorophores, significant background can arise from excitation light leakage through filters. Since maximal performance of interference filters depends upon normally incident excitation light, the multiple scattering is especially confounding. For example in the breast phantom geometry in which the  $1 \text{ cm}^3$  target of  $1 \text{ }\mu\text{M}$  ICG concentration located  $1 \text{ cm}$  deep within a medium with TBR of 100:1, a weak emission fluence to  $4.14 \times 10^{-8}$  (photons/( $\text{cm}^2 \cdot \text{sec}$ )) can be overwhelmed by a strong excitation fluence of  $2.92 \times 10^{-5}$  (photons/( $\text{cm}^2 \cdot \text{sec}$ )). The orders of magnitude difference between excitation and emission fluence only increases with target depth, TBR, and reduction in target fluorophore concentration. One means to reduce excitation light leakage is to collimate light so that it is normally incident on the interference filters. When using fiber optics to collect point measurements of fluence for tomographic reconstructions, GRIN lenses enable collimation of all emitted light thereby minimizing excitation light leakage. On the other hand when employing direct, planar imaging where the emission light across an area is collected, the image plane can be collimated before directed to the interference filter<sup>70</sup>. However, it is nearly impossible to collimate all multiply scattered light in these

area detection systems. An added strategy may be to use cross polarizers to additionally eliminate the specularly reflect excitation light, which constitutes a substantial portion of the collected excitation light<sup>22, 38</sup>. Nonetheless, the use of GRIN lenses a fiber optic collection of light represents the most efficient manner to collect propagated light and separate emission from excitation contribution. Our contribution shows that improvement of model match by adaptation of GRIN lens optics to the breast phantom is due to improvement of interference filter performance. The improvement in model mismatch should contribute to increased accuracy in image reconstruction as described in objective assessment of image quality<sup>86</sup>, as well as ongoing tomographic reconstructions from actual experimental measurements.

## **5. IMPROVEMENT OF MODEL MATCH IN TWO HETEROGENEITY SYSTEMS**

### 5.1 Introduction

Fluorescence-enhanced optical imaging and tomography has been rapidly developing toward clinical imaging of large tissue volumes and three dimensional (3-D) reconstruction studies<sup>18, 29, 39, 41, 72, 84, 87-96</sup>. Moreover, if measurement approaches can result in sensitive acquisition of signals from small amount of contrast agents and small volume of targets within clinically relevant volumes, molecular optical imaging promises to improve diagnostic imaging and to affect the quality of care for patients with cancer. From a clinical perspective, assessment of the multifocality of the disease is significant, since the cancerous tissues tend to spread metastatically in most cases. However, weak fluorescence signals from the fluorophore are usually dominated by noise arising due to the excitation light leakage through the band-pass and band rejection filters, thus impacting the measurement precision and accuracy, and eventually hindering the accurate reconstruction of the target location and size.

In Section 4, good model matches with measurements using GRIN lenses were presented from the breast phantom study with one target. In this Section, we extend the breast phantom studies to the tomographic imaging of two fluorescent targets with varying target depth at different target separation in order to evaluate Rayleigh resolution<sup>53</sup> in a classical sense. Rayleigh's criterion resolving the two bodies is

described in Appendix F. In the following sections, experimental methods and forward model match studies with and without GRIN lenses are described.

## 5.2 Materials and methods

### 5.2.1 Phantom and instrumentation

Basically, the same experimental set-up and breast phantom as used in the previous study (Section 4) were employed. The targets were glass bulbs of  $0.1 \text{ cm}^3$  volume (0.58 cm diameter) targets were separated from 1.0 to 2.45 cm (center to center) and located at 1.26, 2, and 2.55 cm deep from the hemisphere surface of the phantom. The two targets were filled with  $1 \mu\text{M}$  ICG solution in 1% Liposyn. Figure 19 shows two target locations at 1.26 cm deep and details the three dimensional locations. The positions are summarized in Table 9.

The same FDPM measurement methods as described in Section 4 were conducted using the ICCD homodyne detection system to collect the ACR and RPS with and without GRIN lenses. FDPM measurements were compared with forward model predictions using the same procedure as described in Section 4 for two target-model mismatch studies.

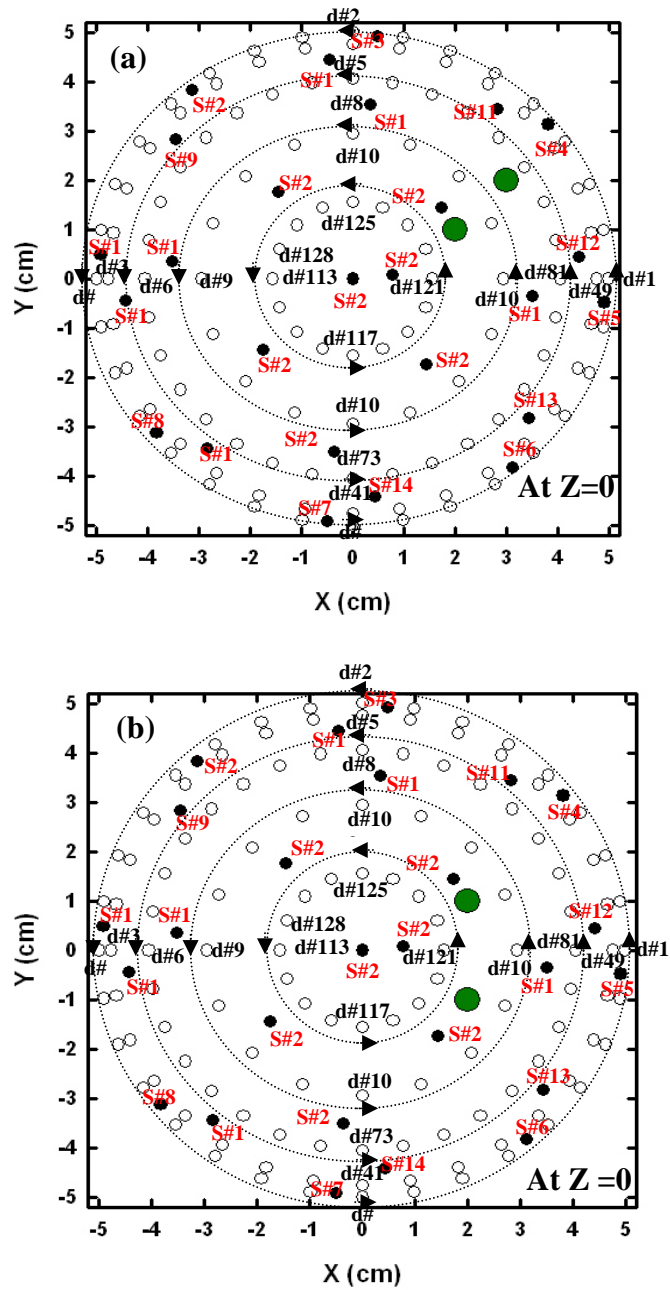


Figure 19 x-y location of all 26 point illumination (black circles), 128 collection fiber locations (open circles), and two target locations (green circles) on the hemispherical portion of the breast phantom. Center to center separations of targets are 2.45 (a), 2.0 (b), and 1.0 cm (c). S# and d# represent source and collection fiber number respectively. Arrows (triangle) indicate numbering direction (counter-clockwise) of 128 collection fibers.

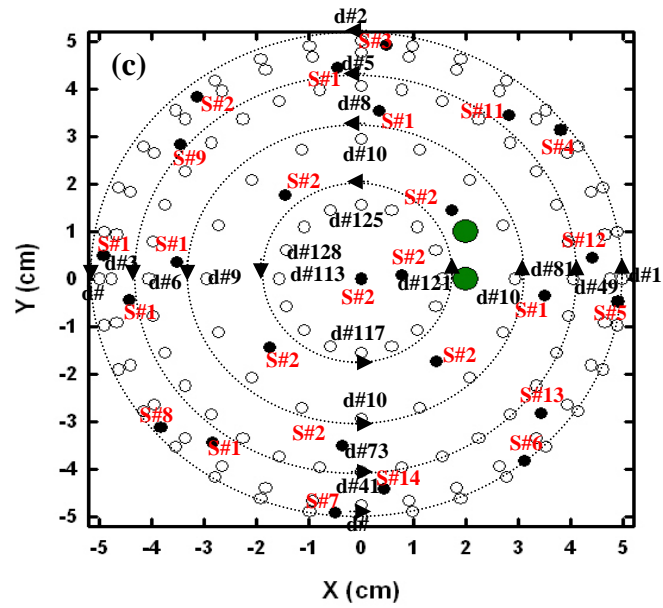


Figure 19 continued

Table 9 ( $x,y,z$ ) coordinates of two targets

Target1	Target2	Target-to-target distance	Target depth
(2.0, 1.0, 3.0)	(3.0, 2.0, 1.0)	2.45 cm	1.26 cm
(2.0, 1.0, 2.0)	(3.0, 0.0, 0.0)	2.45 cm	2.00 cm
(1.0, 1.0, 2.0)	(2.0, -1.0, 1.0)	2.45 cm	2.55 cm
(2.0, 1.0, 3.0)	(2.0, -1.0, 3.0)	2.00 cm	1.26 cm
(2.0, 1.0, 2.0)	(2.0, -1.0, 2.0)	2.00 cm	2.00 cm
(1.0, 1.0, 2.0)	(1.0, -1.0, 2.0)	2.00 cm	2.55 cm
(2.0, 1.0, 3.0)	(2.0, 0.0, 3.1)	1.00 cm	1.26 cm
(2.0, 1.0, 2.0)	(2.0, 0.0, 2.1)	1.00 cm	2.00 cm
(1.0, 1.0, 2.0)	(1.0, 0.0, 2.1)	1.00 cm	2.55 cm

### 5.2.2 The forward problem

The diffusely propagated fluorescence is predicted by the coupled diffusion equations (Equation (1) and (2)) as shown in section 2.1.2. The numerical solutions of the diffusion equations are needed to provide accurate estimates of the fluence on the boundary of tissue for model match with measurements. The numerical solutions for the excitation and emission fluence distributions are obtained using the Robin boundary condition.<sup>32, 97</sup> The Galerkin finite element method with 3-D hexahedral adaptive mesh (33000 hexahedral elements) was used to solve the differential equations (1) and (2). The fluence data determined from the forward model simulations is compared to the measured fluence data in terms of ACR and RPS.

### 5.3 Results and discussion

Figure 20 shows a data set for the model match of ACR ((a), (c), and (e)) and calibrated RPS ((b), (d), and (f)) corresponding to each collection fiber for the two targets separated by 2.45 cm and at a depth of 1.26, 2.0, and 2.55 cm and ICG concentration on 1 $\mu$ M. Filled symbols denote data taken with GRIN lenses while open symbols denote those taken without GRIN lenses. The dotted curves represent lines connecting simulated ACR and RPS at each collection fiber position.

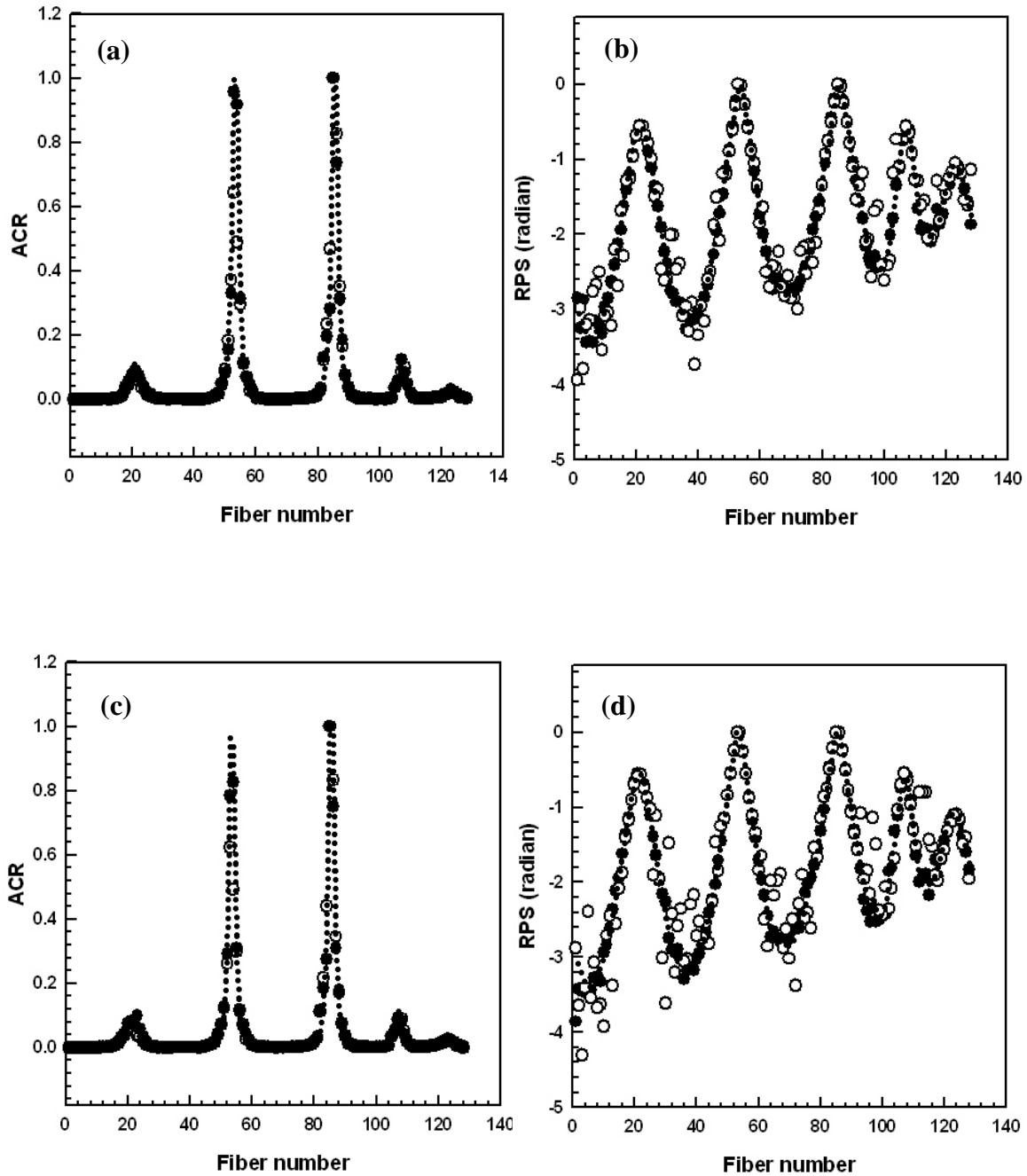


Figure 20 Comparison of amplitude ratio (ACR) ((a),(c),(e)) and relative phase difference (RPS) ((b),(d),(f)) between measurements (symbols) and forward model (dotted line) for two target system as a function of fiber position.. The filled circles denote measurements with GRIN lenses while the unfilled symbols denote those without. Target centroid depth varied from 1.26 cm ((a), (b)), 2.0 cm ((c), (d)), and 2.55 cm ((e), (f)) at 2.45 cm of target to target distance.



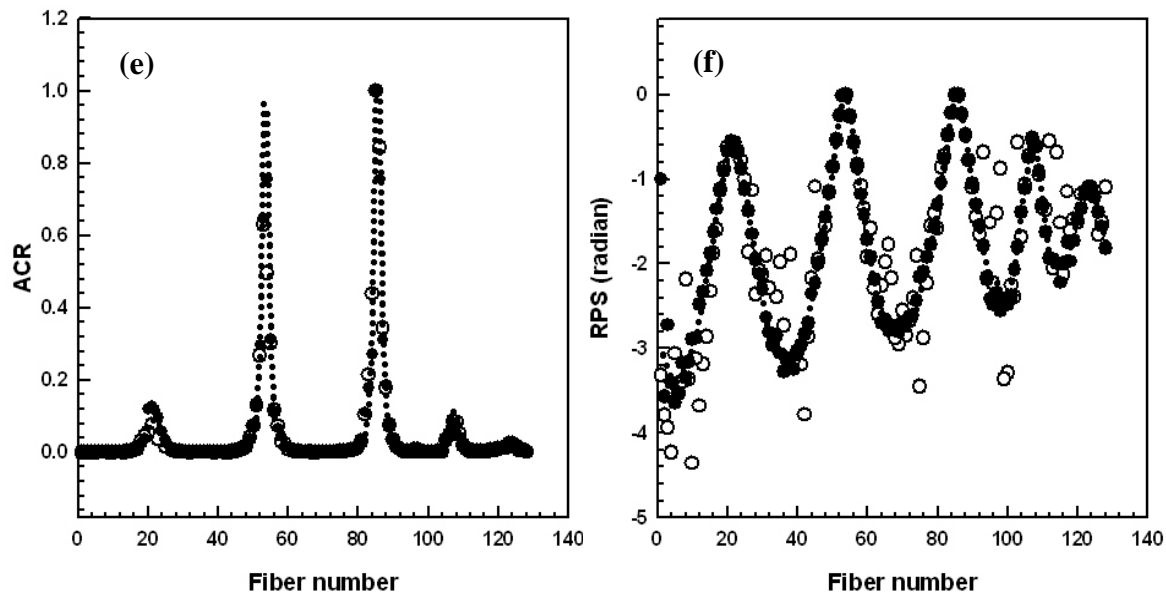


Figure 20 continued

For ACR, a good model match was observed between referenced measurements and simulations for all target depths. However, large model mismatch errors were found in RPS when GRIN lenses were not used as shown in Figure 20 (b),(d), and (f). The errors presumably arose from excitation light leakage by inefficient filter performance as long as model predictions are correct. Figure 21 reports the mean summation error of ACR ((a),(c), and (d)) and calibrated RPS ((b),(d), and (f)) for 128 collection fibers with (filled circles) and without (open circles) GRIN lens collimation as a function of target depth at 2.45 ((a),(b)), 2.0 ((c),(d)), and 1 cm ((e),(f)) of target to target separation. As anticipated, model mismatch errors increased as the target depth increases for ACR and

RPS because weak fluorescent signals at deep target locations can be dominated by high noise floor of excitation light leakage. Mismatch errors arising from data taken using GRIN lenses were less than those taken without GRIN lenses. In particular, the GRIN lens attachments contributed in the improvement of RPS match significantly.

Simple addition of GRIN lenses resulted in advantage of target depth more than 1.29 cm ( $=2.55-1.26$  cm) for ACR and RPS. Specifically, model mismatch errors with GRIN lenses at target depth of 2.55 cm were equal or smaller than those without GRIN lenses at depth of 1.26 cm for all target to target separation.

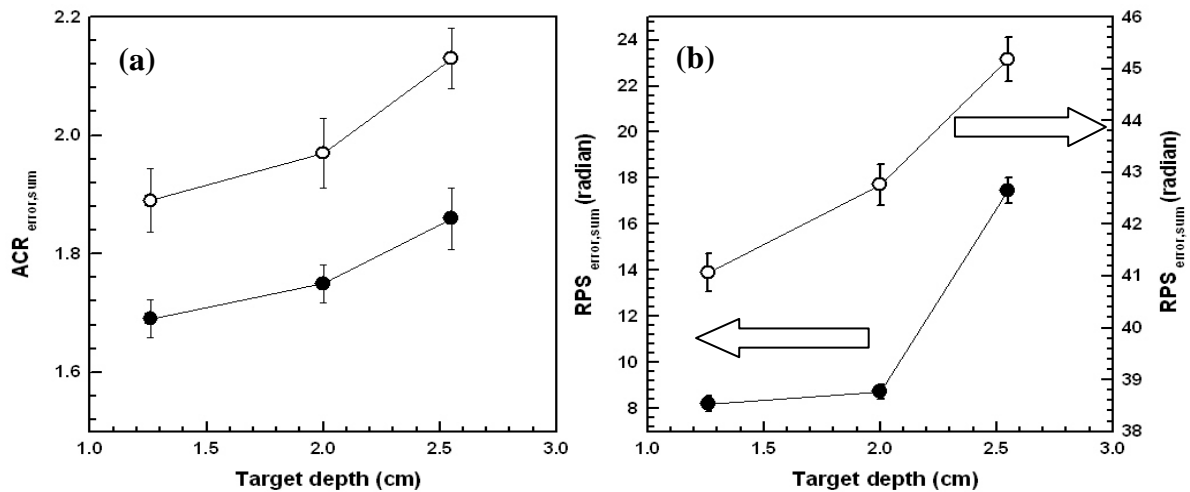


Figure 21 Comparison of mean of ACR ((a),(c), and (e)) and RPS ((b),(d), and (f)) errors between with and without GRIN lens as a function of target depth for 2.45 ((a),(b)), 2.0 ((c),(d)), and 1 cm ((e),(f)) of target to target separation. Filled and unfilled circles correspond to the mean mismatch errors with and without GRIN lenses respectively. Error bars represent the standard deviation of mean mismatch errors.

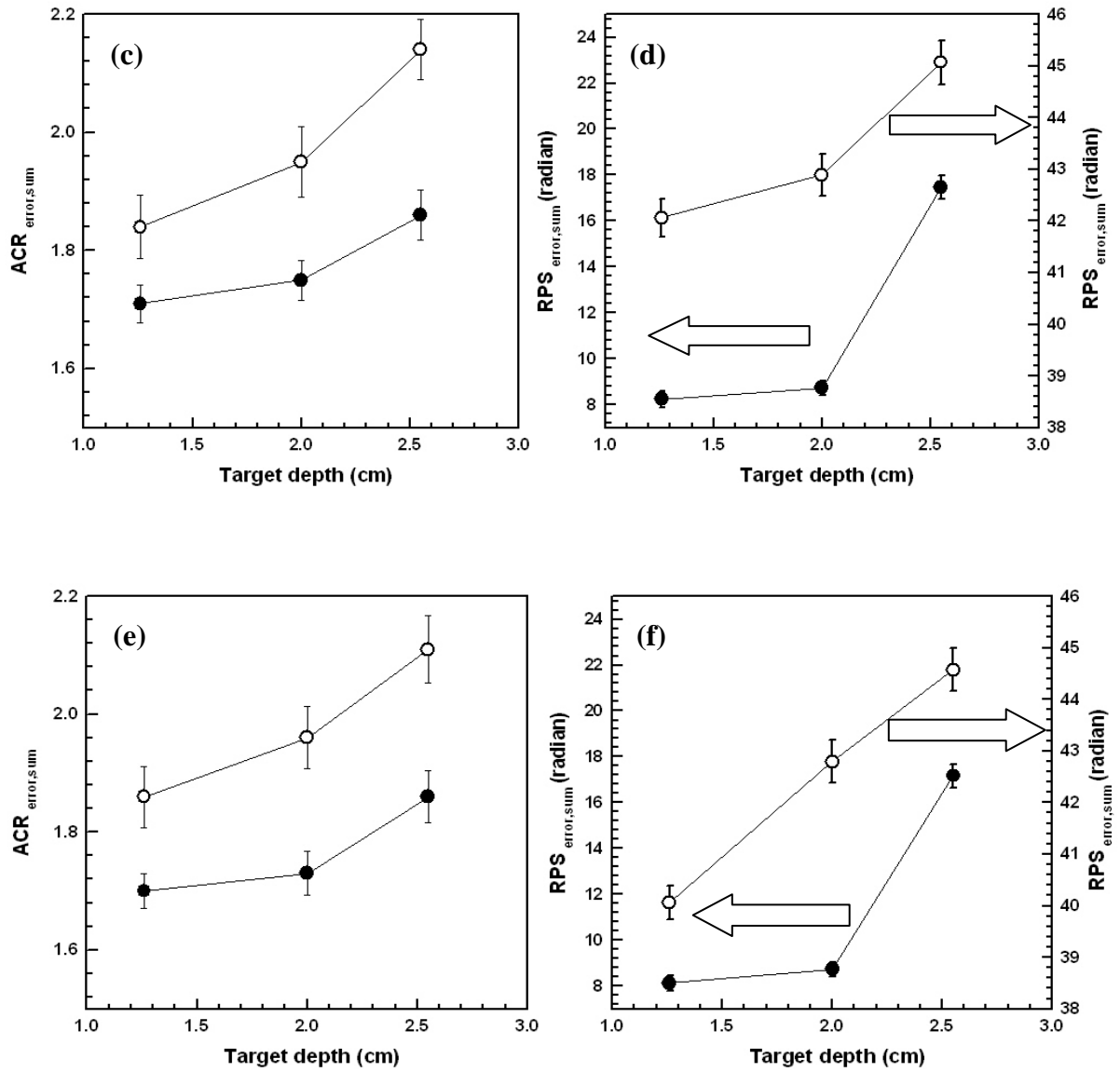


Figure 21 continued

For the remaining 25 source locations, similar trends were found and summarized in Table 10-15.

In Table 10 through 15, there are some exceptional cases for the errors trends of target depth. For example, mismatch errors do not show monotonous increase as target to target depth increases for certain source positions. These inconsistent results could possibly be due to the degree of discretization in the adaptive finite element mesh (from coarse mesh), experimental error in target location, and precision errors in the normalization location of the collection fibers on the curvilinear phantom surface. Apart from the reasons stated above, the major reason for the improvement of model match using GRIN lens especially in RPS is due to efficient rejection of excitation light leakage. This work showed that improvement of model match for two heterogeneities were achieved by adaptation of GRIN lens optics to the breast phantom study in relation to the filter performance. The improvement will eventually contribute in accurate reconstruction of target location and in resolving the multiple heterogeneity of breast tissue.

Table 10 Mean summation of ACR and RPS errors of 128 collection fibers with GRIN lenses as a function of target depth for 26 sources (Target to target separation: 2.45 cm)

S# \ Depth	ACR <sub>error, sum</sub>			RPS <sub>error, sum</sub> (radian)		
	1.26 cm	2.0 cm	2.55 cm	1.26 cm	2.0 cm	2.55 cm
1	1.74±.028	2.20±.035	2.20±.037	6.02±.054	13.85±.084	19.55±.127
2	1.70±.040	1.88±.049	1.98±.047	6.41±.076	8.90±.059	10.07±.092
3	2.21±.045	2.34±.045	2.39±.046	7.31±.056	12.29±.178	20.66±.639
4	2.06±.037	1.95±.031	2.19±.032	9.60±.058	17.63±.114	16.67±.329
5	1.86±.040	1.85±.040	1.98±.067	8.20±.059	15.19±.200	9.98±.104
6	2.09±.068	2.17±.065	2.19±.038	7.77±.061	8.77±.088	13.86±.228
7	2.05±.036	1.95±.032	2.16±.067	7.69±.056	11.69±.205	12.02±.246
8	2.04±.046	2.03±.045	2.04±.038	5.72±.049	11.32±.180	14.86±.306
9	1.84±.031	1.86±.031	1.96±.046	6.66±.038	6.53±.049	14.43±.502
10	2.23±.051	2.34±.052	2.38±.031	5.68±.037	11.30±.216	15.44±.625
11	1.69±.032	1.75±.032	1.86±.052	8.20±.140	8.92±.093	17.47±.549
12	1.82±.044	1.63±.023	1.97±.040	6.92±.069	8.83±.076	10.57±.205
13	3.02±.046	2.49±.041	2.75±.041	7.96±.061	8.96±.077	8.29±.072
14	3.29±.031	3.62±.067	3.78±.050	6.00±.049	10.32±.184	7.28±.067
15	2.20±.051	2.24±.037	2.66±.070	5.50±.047	9.08±.191	9.34±.093
16	2.23±.032	2.36±.036	2.38±.055	7.01±.070	9.34±.177	8.24±.058
17	2.55±.044	2.45±.033	2.78±.036	7.17±.191	12.62±.256	18.51±.609
18	2.20±.046	2.40±.044	2.46±.051	10.38±.136	11.72±.122	13.20±.183
19	3.74±.061	3.77±.065	4.13±.045	11.84±.230	14.72±.147	12.82±.129
20	2.23±.067	2.29±.054	2.39±.068	16.50±.230	17.59±.207	28.28±.452
21	2.26±.056	2.33±.028	3.58±.055	5.57±.134	7.33±.116	8.97±.192
22	3.43±.047	3.84±.045	3.93±.058	5.82±.042	8.23±.058	24.87±.790
23	3.66±.040	3.98±.047	4.52±.047	10.43±.215	9.69±.082	15.85±.554
24	5.22±.051	5.01±.067	5.71±.055	6.21±.050	9.29±.091	8.59±.168
25	8.56±.101	8.98±.177	10.73±.211	4.61±.037	6.53±.058	7.48±.182
26	8.73±.209	9.94±.133	9.87±.141	7.69±.229	7.99±.069	8.00±.128

Table 11 Mean summation of ACR and RPS errors of 128 collection fibers without GRIN lenses as a function of target depth for 26 sources (Target to target separation: 2.45 cm)

S#	Depth	ACR <sub>error, sum</sub>			RPS <sub>error, sum</sub> (radian)		
		1.26 cm	2.0 cm	2.55 cm	1.26 cm	2.0 cm	2.55 cm
1		2.29±.045	3.32±.090	3.12±.084	50.12±.429	54.92±.480	52.36±.470
2		2.18±.054	2.36±.083	2.39±.068	49.28±.352	50.50±.484	57.72±.498
3		2.31±.038	2.45±.082	2.48±.069	50.80±.429	51.30±.563	61.68±.509
4		2.15±.049	3.32±.077	2.69±.060	64.76±.509	66.20±.568	69.12±.525
5		2.14±.074	2.50±.083	2.39±.067	43.58±.357	54.18±.440	55.37±.453
6		1.97±.068	2.05±.065	1.97±.065	56.90±.479	64.42±.540	61.82±.509
7		2.44±.064	2.20±.073	2.46±.065	58.00±.417	60.85±.492	63.40±.536
8		2.15±.067	2.10±.074	2.15±.076	45.25±.406	43.91±.553	49.01±.435
9		2.10±.076	1.97±.076	2.19±.049	32.18±.323	47.23±.429	45.76±.422
10		2.25±.046	2.37±.052	2.36±.051	32.68±.293	41.46±.372	38.22±.346
11		1.89±.054	1.97±.059	2.13±.051	41.06±.365	42.76±.402	45.18±.425
12		1.95±.051	1.99±.056	1.96±.037	33.60±.292	43.05±.428	40.84±.436
13		2.04±.038	2.15±.044	2.06±.041	31.67±.316	36.86±.378	40.77±.428
14		3.38±.073	3.37±.068	3.64±.081	35.06±.312	38.96±.366	52.07±.431
15		2.79±.072	3.08±.081	2.97±.081	34.15±.321	33.50±.346	40.12±.412
16		2.02±.036	2.06±.037	1.96±.037	34.84±.324	36.60±.387	41.05±.402
17		2.15±.033	2.15±.035	2.19±.032	37.93±.352	44.58±.451	45.65±.648
18		2.16±.074	2.09±.088	2.16±.036	55.60±.512	64.46±.594	68.58±.435
19		4.20±.054	4.79±.056	4.95±.083	49.89±.406	50.92±.494	58.75±.621
20		2.24±.049	2.33±.060	2.35±.056	70.51±.559	73.88±.539	73.47±.494
21		3.81±.074	4.45±.063	3.93±.056	40.67±.475	40.91±.399	44.30±.438
22		5.04±.055	4.90±.068	5.50±.070	35.62±.305	36.85±.362	43.83±.465
23		4.01±.060	4.19±.068	4.21±.058	37.43±.367	40.27±.486	37.49±.333
24		3.89±.058	4.60±.100	4.68±.100	34.91±.353	40.09±.406	48.32±.434
25		10.29±.214	10.89±.209	11.58±.221	39.17±.398	40.45±.507	41.28±.453
26		10.16±.155	10.53±.157	11.26±.160	40.27±.425	44.73±.503	45.64±.481

Table 12 Mean summation of ACR and RPS errors of 128 collection fibers with GRIN lenses as a function of target depth for 26 sources (Target to target separation: 2.0 cm)

S# \ Depth	ACR <sub>error_sum</sub>			RPS <sub>error_sum</sub> (radian)		
	1.26 cm	2.0 cm	2.55 cm	1.26 cm	2.0 cm	2.55 cm
1	1.76±.038	2.34±.036	2.40±.033	6.02±.054	13.85±.084	19.55±.127
2	1.70±.041	1.80±.045	1.98±.043	6.41±.066	8.90±.059	10.07±.092
3	2.11±.044	2.31±.048	2.39±.045	7.31±.056	12.29±.178	20.66±.639
4	2.05±.033	1.95±.036	2.19±.042	9.60±.048	15.63±.114	16.67±.329
5	1.89±.042	1.95±.044	1.98±.057	8.20±.059	11.29±.200	10.98±.104
6	2.04±.068	2.17±.075	2.19±.038	7.77±.063	8.77±.088	13.86±.228
7	2.05±.037	1.95±.042	2.16±.057	7.69±.056	11.69±.205	12.02±.246
8	2.05±.048	2.08±.047	2.04±.038	5.72±.040	11.32±.180	14.86±.306
9	1.80±.031	1.86±.036	1.96±.036	6.66±.038	6.53±.049	14.43±.502
10	2.21±.053	2.34±.052	2.38±.041	5.68±.034	11.30±.216	15.44±.625
11	1.71±.032	1.75±.034	1.85±.043	8.23±.140	8.62±.096	16.47±.449
12	1.74±.046	1.63±.025	1.97±.040	6.92±.068	8.83±.076	10.57±.205
13	3.09±.048	2.49±.041	2.75±.041	7.96±.061	9.96±.077	9.49±.072
14	3.19±.031	3.62±.063	3.78±.041	6.00±.031	6.92±.184	7.28±.067
15	2.10±.053	2.24±.032	2.66±.060	5.50±.047	9.18±.191	9.34±.093
16	2.13±.032	2.36±.033	2.38±.055	7.01±.060	9.04±.177	9.25±.058
17	2.38±.043	2.45±.034	2.78±.036	7.17±.191	12.62±.256	18.51±.609
18	2.20±.046	2.40±.044	2.46±.051	10.38±.132	11.72±.122	13.20±.183
19	3.70±.060	3.77±.060	4.13±.045	11.84±.210	14.72±.147	15.82±.129
20	2.24±.063	2.29±.052	2.39±.068	16.50±.220	17.59±.207	28.28±.452
21	3.25±.056	2.33±.038	3.58±.055	5.57±.134	7.33±.116	8.97±.192
22	3.53±.044	3.84±.045	3.93±.058	5.82±.042	8.23±.058	24.87±.690
23	3.46±.040	3.98±.057	4.52±.047	10.43±.215	9.69±.082	15.85±.454
24	5.52±.051	5.01±.067	5.71±.054	6.21±.050	9.29±.081	8.59±.158
25	9.56±.100	9.98±.187	10.73±.201	4.61±.047	6.53±.068	7.48±.142
26	8.73±.202	9.84±.143	9.87±.131	7.69±.229	7.99±.059	8.00±.118

Table 13 Mean summation of ACR and RPS errors of 128 collection fibers without GRIN lenses as a function of target depth for 26 sources (Target to target separation: 2.0 cm)

S# \ Depth	ACR <sub>error, sum</sub>			RPS <sub>error, sum</sub> (radian)		
	1.26 cm	2.0 cm	2.55 cm	1.26 cm	2.0 cm	2.55 cm
1	2.23±.043	3.31±.085	3.32±.082	51.12±.423	54.12±.481	54.36±.472
2	2.16±.053	2.42±.082	2.49±.066	46.28±.350	50.10±.483	57.82±.492
3	2.32±.036	2.41±.081	2.47±.067	51.80±.425	60.30±.560	61.98±.503
4	2.16±.051	3.30±.076	2.99±.061	61.76±.505	64.20±.564	69.42±.522
5	2.15±.076	2.51±.080	2.59±.068	44.58±.356	52.18±.441	55.07±.450
6	1.94±.069	2.03±.066	2.07±.065	54.90±.478	60.22±.541	61.12±.503
7	2.40±.063	2.21±.074	2.42±.063	56.00±.416	60.75±.482	59.40±.532
8	2.13±.066	2.12±.075	2.17±.072	46.25±.402	53.91±.503	49.91±.430
9	2.11±.074	1.99±.077	2.19±.043	33.18±.320	43.23±.439	45.06±.421
10	2.22±.043	2.33±.054	2.39±.053	33.68±.294	42.46±.362	48.22±.342
11	1.84±.054	1.95±.056	2.14±.052	42.06±.373	42.89±.402	45.07±.412
12	1.94±.055	1.98±.057	1.99±.035	32.60±.290	44.05±.424	40.84±.432
13	2.03±.033	2.10±.045	2.08±.040	30.67±.314	35.86±.373	40.77±.422
14	3.36±.075	3.38±.067	3.63±.083	34.06±.311	38.96±.364	50.07±.431
15	2.74±.074	3.04±.080	3.17±.080	33.15±.311	35.50±.345	39.12±.413
16	2.01±.035	2.02±.033	2.06±.037	33.84±.314	36.60±.383	40.05±.401
17	2.16±.034	2.17±.034	2.19±.033	38.93±.332	44.58±.452	44.65±.638
18	2.12±.075	2.09±.088	2.16±.034	56.60±.502	64.16±.592	66.58±.425
19	4.22±.055	4.75±.055	4.96±.080	46.89±.402	50.12±.493	55.75±.611
20	2.25±.046	2.32±.062	2.35±.056	70.51±.539	74.88±.534	73.17±.490
21	3.83±.070	4.35±.064	4.53±.053	43.67±.474	41.91±.395	45.30±.434
22	4.34±.054	4.80±.063	5.51±.071	36.62±.302	34.85±.361	41.83±.462
23	4.04±.061	4.09±.068	4.13±.052	37.03±.362	44.27±.483	47.49±.330
24	3.85±.053	4.63±.101	4.69±.103	34.31±.350	42.09±.404	48.32±.432
25	10.39±.211	10.85±.203	11.59±.211	38.17±.390	43.45±.503	45.28±.451
26	10.29±.152	10.56±.154	11.28±.140	41.27±.423	53.73±.502	55.64±.461



Table 14 Mean summation of ACR and RPS errors of 128 collection fibers with GRIN lenses as a function of target depth for 26 sources (Target to target separation: 1.0 cm)

S#	Depth	ACR <sub>error, sum</sub>			RPS <sub>error, sum</sub> (radian)		
		1.26 cm	2.0 cm	2.55 cm	1.26 cm	2.0 cm	2.55 cm
1		1.76±.037	2.33±.035	2.41±.032	6.01±.053	13.25±.084	19.55±.124
2		1.71±.040	1.81±.045	1.95±.041	6.40±.065	8.30±.059	10.07±.090
3		2.21±.042	2.28±.043	2.34±.042	7.30±.055	12.89±.178	20.66±.637
4		2.15±.033	2.16±.032	2.19±.040	9.61±.047	14.63±.114	16.67±.319
5		1.84±.041	1.92±.043	1.97±.053	8.22±.058	11.19±.200	11.98±.105
6		2.00±.064	2.15±.072	2.19±.033	7.87±.062	8.57±.088	13.86±.218
7		2.01±.037	2.05±.042	2.13±.053	7.63±.055	11.59±.205	12.02±.236
8		2.02±.042	2.08±.044	2.08±.035	5.62±.041	10.22±.180	14.86±.316
9		1.87±.031	1.86±.039	1.93±.033	6.60±.039	6.73±.049	14.43±.512
10		2.25±.050	2.34±.051	2.39±.042	5.78±.033	11.00±.216	15.40±.605
11		1.70±.027	1.73±.033	1.86±.040	8.13±.142	8.72±.096	17.14±.432
12		1.64±.042	1.65±.024	1.98±.046	6.82±.067	8.81±.076	10.53±.202
13		2.09±.048	2.40±.040	2.65±.038	7.86±.060	9.90±.077	9.29±.070
14		3.18±.032	3.62±.065	3.74±.041	6.10±.030	7.32±.184	8.25±.063
15		2.13±.051	2.34±.031	2.69±.061	5.60±.046	9.08±.191	9.32±.092
16		2.10±.032	2.26±.030	2.34±.054	7.11±.061	8.34±.177	9.20±.058
17		2.52±.044	2.49±.036	2.73±.037	7.07±.192	13.62±.256	18.41±.619
18		2.30±.045	2.35±.044	2.43±.051	10.28±.122	12.72±.122	13.10±.173
19		3.68±.061	3.77±.061	4.23±.043	11.54±.200	10.72±.147	10.79±.119
20		2.24±.060	2.28±.053	2.49±.067	16.51±.220	17.29±.207	26.28±.450
21		2.29±.055	2.32±.039	3.59±.055	5.59±.137	7.43±.116	8.87±.182
22		3.54±.044	3.83±.044	3.96±.059	5.84±.045	8.27±.058	24.97±.650
23		3.26±.042	3.90±.053	4.42±.042	10.33±.205	9.49±.082	15.85±.444
24		4.52±.051	5.01±.062	5.61±.051	6.31±.052	9.20±.081	8.79±.138
25		9.46±.101	9.91±.184	10.63±.211	4.51±.048	6.33±.068	7.68±.132
26		8.70±.203	9.74±.142	9.89±.121	7.49±.226	7.79±.059	8.10±.108

Table 15 Mean summation of ACR and RPS errors of 128 collection fibers without GRIN lenses as a function of target depth for 26 sources (Target to target separation: 1.0 cm)

S# \ Depth	ACR <sub>error, sum</sub>			RPS <sub>error, sum</sub> (radian)		
	1.26 cm	2.0 cm	2.55 cm	1.26 cm	2.0 cm	2.55 cm
1	2.25±.042	3.21±.084	3.32±.081	50.12±.413	53.12±.470	55.36±.470
2	2.27±.053	2.40±.081	2.48±.063	47.28±.340	51.10±.484	56.52±.491
3	2.20±.033	2.40±.080	2.46±.062	50.80±.423	61.30±.562	62.04±.500
4	2.14±.051	3.32±.074	2.98±.063	60.76±.502	63.20±.561	67.00±.512
5	2.12±.073	2.53±.081	2.58±.062	43.58±.351	54.18±.443	57.02±.440
6	1.95±.062	2.07±.060	2.08±.061	54.50±.472	60.22±.544	61.15±.513
7	2.44±.061	2.41±.070	2.42±.062	56.30±.414	60.75±.484	60.40±.522
8	2.15±.063	2.22±.073	2.17±.070	46.05±.406	53.91±.513	50.91±.420
9	2.10±.072	2.09±.072	2.15±.042	33.08±.323	43.23±.429	46.06±.411
10	2.20±.044	2.30±.053	2.39±.051	33.80±.291	42.86±.332	46.22±.322
11	1.86±.055	1.96±.056	2.11±.050	40.06±.323	42.39±.412	44.57±.402
12	1.95±.056	1.94±.053	1.98±.030	32.60±.270	44.15±.434	45.84±.422
13	2.07±.035	2.11±.044	2.18±.042	30.67±.324	34.86±.370	41.77±.412
14	3.46±.073	3.30±.066	3.66±.085	34.06±.313	39.96±.360	51.07±.421
15	2.54±.072	3.02±.086	3.14±.085	33.15±.313	36.50±.343	38.12±.411
16	2.11±.033	2.02±.037	2.07±.035	33.84±.312	38.60±.384	41.05±.403
17	2.06±.034	2.12±.037	2.18±.033	38.93±.331	43.58±.452	45.65±.632
18	2.02±.074	2.04±.084	2.26±.032	56.60±.501	63.16±.593	64.58±.424
19	4.12±.053	4.35±.052	4.99±.082	46.89±.400	51.12±.492	54.75±.613
20	2.35±.042	2.39±.067	2.39±.056	70.51±.532	72.88±.535	73.07±.494
21	3.73±.071	4.30±.062	4.53±.052	43.67±.472	43.91±.393	45.80±.435
22	4.24±.052	4.60±.062	5.31±.072	36.62±.301	36.85±.369	41.89±.462
23	4.14±.062	4.19±.064	4.19±.055	37.03±.364	44.37±.485	47.99±.332
24	3.95±.055	4.53±.105	4.63±.105	34.31±.354	40.09±.402	48.12±.422
25	10.09±.221	10.95±.201	11.50±.221	37.17±.392	41.45±.501	44.38±.411
26	10.21±.142	10.96±.150	11.20±.141	42.27±.420	53.93±.500	56.54±.422

## 6. CONCLUSIONS AND SUGGESTED FUTURE WORK

This dissertation focuses on improving the sensitivity of near-infrared (NIR) optical fluorescence imaging and tomography. Specifically, we developed an imaging system for efficient rejection of excitation light by collimating the incident light on the optical filter planes. The developed imaging system was employed for both planar imaging and tomographic imaging study. Small animal molecular imaging with collimation technique for planar system has improved TBR values used to assess the molecular targeting of contrast agents. For a clinically relevant tomographic imaging system, GRIN lens collimation resulted in decrease of model mismatch errors and enabled imaging of one/two targets at greater depths and with lower concentrations of fluorophores. The following points highlight the results of this work.

- Planar imaging systems for improved rejection of excitation light were developed. A new internal design of the frequency domain imager using collimating optics for the area illumination and detection geometry on a tissue phantom was made in order to align the collected excitation and fluorescent light normal to the filter surface. The frequency domain imaging method was employed with an intensity modulated ICCD camera as an area detector to acquire the fluorescence signal to area illumination and detection geometry. Improvement of excitation light rejection was assessed using transmission ratio  $(S(\lambda_x) / (S(\lambda_m) - S(\lambda_x)))$  from measurements conducted with and without

collimating lenses. The addition of collimating optics resulted in a 51 to 75% reduction in the ratio of  $(S(\lambda_x))/ (S(\lambda_m) - S(\lambda_x))$ .

- To translate the implication of phantom planar imaging results for *in vivo* imaging, we extended experiments of excitation light leakage rejection to animal molecular imaging. To quantitatively assess image improvement owing to improved excitation light rejection, we imaged the molecular targeting of the integrin  $\alpha_v\beta_3$  receptor with an arginine-glycine-aspartic acid (RGD) peptide-IRDye<sup>TM</sup>800 conjugate in xenografts of human glioma<sup>62</sup> and assessed improvement in TBR and signal to noise ratio (SNR). The addition of collimating optics resulted in an increase of TBR from 11% to 31% and signal to noise (SNR) from 11% to 142%.
- Tomographic imaging system for efficient collection of fluorescence signals was developed. In this study, we adapted GRIN lenses into an existing frequency-domain tomography system to detect the signals from a clinically relevant breast phantom. This study presented results demonstrating the improvement of model match between experiments and forward simulation models by adaptation of GRIN (Gradient index) lens optics to breast phantom study. In particular, 128 GRIN lenses on the fiber bundle face were employed to align the collected excitation and emission light normal to the filter surface in an existing frequency-domain system. For the improvement of excitation light rejection and enhancing

tomographic imaging, we validated the collimation of incident light on the filter plane by solving the ray tracing equation of designed GRIN lens to the breast phantom study, lowered transmission ratio (R), removed the systematic errors resulting from instrumentation, and improved the model match of tomographic imaging system.

- Improvement of excitation light rejection using GRIN lenses affected two target systems. Mismatch errors arising from data taken using GRIN lenses were less than that those taken without GRIN lenses. Model mismatch errors of ACR and RPS increased as the target depth increases. Model mismatch errors with GRIN lens collimation at target depth of 2.55 cm were equal or smaller than those without GRIN lens collimation at depth of 1.26 cm. Consequently, GRIN lens collimation resulted in increase of target depth (>1.29 cm)

In the future, tomographic reconstruction studies will be performed. Briefly, fluorescence optical tomography is typically performed in a model-based framework wherein a photon transport model in tissue is used to generate predicted boundary fluorescence measurements for a given fluorescence absorption map. The map of the absorption due to fluorophore is then iteratively updated until the predicted boundary fluorescence measurements converge to the actual experimentally observed fluorescence measurements. In our future study to demonstrate improved image resolution in tomographically reconstructed images, we will use existing tomographic algorithm and

measurements made with GRIN lenses in Section 5. More specifically, the algorithm will be derived within a Lagrangian frame work by treating the photon diffusion model as a constraint to the optimization problem<sup>36</sup>. Adaptively refined meshes<sup>37, 38</sup> will be used to separately discretize maps of the forward/adjoint variables and the unknown parameter of fluorescent yield. Currently, tomographic reconstruction has not been accomplished. Presumably, the difficulties preventing tomography arises due to the curved surface of breast phantom which is discretized using adaptive hexahedral elements. We will address this problem using adaptive tetrahedral elements under development by the PML group. This work will be conducted in our group by Dr. Jaehoon Lee and Dr. Amit Joshi.

## REFERENCES

1. Venter, J.C., Adams, M.D., Myers E.U., Li, P.W., Zandieh, A., *et al.* The sequence of the human genome. *Science* **291**, 1304-1351 (2001).
2. Weissleder, R. & Mahmood, U. Molecular imaging. *Radiology* **219**, 316-333 (2001).
3. Sokolov, K., Aaron, J., Hsu, B., Nida, D., Gillenwater, A., *et al.* Real-time vital optical imaging of precancer using anti-epidermal growth factor receptor antibodies conjugated to gold nanoparticles. *Cancer Res* **63**, 1999-2004 (2003).
4. Ntziachristos, V., Bremer, C. & Weissleder, R. Fluorescence imaging with near-infrared light: new technological advances that enable *in vivo* molecular imaging. *Eur Radiol* **13**, 195-208 (2003).
5. Leevy, C.M., Smith, F., Longueville, J., Paumgartner, G. & Howard, M.M. Indocyanine green clearance as a test for hepatic function. Evaluation by dichromatic ear densitometry. *Journal of the American Medical Association* **200**, 236-240 (1967).
6. Kogure, K., Noble, J.D., Ulich, Y. & Earl, C. Infrared absorption angiography of the fundus circulation. *Arch Ophthalmol* **83**, 209-214 (1970).
7. Franceschini, M.A., Moesta, K.T., Fantini, S., Gaida, G., Gratton, E., *et al.* Frequency-domain techniques enhance optical mammography: initial clinical results. *Proceedings of the National Academy of Sciences of the United States of America* **94**, 6468-6473 (1997).

8. Fantini, S., Walker, S.A., Franceschini, M.A., Kaschke, M., Schlag P.M., *et al.* Assessment of the size, position, and optical properties of breast tumors *in vivo* by noninvasive optical methods. *Applied Optics* **37**, 1982-1989 (1998).
9. Moesta, K.T., Fantini, S., Jess, H., Totkas, S., Franceschini, M.A., *et al.* Contrast features of breast cancer in frequency-domain laser scanning mammography. *Journal of Biomedical Optics* **3**, 129-136 (1998).
10. Groesnick, D., Wabnitz, H., Rinneberg, H.H., Moesta, K.T. & Schlag, P.M. Development of a time-domain optical mammography and first *in vivo* applications. *Applied Optics* **38**, 2927-2943 (1999).
11. Pogue, B.W., Poplack, S.P., McBride, T.O., Well, W.A., Osterman, K.S., *et al.* Quantitative hemoglobin tomography with diffuse near-infrared spectroscopy: pilot results in the breast. *Radiology* **218**, 261-266 (2001).
12. Jiang, H., Xu, Y., Iftimia, N., Eggert, N., Klove, L., *et al.* Three dimensional optical tomographic imaging of breast in a human subject. *IEEE Transactions in Medical Imaging* **20**, 1334-1340 (2001).
13. Licha, K. Contrast agents for optical imaging. *Topics in Current Chemistry* **222**, 1-29 (2002).
14. Houston, J.P., Thompson, A.B., Gurfinkel, M. & Sevick-Muraca, E.M. Sensitivity and depth penetration of continuous wave versus frequency-domain photon migration near-infrared fluorescence contrast-enhanced imaging. *Photochemistry and Photobiology* **77**, 420-430 (2003).



15. Weissleder, R., Tung, C.H., Mahmood, U. & Bogdanov, A. *In vivo* imaging of tumors with protease-activated near-infrared fluorescent probes. *Nature Biotechnology* **17**, 375-378 (1999).
16. Ke, S., Wen, X., Gurfinkel, M., Chusilp, C., Fan, Z., *et al.* Near infrared optical imaging of epidermal growth factor receptor in breast cancer xenografts. *Cancer Research* **63**, 7870-7875 (2003).
17. Achilefu, S., Dorshow, R.B., Bugaj, J.E., & Rajagopalan, R. Novel receptor-targeted fluorescent contrast agents for *in vivo* tumor imaging. *Investigative Radiology* **35**, 479-485 (2000).
18. Eppstein, M.J., Hawrysz, D.J., Godavarty, A. & Sevick-Muraca, E.M. Three-dimensional, Bayesian image reconstruction from sparse and noisy data sets: near-infrared fluorescence tomography. *Proceedings of the National Academy of Sciences of the United States of America* **99**, 9619-9624 (2002).
19. Ntziachristos, V., Tung, C.-H., Bremer, C. & Weissleder, R. Fluorescence molecular tomography resolves protease activity *in vivo*. *Nature Medicine* **8**, 757-761 (2002).
20. Shives, E., Xu, Y. & Jiang, H. Fluorescence lifetime tomography of turbid media based on an oxygen-sensitive dye. *Optics Express* **10**, 1557-1562 (2002).
21. Thompson, A.B. & Sevick-Muraca, E.M. NIR fluorescence contrast enhanced imaging with ICCD homodyne detection: measurement precision and accuracy. *Journal of Biomedical Optics* **8**, 111-120 (2003).

22. Thompson, A.B., Hawrysz, D.J. & Sevick-Muraca, E.M. Near-infrared fluorescence contrast-enhanced imaging with area illumination and area detection: the forward imaging problem. *Applied Optics* **42**, 4125-4136 (2003).
23. Godavarty, A., Thompson, A.B., Roy, R., Gurfinkel, M., Eppstein, M.J., *et al.* Diagnostic imaging of breast cancer using fluorescence-enhanced optical tomography: phantom studies. *Journal of biomedical optics* **9**, 488-496 (2004).
24. Chen, X., Conti, P.S. & Moats, R.A. *In vivo* Near-Infrared Fluorescence Imaging of Integrin  $\alpha_3\beta_3$  in Brain Tumor Xenografts. *Cancer Res* **64**, 8009-8014 (2004).
25. Godavarty, A. Fluorescence enhanced optical tomography on breast phantoms with measurements using a gain modulated intensified CCD imaging system. Ph.D. Dissertation (Texas A&M University, College Station; 2003).
26. Chance, B., Leigh, J.S., Miyake, H., Smith, D.S., Nioka, S., *et al.* Comparison of time-resolved and -unresolved measurements of deoxyhemoglobin in brain. *Proceedings of the National Academy of Sciences of the United States of America* **85**, 4971-4975 (1988).
27. Arridge, S.R. & Lionheart, W.R.B. Nonuniqueness in diffusion-based optical tomography. *Optics Letters* **23**, 882-884 (1998).
28. Ishimaru, A. Diffusion of light in turbid media. *Applied Optics* **28**, 2210-2215 (1989).
29. Sevick-Muraca, E.M. & Burch, C. The origin of phosphorescent and fluorescent signals in tissues. *Optics Letters* **19**, 1928-1930 (1994).

30. Patterson, M.S. & Pogue, B.W. Mathematical model for time-resolved and frequency-domain fluorescence spectroscopy in biological tissues. *Applied Optics* **33**, 1963-1974 (1994).
31. Hutchinson, C.L., Troy, T.L. & Sevick-Muraca, E.M. Fluorescence-lifetime determination in tissues or other scattering media from measurements of excitation and emission kinetics. *Applied Optics* **35**, 2325-2332 (1996).
32. Haskell, R.C., Svaasand, L.O., Tsay, T., Feng, T., McAdams M.S., *et al.* Boundary conditions for the diffusion equation in radiative transfer. *Journal of the Optical Society of America A* **11**, 2727-2741 (1994).
33. Godavarty, A., Hawrysz, D.J., Roy, R., Sevick-Muraca, E.M. & Eppstein, M.J. Influence of the refractive index-mismatch at the boundaries measured in fluorescence-enhanced frequency-domain photon migration imaging. *Optics Express* **10**, 653-662 (2002).
34. Paulsen, K.D. & Jiang, H. Spatially varying optical property reconstruction using a finite element diffusion equation approximation. *Medical Physics* **22**, 691-701 (1995).
35. Roy, R. & Sevick-Muraca, E.M. Truncated Newton's optimization scheme for absorption and fluorescence optical tomography: part I theory and formulation. *Optics Express* **4**, 353-371 (1999).
36. Joshi, A., Bangerth, W. & Sevick-Muraca, E.M. Adaptive finite element based on tomography for fluorescent optical imaging in tissue. *Optics Express* **12**, 5402-5417 (2004).

37. Joshi, A., Bangerth, W., Hwang, K., Rasmussen, J. & Sevick-Muraca, E.M. Plane-wave fluorescence tomography with adaptive finite elements *Optics Letters* **31**, 193-195 (2006).
38. Joshi, A., Bangerth, W., Hwang, K., Rasmussen, J. & Sevick-Muraca, E.M. Fully adapted FEM based fluorescence optical tomography from time-dependent measurements with area illumination and detection. *Medical Physics* **33**, 1299-1310 (2006).
39. Godavarty, A., Zhang, C., Eppstein, M.J. & Sevick-Muraca, E.M. Fluorescence-enhanced optical imaging of large phantoms using single and simultaneous dual point illumination geometries. *Medical Physics* **31**, 183-190 (2004).
40. Sevick-Muraca, E.M., Godavarty, A., Houston, J.P., Thompson, A.B. & Roy, R. in Handbook of Biomedical Fluorescence. (eds. B.W. Pogue & M.-A. Mycek) 445-528 (Marcel Dekker, New York; 2003).
41. Roy, R., Thompson, A.B., Godavarty, A. & Sevick-Muraca, E.M. Tomographic fluorescence imaging in tissue phantoms: A novel reconstruction algorithm and imaging geometry. *IEEE Transactions on Medical Imaging* **24**, 137-154 (2005).
42. Hielscher, A.H. Optical tomographic imaging of small animals. *Current Opinion in Biotechnology* **16**, 79-88 (2005).
43. Ntziachristos, V. Would near-infrared fluorescence signals propagate through large human organs for clinical studies? *Optics Letters* **27**, 333-335 (2002).
44. Gurfinkel, M., Thompson, A.B., Ralston, W., Troy, T.L., Moore, A.L., *et al.* Pharmacokinetics of ICG and HPPH-car for the detection of normal and tumor

- tissue using fluorescence, near-infrared reflectance imaging: a case study. *Photochem Photobiol* **72**, 94-102 (2000).
45. Achilefu, S., Jimenez, H.N., Dorshow, R.B., Bugaj, J.E., Webb, E.G., *et al.* Synthesis, *in vitro* receptor binding, and *in vivo* evaluation of fluorescein and carbocyanine peptide-based optical contrast agents. *J. Med. Chem* **45**, 2003-2015 (2002).
  46. Mahmood, U., Tung, C.-H., Tang, Y. & Weissleder, R. Feasibility of *in vivo* multichannel optical imaging of gene expression: experimental study in mice. *Radiology* **224**, 446-451 (2002).
  47. Tung, C.-H., Lin, Y., Moon, W.K. & Weissleder, R. A receptor-targeted near-infrared fluorescence probe for *in vivo* tumor imaging. *ChemBioChem* **3**, 784-786 (2002).
  48. Kircher, M.F., Josephson, L. & Weissleder, R. Ratio imaging of enzyme activity using dual wavelength optical reporters. *Molecular Imaging* **1**, 89-95 (2002).
  49. Chen, Y., Mu, C., Intes, X., Blessington, D. & Chance, B. Near-infrared phase cancellation instrument for fast and accurate localization of fluorescent heterogeneity. *Review of Scientific Instruments* **74**, 3466-3473 (2003).
  50. Funovics, M.A., Weissleder, R. & Mahmood, U. Catheter-based *in vivo* imaging of enzyme activity and gene expression: feasibility study in mice. *Radiology* **231**, 659-666 (2004).

51. Dobrowolski, J.A. in *Handbook of Optics* Vol. 1. (eds. M. Bass, E.W. Van Stryland, D.R. Williams & W.L. Wolfe) 42.89-42.90 (McGraw-Hill, Inc, New York, 1995).
52. Owen, H. in *Handbook of Vibrational Spectroscopy*, Vol. 1. (eds. J.M. Chalmers & P.R. Griffiths) 482-489 (John Wiley & Sons Ltd, New York, 2002).
53. Hecht, E. & Zajac, A. *Optics*, 4th ed. (Addison-Wesley, San Francisco, 2002).
54. Knittel, J., Schnieder, L., Buess, G., Messerschmidt, B. & Possner, T. Endoscope-compatible confocal microscope using a gradient index-lens system. *Optics Communications* **18**, 267-273 (2001).
55. Jung, J.C. & Schnitzer, M.J. *In vivo* epi-fluorescence micro-endoscopy. *Biophysics Journal* **82**, 496-506 (2002).
56. Jung, J.C. & Schnitzer, M.J. Multiphoton endoscopy. *Optics Letters* **28**, 902-904 (2003).
57. Levene, M.J., Dombek, D.A., Kasischke, R.P., Molloy, R.P. & Webb, W.W. *In vivo* multiphoton microscopy of deep tissue. *Journal of Neurophysiology* **91**, 1908-1912 (2004).
58. Zhou, C. & Chen, R.T. Surface-normal 3\*3 non-blocking wavelength-selective crossbar using polymer-based volume holograms. *Applied Physics Letters* **69**, 3990-3992 (1996).
59. Sakamoto, T. Characteristic analysis of laser diode to multimode fiber coupling using a plano-convex gradient-index (GRIN) lens. *Applied Optics* **26**, 2947-2951 (1987).

60. Achilefu, S., Srinivasan, A., Schmidt, M.A., Jimenez, H.N., Bugaj, J.E., *et al.* Novel bioactive and stable neurotensin peptide analogues capable of delivering radiopharmaceuticals and molecular beacons to tumors. *Journal of Medicinal Chemistry* **46**, 3403-3411 (2003).
61. Funovics, M.A., Weissleder, R. & Mahmood, U. Catheter-based *in vivo* imaging of enzyme activity and gene expression: feasibility study in mice. *Radiology* **231**, 609-610 (2004).
62. Wang, W., Ke, S., Wu, Q., Li, C., Gurfinkel, M., *et al.* Near-infrared optical imaging of integrin  $\alpha_v\beta_3$  in human tumor xenografts. *Molecular Imaging* **3**, 343-351 (2004).
63. Rajagopalan, R., Uetrecht, P., Bugaj, J.E., Achilefu, S.A. & Dorshow, R.B. Stabilization of the optical tracer agent indocyanine green using noncovalent interactions. *Photochem. Photobiol.* **71**, 347-350 (2000).
64. Gurfinkel, M. Cancer diagnostics using dynamic near-infrared optical imaging and fluorescent contrast agents. Ph.D. Dissertation (Texas A&M University, College Station; 2004).
65. Montgomery, D.C. & Runger, G.C. in *Applied Statistics and Probability for Engineers*, 2<sup>nd</sup> ed. (ed. W. Anderson) 375-482 (John Wiley & Sons, Inc., New York; 1999).
66. Kwon, S., Ke, S., Gurfinkel, M., Wang, W., Wu, Q., *et al.* Dose-dependent uptakes of an RGD-fluorescent dye-targeted to  $\alpha_v\beta_3$  receptor expressed Kaposi's Sarcoma. *Molecular Imaging* **4**, 75-88 (2005).

67. Lin, Y., Weissleder, R. & Tung, C.-H. Novel near-infrared cyanine fluorechromes: synthesis, properties and bioconjugation. *Bioconjugate Chemistry* **13**, 605-610 (2002).
68. Pham, W., Lai, W.-F., Weissleder, R. & Tung, C.-H. High efficiency synthesis of a bioconjugatable near-infrared fluorochrome. *Bioconjugate Chemistry* **14**, 1048-1051 (2003).
69. Houston, J.P., Ke, S., Wang, W., Li, C. & Sevick-Muraca, E.M. Quality analysis of *in vivo* near-infrared fluorescence and conventional gamma images acquired using a dual-labeled tumor-targeting probe. *Journal of Biomedical Optics* **10**, 054010 (2005).
70. Hwang, K., Houston, J.P., Rasmussen, J.C., Joshi, A., Ke, S., *et al.* Improved excitation light rejection enhances small-animal fluorescent optical imaging. *Molecular Imaging* **4**, 194-204 (2005).
71. Sevick-Muraca, E.M., Lopez, G., Reynolds, J.S., Troy, T.L. & Hutchinson, C.L. Fluorescence and absorption contrast mechanisms for biomedical optical imaging using frequency-domain techniques. *Photochem. Photobiol.* **66**, 55-64 (1997).
72. Li, X.D., Chance, B. & Yodh, A.G. Fluorescence heterogeneities in turbid media, limits for detection, characterization, and comparison with absorption. *Applied Optics* **37**, 6833-6843 (1998).



73. Eppstein, M.J., Dougherty, D.E., Troy, T.L. & Sevick-Muraca, E.M. Biomedical optical tomography using dynamic parameterization and Bayesian conditioning on photon migration measurements. *Applied Optics* **38**, 2138-2150 (1999).
74. Sahu, A.K., Roy, R. & Sevick-Muraca, E.M. Evaluation of anatomical structure and nonuniform distribution of imaging agent in near-infrared fluorescence-enhanced optical tomography. *Optics Express* **13**, 10182-10199 (2005).
75. Koch, B.J., Leger, J.R., Gopinath, A. & Wang, Z. Single-mode vertical cavity surface emitting laser by graded-index lens spatial filtering. *Applied Physics Letter* **70**, 2359-2361 (1997).
76. Buren, M.V. & Riza, N.A. Foundations for low-loss fiber gradient-index lens pair coupling with the self-imaging mechanism. *Applied Optics* **42**, 550-564 (2003).
77. Sun, X., Ma, H., Ming, H., Zheng, Z., Yang, J., *et al.* The measurement of refractive index profile and aberration of radial gradient index lens by using imaging method. *Optics and Laser Technology* **36**, 163-166 (2004).
78. Rector, D.M., Rogers, R.F., Schwaber, J.S., Harper, R.M. & George, J.S. Scattered-light imaging *in vivo* tracks fast and slow processes of neurophysiological activation. *Neuroimage* **14**, 977-994 (2001).
79. Michael, K.L., Taylor, L.C. & Walt, D.R. A far-field-view sensor for making analytical measurements in remote locations. *Analytical Chemistry* **71**, 2766-2773 (1999).

80. Vassiliev, V.V., Ilina, S.M. & Velichansky, V.L. Diode laser coupled to a high-Q microcavity via a GRIN lens. *Applied Physics B-Lasers and Optics* **76**, 521-523 (2003).
81. Rouke, J.L. & Moore, D.T. Birefringence in gradient-index rod lenses:a direct measurement method and interferometric polarization effects. *Applied Optics* **40**, 4971-4980 (2001).
82. Rector, D.M., Rogers, R.F. & George, J.S. A focusing image probe for assessing neural activity *in vivo*. *Journal of Neuroscience Method* **91**, 135-145 (1999).
83. Suparno, Deurloo, K., Stamatelopolous, P., Srivastava, R. & Thomas, J.C. Light scattering with single-mode fiber collimators. *Applied Optics* **33**, 7200-7205 (1994).
84. Godavarty, A., Eppstein, M.J., Zhang, C. & Sevick-Muraca, E.M. Detection of single and multiple targets in tissue phantoms with fluorescence-enhanced optical imaging:feasibility study. *Radiology* **235**, 148-154 (2005).
85. Sakamoto, T. Analytic solutions of the eikonal equation for a GRIN-rod lens. *Journal of Modern Optics* **40**, 503-516 (1993).
86. Sahu, A., Joshi, A. & Sevick-Muraca, E.M. Assessment of a fluorescence-enhanced optical imaging system using the Hotelling observer. *Optics Express* **14**, 7642-7660 (2006).
87. Li, X.D., O'Leary, M.A., Boas, D.A., Chance, B. & Yodh, A.G. Fluorescent diffuse photon density waves in homogenous and heterogeneous turbid media: analytical solutions and applications. *Applied Optics* **35**, 3746-3758 (1996).

88. O'Leary, M.A., Boas, D.A., Chance, B. & Yodh, A.G. Reradiation and imaging of diffuse photon density waves using fluorescent inhomogeneities. *Journal of Luminescence* **60**, 281-286 (1994).
89. O'Leary, M.A., Boas, D.A., Li, X.D., Chance, B., & Yodh A.G. Fluorescence lifetime imaging in turbid media. *Optics Letters* **21**, 158-160 (1996).
90. Schotland, J.C. Continuous-wave diffusion imaging. *JOSA A* **14**, 275-279 (1997).
91. Chernomordik, V., Hattery, D., Gannot, I. & Gandjbakhche, A.H. Inverse method 3-D reconstruction of localized *in vivo* fluorescence application to Sjogren syndrome. *IEEE J.Sel. Top. Quantum Electron.* **54**, 930-935 (1999).
92. Godavarty, A., Eppstein, M.J., Zhang, C. & Sevick-Muraca, E.M. Fluorescence-enhanced optical imaging in large tissue volumes using a gain-modulated ICCD camera. *Phys Med Biol* **48**, 1701-1720 (2003).
93. Ntziachristos, V. & Weissleder, R. Experimental three-dimensional fluorescence reconstruction of diffuse media by use of a normalized Born approximation. *Optics Letters* **26**, 893-895 (2001).
94. Hawrysz, D.J., Eppstein, M.J., Lee, J. & Sevick-Muraca, E.M. Error consideration in contrast-enhanced three-dimensional optical tomography. *Optics Letters* **26**, 704-706 (2001).
95. Lee, J. & Sevick-Muraca, E.M. 3-D fluorescence enhanced optical tomography using referenced frequency-domain photon migration, measurements at emission and excitation measurements. *Journal of the Optical Society of America A* **19**, 759-771 (2001).

96. Eppstein, M.J., Hawrysz, D.J., Godavarty, A. & Sevick-Muraca, E.M. Three-dimensional near-infrared fluorescence tomography with Bayesian methodologies for image reconstruction from sparse and noisy data sets. *Proceedings of the National Academy of Sciences of the United States of America* **99**, 9619-9624 (2002).
97. Keijzer, M., Star, W.M. & Storchi, P.M. Optical diffusion in layered media. *Applied Optics* **27**, 1820-1824 (1988).
98. Reynolds, J., Troy, T.L. & Sevick-Muraca, E.M. Multipixel techniques for frequency-domain photon migration imaging. *Biotech. Progress* **13**, 669-680 (1997).
99. Hildebrand, F.B. *Advanced Calculus for Applications*, 2nd ed. (Prentice Hall, Englewood Cliffs, New Jersey 1976).

## APPENDIX A

### FDPM INSTRUMENTATION

Frequency domain photon migration (FDPM) measurements for fluorescence imaging are performed using the ICCD homodyne detection system throughout this dissertation. The ICCD system is composed of five major components, a laser light source, a couple of optical filters, an image intensifier, frequency synthesizer for sinusoidal modulation of the laser and image intensifier, and a charge-coupled device (CCD) camera.

Figure A1 presents the ICCD homodyne detection system which is also described elsewhere.

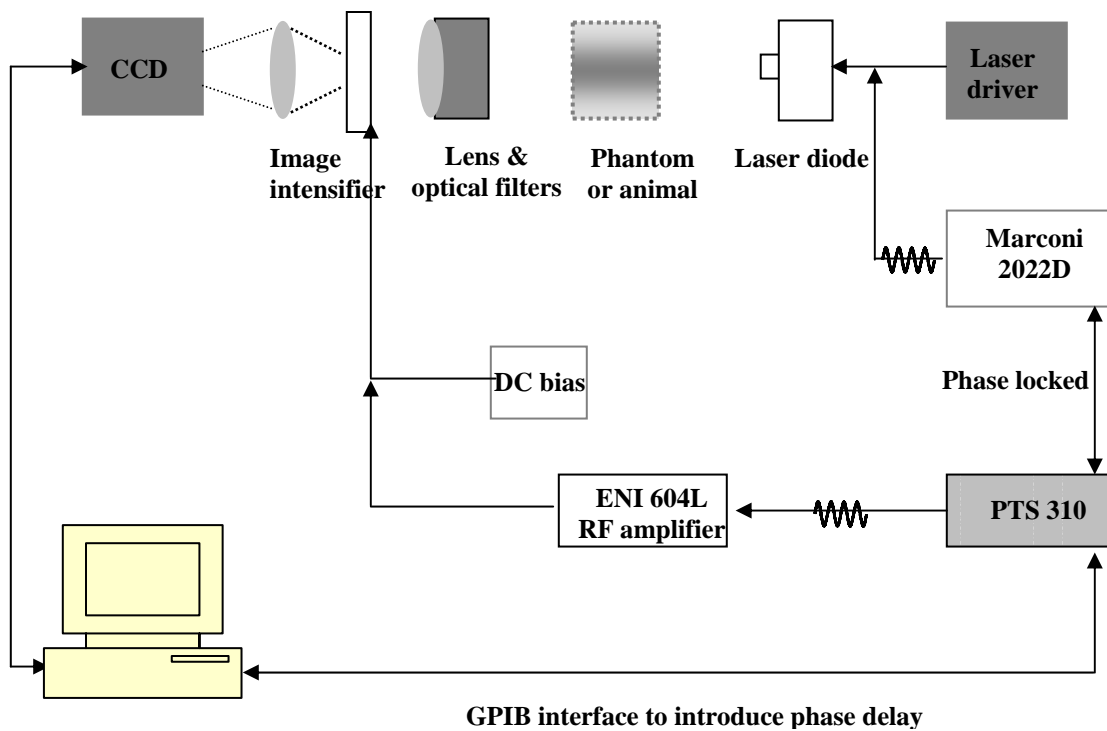


Figure A1 FDPM instrumentation for fluorescence enhanced optical imaging.

### A.1 Illumination source

To excite the target within the tissue phantom, laser beam is incident upon the surface of the Liposyn. Emanating from a laser diode (DL7140-201S, 785nm, 80mW, Thorlabs Inc., NJ for area illumination and HPD1105-9mm-D-78505 model, 530mW, High Power Devices Inc., NJ for point illumination), the incident light penetrates the phantom solution and excites the ICG within the embedded target. The laser diode was driven by laser driver ( model LDC 500, Thorlabs Inc., Newton, NJ) was maintained at a controlled power and constant temperature (16°C) by a temperature controller (model TEC 2000, Thorlabs Inc., Newton, NJ).

### A.2 Optical filters

The optical filter arrangement within the ICCD FDPM instrumentation includes holographic super notch filter (HSPF785.0-2.0, Kaiser Optical system, Ann Arbor, MI: OD > 6.0 at 785nm) and bandpass filter (830FS10-50, Andover, Salem, NH: OD~6 at 785 nm). Figure A2 provides the transmission spectra of the holographic and bandpass filters used in the study.

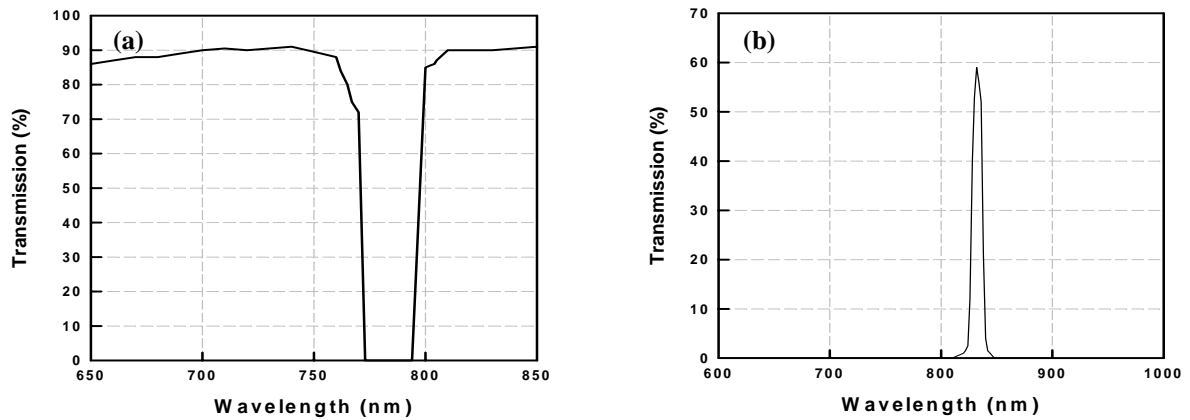


Figure A2 Transmission curve of holographic filter (a) and 830 nm interference filter (b) at zero incident angle.

### A.3 Image intensifier

The image intensifier (ITT Industries Night Vision, model FS9910C, Roanoke, VA) is regarded as a vital component of FDPM ICCD imaging system. The image intensifier is placed at the entry to the CCD array and used for modulation. The intensifier is composed of three main components. A photocathode converts the area light signal formed by focusing lens to an electronic signal. The electronic signal is subsequently received by the multichannel plate, which amplifies the electronic signal via an adjustable voltage, or gain. The phosphor screen converts the amplified signal to an area light signal, which is picked up by a 105-mm AF Micro Nikkor lens to be focused into the CCD array. Measurements with the image intensifier are always conducted in the dark to prevent high intensity light damage.

#### A.4 Modulation instrumentation

Frequency synthesizers enable FDPM measurements through modulation of the light source and image intensifier at the same frequency. Modulation of the laser diode and image intensifier at the same frequency produces a steady state signal that is displayed on the phosphor screen and read by the CCD array. FDPM measurements, are accomplished by sending an oscillating signal to the image intensifier, which induces modulation of the potential between the photocathode and multichannel plate, and phase-delaying the signal at regular intervals over a sinusoidal cycle of 0 to  $2\pi$ . This technique is called as homodyning. Frequency modulation for this study is 100MHz and is produced by two frequency synthesizers. The first synthesizer, which modulates the laser diode, is a Marconi Instrument (model 2022D, Hertfordshire, England) that provides a controllable RF signal for the desired modulation frequency. A second synthesizer (model 310, Programmed Test Sources Inc., Littleton, MA) with amplifier (model 604L, ENI Technology Inc., Rochester, NY) directs a modulation signal to the DC bias of the image intensifier for RF modulation of the detector.

#### A.5 CCD camera

The charge coupled device (CCD) camera (Photometrics Ltd., series AT200, model SI512B, Tucson, AZ) is comprised of a 512\*512-array of photosensitive detectors that convert incident photons into electrons. The total amount of charge that accumulates within a pixel, whose area is typically on the order of  $\mu\text{m}^2$ , is proportional to the product of light intensity and exposure time. Exposure time is controlled by use of a shutter.



Electronic charge is sequentially read out to an output amplifier that converts analog data to 16-bit digital data at a rate of 40,000 pixels per second. The CCD array is thermoelectrically cooled to  $-41^{\circ}\text{C}$  in order to minimize thermally generated electronic charge.

#### A.6 Data acquisition

FDPM data are gathered using a computer program (PMIS Image Processing Software, Photometrics Ltd., Tucson, AZ) that directs the following procedure. The phase of the intensifier modulation is evenly stepped, or delayed, 32 times between 0 and 360 degree relative to the phase of the laser diode modulation via an IEEE-488 general purpose interface bus (GPIB) (National Instruments Corp., Austin, TX). At each phase delay, a phase-sensitive image is acquired by the CCD camera for a given exposure time. The  $512 \times 512$  array of CCD pixels is binned down to a  $128 \times 128$  array during charge readout and before signal digitization. Following completion of the 360 degree phase delay loop, the laser diode is inactivated, and a steady-state image is acquired by the CCD camera using the same exposure time. This image contains ambient light, dark current, and read-out noise. Directed by a Matlab routine (The Mathworks, Inc., Natick, MA), the steady-state image is subtracted from the phase sensitive images; the corrected phase-sensitive images are arranged in the order that they were acquired; and a fast Fourier transform (FFT) is conducted at each pixel to calculate phase ( $\delta$ ) and modulation amplitude ( $I_{AC}$ ) using the following relationships:<sup>98</sup>

$$\delta(i, j) = \arctan\left(\frac{\text{IMAG}[I(f_{\max})_{ij}]}{\text{REAL}[I(f_{\max})_{ij}]}\right) \quad (\text{A1})$$

$$I_{AC}(i, j) = \frac{(\{\text{IMAG}[I(f_{\max})_{ij}]\}^2 + \{\text{REAL}[I(f_{\max})_{ij}]\}^2)^{1/2}}{32/2} \quad (\text{A2})$$

$$I_{DC}(i, j) = \frac{1}{32} \sum_{k=1}^{32} I(i, j, k) \quad (\text{A3})$$

where  $I(f)$  is the Fourier transform of the phase-sensitive intensity data ;  $\text{IMAG}[I(f_{\max})]$  and  $\text{REAL}[I(f_{\max})]$  are the imaginary and real components in the digital frequency spectrum that describe the sinusoidal data;  $I_{DC}(i,j)$  is the average intensity at each pixel.

**APPENDIX B**

**SOURCE AND COLLECTION FIBER LOCATIONS ON BREAST**

**PHANTOM**

B.1 Illumination fiber X-Y-Z locations on the hemispherical surface of the breast phantom

Source number	X (cm)	Y(cm)	Z (cm)
1	-4.91	0.48	0.78
2	-3.13	3.82	0.78
3	0.48	4.91	0.78
4	3.82	3.13	0.78
5	4.91	-0.48	0.78
6	3.13	-3.82	0.78
7	-0.48	-4.91	0.78
8	-3.82	-3.13	0.78
9	-3.44	2.83	2.27
10	-0.44	4.43	2.27
11	2.83	3.44	2.27
12	4.43	0.44	2.27
13	3.44	-2.83	2.27
14	0.44	-4.43	2.27
15	-2.83	-3.44	2.27
16	-4.43	-0.44	2.27
17	-3.52	0.35	3.54
18	0.35	3.52	3.54
19	3.52	-0.35	3.54
20	-0.35	-3.52	3.54
21	-1.44	1.75	4.46
22	1.75	1.44	4.46
23	1.44	-1.75	4.46
24	-1.75	-1.44	4.46
25	0.78	0.08	4.94
26	0	0	5

## B.2 Collection fiber X-Y-Z locations on the hemispherical surface of the breast phantom

Collection fiber number	X(cm)	Y(cm)	Z(cm)
1	-5.00	0.00	0.00
2	-4.90	-0.98	0.00
3	-4.62	-1.91	0.00
4	-4.16	-2.78	0.00
5	-3.54	-3.54	0.00
6	-2.78	-4.16	0.00
7	-1.91	-4.62	0.00
8	-0.98	-4.90	0.00
9	0.00	-5.00	0.00
10	0.98	-4.90	0.00
11	1.91	-4.62	0.00
12	2.78	-4.16	0.00
13	3.54	-3.54	0.00
14	4.16	-2.78	0.00
15	4.62	-1.91	0.00
16	4.90	-0.98	0.00
17	5.00	0.00	0.00
18	4.90	0.98	0.00
19	4.62	1.91	0.00
20	4.16	2.78	0.00
21	3.54	3.54	0.00
22	2.78	4.16	0.00
23	1.91	4.62	0.00
24	0.98	4.90	0.00
25	0.00	5.00	0.00
26	-0.98	4.90	0.00
27	-1.91	4.62	0.00
28	-2.78	4.16	0.00
29	-3.54	3.54	0.00
30	-4.16	2.78	0.00
31	-4.62	1.91	0.00
32	-4.90	0.98	0.00
33	-4.76	0.00	1.55
34	-4.66	-0.93	1.55
35	-4.39	-1.82	1.55
36	-3.95	-2.64	1.55
37	-3.36	-3.36	1.55
38	-2.64	-3.95	1.55
39	-1.82	-4.39	1.55
40	-0.93	-4.66	1.55

41	0.00	-4.76	1.55
42	0.93	-4.66	1.55
43	1.82	-4.39	1.55
44	2.64	-3.95	1.55
45	3.36	-3.36	1.55
46	3.95	-2.64	1.55
47	4.39	-1.82	1.55
48	4.66	-0.93	1.55
49	4.76	0.00	1.55
50	4.66	0.93	1.55
51	4.39	1.82	1.55
52	3.95	2.64	1.55
53	3.36	3.36	1.55
54	2.64	3.95	1.55
55	1.82	4.39	1.55
56	0.93	4.66	1.55
57	0.00	4.76	1.55
58	-0.93	4.66	1.55
59	-1.82	4.39	1.55
60	-2.64	3.95	1.55
61	-3.36	3.36	1.55
62	-3.95	2.64	1.55
63	-4.39	1.82	1.55
64	-4.66	0.93	1.55
65	-4.05	0.00	2.94
66	-3.97	-0.79	2.94
67	-3.74	-1.55	2.94
68	-3.36	-2.25	2.94
69	-2.86	-2.86	2.94
70	-2.25	-3.36	2.94
71	-1.55	-3.74	2.94
72	-0.79	-3.97	2.94
73	0.00	-4.05	2.94
74	0.79	-3.97	2.94
75	1.55	-3.74	2.94
76	2.25	-3.36	2.94
77	2.86	-2.86	2.94
78	3.36	-2.25	2.94
79	3.74	-1.55	2.94
80	3.97	-0.79	2.94
81	4.05	0.00	2.94
82	3.97	0.79	2.94
83	3.74	1.55	2.94
84	3.36	2.25	2.94
85	2.86	2.86	2.94

86	2.25	3.36	2.94
87	1.55	3.74	2.94
88	0.79	3.97	2.94
89	0.00	4.05	2.94
90	-0.79	3.97	2.94
91	-1.55	3.74	2.94
92	-2.25	3.36	2.94
93	-2.86	2.86	2.94
94	-3.36	2.25	2.94
95	-3.74	1.55	2.94
96	-3.97	0.79	2.94
97	-2.94	0.00	4.05
98	-2.72	-1.12	4.05
99	-2.08	-2.08	4.05
100	-1.12	-2.72	4.05
101	0.00	-2.94	4.05
102	1.12	-2.72	4.05
103	2.08	-2.08	4.05
104	2.72	-1.12	4.05
105	2.94	0.00	4.05
106	2.72	1.12	4.05
107	2.08	2.08	4.05
108	1.12	2.72	4.05
109	0.00	2.94	4.05
110	-1.12	2.72	4.05
111	-2.08	2.08	4.05
112	-2.72	1.12	4.05
113	-1.55	0.00	4.76
114	-1.43	-0.59	4.76
115	-1.09	-1.09	4.76
116	-0.59	-1.43	4.76
117	0.00	-1.55	4.76
118	0.59	-1.43	4.76
119	1.09	-1.09	4.76
120	1.43	-0.59	4.76
121	1.55	0.00	4.76
122	1.43	0.59	4.76
123	1.09	1.09	4.76
124	0.59	1.43	4.76
125	0.00	1.55	4.76
126	-0.59	1.43	4.76
127	-1.09	1.09	4.76
128	-1.43	0.59	4.76

---

## APPENDIX C

### RAY TRACING OF GRIN LENS - DETECTOR FIBERS FOR BREAST PHANTOM SYSTEM

#### C.1 Design of GRIN lenses and ray tracing

The objective of the employing the GRIN lenses is to collimate the light delivered from the fiber optics for passage through the interference and bandpass filters. As shown in Figure A3, one end of a collecting fiber contacts the Liposyn solution and the other end of it is attached to the GRIN lens.

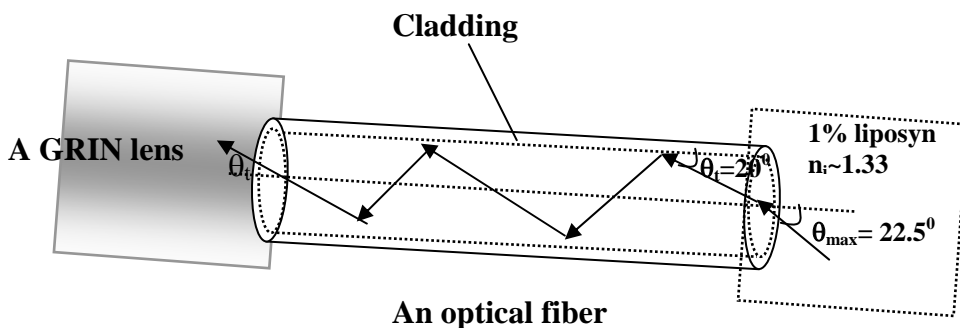


Figure A3 Calculation of incident angle to the GRIN lens from an optical fiber.  $n_i$ ,  $\theta_{\max}$ , and  $\theta_t$  represent the refractive index of the 1% liposyn solution, maximum half of angle of incident light to the optical fiber from the 1% liposyn solution in breast phantom, and maximum incident angle to the GRIN lens respectively.

For the NA of the fibers (NA=0.51), the maximum half angle of light collected,  $\theta_{\max}$  was computed from the Equation (A4).

$$NA = n_i \sin \theta_{\max} = \sqrt{(n_f^2 - n_c^2)} \quad (A4)$$

Where  $n_i$ ,  $n_f$ , and  $n_c$  are the refractive indices of the 1% Liposyn solution, fiber core, and fiber cladding taken to be 1.33, 1.492, and 1.402 respectively. In our system,  $\theta_{\max}$  was found to be  $22.5^\circ$  and at this collection angle, the maximum internal angle ( $\theta_t$ ) for reflection at the interface between fiber core and fiber cladding was found from Snell's law to be  $20^\circ$ . Consequently, the maximum angle of incident light onto the GRIN lens assuming total internal reflection of light inside the fiber was taken to be  $20^\circ$ . GRIN lens properties adopted in ray tracing calculation are as follows. Gradient constant ( $\sqrt{A}$ ), Pitch, and lens refractive index on the optical axis ( $N_0$ ) are  $0.1517 \text{ mm}^{-1}$ , 0.25, and 1.625 respectively. From the Eikonal equation for the ray vector<sup>85</sup>, a lens length of 10.4 mm and a diameter of 4 mm were determined to be necessary for producing collimated light as shown in insert of Figure 12 and detailed solution of the ray tracing equation is presented in following section.

## C.2 Results of Ray tracing of a collection fiber-GRIN lens

The insert of Figure 12 provides the expected ray tracing of the light from a fiber terminating the interfacing plate and directing light through a GRIN lens. For simplicity, ray tracing from one point on the fiber is considered.

Ray tracing of GRIN media is represented by radial position ( $r$ ) and gradient ( $\Phi = \frac{dr}{dz}$ ) of a ray lying in an axial plane. Ray equation (differential equation) for a medium of GRIN rod is derived from Eikonal equation for the ray vector.<sup>85</sup> The differential equation is given by equation (A4) and (A5) and its initial conditions are given by equation A6-A7



$$\frac{d^2 r}{dz^2} = \frac{1}{2N_0 \cos \theta_t} \frac{d(n^2)}{dr} \quad (\text{A4})$$

$$n = N_0 \left( 1 - \frac{(\sqrt{A})^2}{2} r^2 \right) \quad (\text{A5})$$

$$r = 0 \text{ at } z = 0 \quad (\text{A6})$$

$$\frac{dr}{dz} = \tan \theta_t \text{ at } z=0 \quad (\text{A7})$$

where  $r$  is ray height (radial position of ray),  $z$  is lens length,  $n$  is refractive index profile of GRIN lens, and  $\theta_t$  is incident angle of light ( $\leq 20^\circ$ ) to GRIN lens.

The second-order ordinary differential equation with initial conditions was solved for  $r$  as a function of  $z$  using Runge-Kutta method<sup>99</sup> of fourth-order accuracy and  $\theta$  was obtained by differentiating the  $r$  with respect to  $z$ . The numerical error in the results is less than 0.1% based upon the comparison between the solutions at step size of 0.1 and those at step size of 0.05. By solving the above equations for lens design, diameter and length of a GRIN lens were determined to be 4 mm and 10.4 mm respectively.

Numerical solutions of equation (A4) for  $r$  as a function of  $z$  and gradient of  $r$  with respect to  $z$ ,  $\Phi$  are shown in Figure A4.

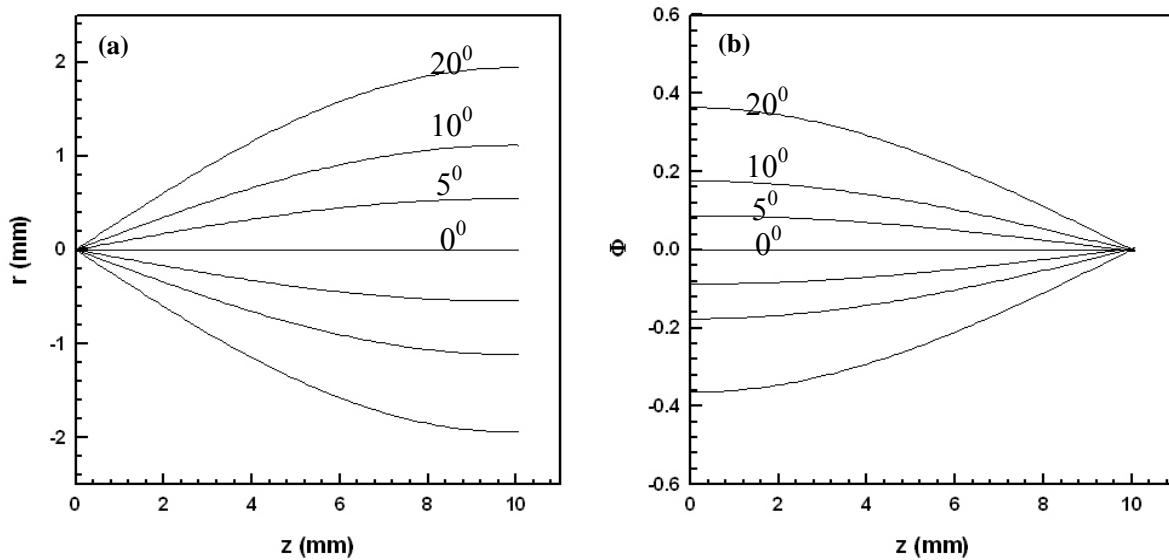


Figure A4 Ray height ( $r$ )(a) and gradient ( $\Phi$ )(b) through ray tracing calculation of the GRIN as a function of lens length ( $z$ ).

Ray height did not exceed the lens diameter (4 mm) for all possible incident angles and angle of departure ( $\theta$ ) converged to zero at the end of the lens. In other words, all possible incident lights leave the lens at zero angles and impinge normally upon the filter plane. Therefore, improvement of excitation light rejection through efficient optical filter performance should be expected to reduce the transmission ratios as well as model mismatch errors.

**APPENDIX D**

**SLOPES AND CORRELATION FACTORS OF LINEAR**

**REGRESSION FOR THE MISMATCH ERRORS**

Source No.	With GRIN Lens			Without GRIN Lens		
	R	Slope	$\hat{\sigma}^2$	R	Slope	$\hat{\sigma}^2$
1	0.990	0.996	0.152	0.890	0.860	0.417
2	0.991	1.005	0.141	0.907	0.836	0.378
3	0.990	0.996	0.147	0.857	1.026	0.588
4	0.990	1.009	0.157	0.871	0.804	0.451
5	0.983	0.967	0.194	0.893	0.935	0.426
6	0.985	0.995	0.196	0.858	0.915	0.491
7	0.990	0.973	0.164	0.918	0.974	0.408
8	0.993	0.998	0.127	0.839	0.825	0.503
9	0.990	1.008	0.154	0.927	0.961	0.327
10	0.985	0.956	0.180	0.895	0.902	0.395
11	0.985	0.956	0.180	0.903	0.866	0.371
12	0.988	0.970	0.161	0.910	0.933	0.378
13	0.989	1.014	0.160	0.901	0.923	0.382
14	0.991	0.988	0.150	0.912	0.911	0.383
15	0.992	0.990	0.132	0.923	0.906	0.351
16	0.993	1.017	0.123	0.904	0.840	0.382
17	0.990	0.947	0.147	0.924	0.920	0.323
18	0.955	0.873	0.291	0.852	0.772	0.491
19	0.969	0.955	0.274	0.875	0.836	0.427
20	0.878	0.832	0.481	0.795	0.794	0.617
21	0.988	0.936	0.181	0.906	0.915	0.386
22	0.995	0.960	0.120	0.879	0.853	0.445
23	0.977	0.940	0.250	0.911	0.923	0.395
24	0.845	0.760	0.595	0.926	0.988	0.349
25	0.978	0.931	0.239	0.918	0.959	0.377
26	0.979	0.968	0.242	0.917	0.910	0.402

## APPENDIX E

### TRANSMISSION RATIO FOR 26 SOURCES

Source No.1	AC Amplitude				DC Intensity			
Collection Fiber No.	Without GRIN lens		With GRIN lens		Without GRIN lens		With GRIN lens	
	Ratio	Std.Dev	Ratio	Std.Dev.	Ratio	Std.Dev.	Ratio	Std.Dev.
1	.006	.0030	.003	.0002	.015	.011	.026	.0012
2	.086	.0535	.029	.0004	.117	.061	.146	.0011
3	.038	.0189	.004	.0003	.098	.014	.030	.0008
4	.042	.0289	.014	.0033	.097	.026	.060	.0007
5	.047	.0240	.008	.0006	.082	.011	.044	.0010
6	.093	.0628	.015	.0016	.135	.010	.072	.0011
7	.199	.0995	.030	.0064	.234	.015	.137	.0008
8	.206	.0459	.059	.0186	.299	.009	.187	.0011
26	.198	.0880	.034	.0055	.341	.013	.147	.0009
27	.114	.0679	.029	.0052	.317	.016	.118	.0010
28	.064	.0289	.021	.0061	.151	.019	.071	.0011
29	.023	.0071	.011	.0002	.059	.006	.041	.0012
30	.019	.0120	.009	.0007	.045	.022	.035	.0012
31	.006	.0035	.003	.0000	.021	.028	.019	.0013
32	.008	.0073	.003	.0002	.024	.060	.024	.0012
33	.024	.0179	.017	.0006	.045	.011	.039	.0013
34	.087	.0574	.055	.0014	.139	.026	.151	.0011
35	.012	.0094	.008	.0013	.024	.027	.019	.0011
36	.019	.0071	.006	.0004	.037	.014	.032	.0012
37	.038	.0140	.029	.0017	.101	.018	.100	.0007
38	.089	.0491	.066	.0083	.128	.017	.117	.0008
39	.106	.0619	.037	.0024	.209	.010	.112	.0009
45	.680	.2934	.012	.0010	.846	.015	.079	.0011
57	.645	.3874	.087	.0196	.289	.017	.252	.0010
58	.162	.0723	.034	.0082	.232	.017	.102	.0012
59	.029	.0085	.036	.0035	.143	.008	.121	.0011
60	.025	.0113	.009	.0001	.079	.014	.042	.0011
61	.022	.0097	.007	.0002	.038	.009	.028	.0007
62	.008	.0012	.004	.0002	.028	.006	.023	.0010
63	.005	.0017	.003	.0002	.016	.014	.012	.0011
64	.007	.0029	.003	.0001	.019	.033	.024	.0009
65	.007	.0032	.005	.0006	.028	.013	.025	.0001
66	.009	.0029	.006	.0004	.023	.008	.014	.0010
67	.032	.0191	.019	.0018	.048	.015	.043	.0011

68	.029	.0191	.011	.0011	.077	.014	.039	.0014
69	.100	.0836	.020	.0009	.198	.021	.054	.0011
70	.144	.0807	.034	.0050	.368	.029	.090	.0008
71	.185	.1438	.070	.0034	.420	.025	.184	.0007
72	.137	.0471	.046	.0059	.293	.012	.135	.0010
89	.427	.1616	.080	.0139	.462	.007	.191	.0011
90	.158	.0418	.030	.0122	.272	.007	.129	.0008
91	.085	.0498	.042	.0074	.257	.016	.132	.0011
92	.084	.0483	.013	.0056	.182	.020	.072	.0008

Source No.2		AC Amplitude				DC Intensity			
Collection Fiber No.	Without GRIN lens Ratio	Without GRIN lens Std.Dev.	With GRIN lens Ratio	With GRIN lens Std.Dev.	Without GRIN lens Ratio	Without GRIN lens Std.Dev.	With GRIN lens Ratio	With GRIN lens Std.Dev.	
1	.120	.0516	.011	.0009	.274	.0151	.050	.0040	
2	.302	.1285	.021	.0017	.608	.0153	.116	.0051	
22	.715	.3832	.050	.0104	.429	.0016	.194	.0042	
23	.254	.1888	.020	.0041	.609	.0036	.116	.0067	
24	.063	.0331	.013	.0044	.185	.0024	.063	.0015	
25	.036	.0214	.008	.0010	.091	.0024	.055	.0030	
26	.013	.0070	.004	.0007	.047	.0023	.045	.0213	
27	.030	.0211	.008	.0010	.055	.0049	.011	.0020	
28	.036	.0259	.006	.0005	.069	.0123	.053	.0081	
29	.028	.0094	.007	.0004	.059	.0045	.046	.0171	
30	.017	.0138	.004	.0007	.049	.0054	.040	.0143	
31	.008	.0047	.003	.0010	.020	.0015	.016	.0035	
32	.021	.0155	.005	.0016	.122	.0042	.033	.0037	
33	.029	.0150	.011	.0011	.111	.0021	.053	.0018	
34	.071	.0383	.032	.0029	.133	.0022	.113	.0059	
35	.157	.0990	.025	.0020	.353	.0039	.082	.0023	
49	.875	.2915	.025	.0020	.850	.0016	.194	.0084	
54	.207	.1415	.032	.0094	.486	.0023	.104	.0043	
55	.069	.0410	.017	.0042	.216	.0021	.070	.0015	
56	.050	.0248	.016	.0036	.138	.0026	.062	.0023	
57	.026	.0229	.029	.0028	.071	.0033	.129	.0122	
58	.018	.0131	.005	.0004	.051	.0045	.061	.0080	
59	.050	.0187	.017	.0010	.083	.0075	.240	.0390	
60	.016	.0110	0.002	.0002	.039	.0088	.035	.0062	
61	.021	.0052	0.001	.0002	.044	.0054	.043	.0032	
62	.014	.0021	0.001	.0001	.029	.0013	.023	.0052	
63	.010	.0043	0.003	.0003	.031	.0018	.028	.0014	
64	.014	.0063	0.004	.0009	.051	.0014	.029	.0020	
65	.044	.0113	0.009	.0019	.126	.0011	.044	.0045	
66	.057	.0178	0.015	.0024	.121	.0064	.058	.0010	
67	.258	.0950	0.060	.0190	.324	.0192	.166	.0020	

68	.450	.2028	0.060	.0283	.469	.0151	.202	.0042
71	.509	.1074	0.008	.0012	.870	.0190	.310	.0221
85	.283	.1539	0.037	.0083	.442	.0012	.137	.0060
86	.123	.0277	0.037	.0029	.325	.0013	.107	.0043
87	.072	.0230	0.033	.0077	.186	.0019	.101	.0041
88	.055	.0404	.035	.0016	.155	.0022	.134	.0041
89	.037	.0148	.012	.0005	.089	.0014	.061	.0052
90	.015	.0029	.008	.0012	.059	.0007	.045	.0015
91	.056	.0444	.016	.0019	.102	.0061	.101	.0050
92	.029	.0151	.006	.0011	.073	.0034	.057	.0012
93	.030	.0118	.008	.0010	.122	.0020	.061	.0063
94	.025	.0118	.006	.0004	.059	.0034	.040	.0031
95	.019	.0094	.008	.0008	.064	.0023	.041	.0013

Source No.3		AC Amplitude				DC Intensity			
Collection Fiber No.	Without GRIN lens Ratio	Without GRIN lens Std.Dev.	With GRIN lens Ratio	With GRIN lens Std.Dev.	Without GRIN lens Ratio	Without GRIN lens Std.Dev.	With GRIN lens Ratio	With GRIN lens Std.Dev.	
20	.058	.0382	.024	.0026	.162	.0015	.032	.0011	
21	.036	.0240	.017	.0009	.098	.0025	.024	.0012	
22	.019	.0151	.012	.0003	.054	.0029	.017	.0012	
23	.015	.0135	.013	.0008	.039	.0038	.019	.0015	
24	.012	.0084	.011	.0003	.027	.0050	.020	.0016	
25	.025	.0217	.022	.0005	.049	.0097	.043	.0011	
26	.011	.0072	.011	.0005	.026	.0024	.023	.0009	
27	.031	.0228	.020	.0020	.060	.0024	.048	.0011	
28	.029	.0140	.017	.0012	.091	.0016	.034	.0013	
29	.052	.0104	.043	.0019	.166	.0009	.049	.0013	
30	.171	.1045	.065	.0113	.225	.0014	.095	.0013	
52	.026	.0142	.022	.0014	.096	.0012	.035	.0011	
53	.018	.0070	.014	.0010	.067	.0015	.022	.0012	
54	.015	.0100	.011	.0006	.034	.0023	.014	.0012	
55	.008	.0073	.013	.0007	.024	.0036	.019	.0011	
56	.015	.0111	.023	.0005	.032	.0067	.031	.0012	
57	.109	.0872	.268	.0092	.168	.0494	.358	.0015	
58	.025	.0201	.039	.0009	.050	.0077	.050	.0012	
59	.038	.0140	.061	.0005	.066	.0035	.075	.0011	
60	.028	.0177	.027	.0015	.059	.0022	.032	.0012	
61	.045	.0110	.030	.0031	.099	.0008	.035	.0011	
62	.073	.0076	.069	.0033	.151	.0007	.050	.0009	
63	.169	.0493	.097	.0079	.296	.0017	.070	.0008	
82	.153	.0333	.096	.0014	.317	.0013	.072	.0013	
83	.083	.0269	.089	.0040	.217	.0020	.066	.0012	
84	.026	.0113	.060	.0026	.111	.0017	.057	.0012	

85	.022	.0067	.019	.0010	.052	.0012	.022	.0012
86	.018	.0047	.022	.0033	.049	.0012	.027	.0011
87	.014	.0043	.021	.0015	.039	.0009	.025	.0014
88	.120	.0692	.108	.0051	.173	.0111	.115	.0012
89	.047	.0197	0.041	.0011	.077	.0029	.047	.0011
90	.019	.0059	0.026	.0009	.038	.0006	.033	.0011
91	.073	.0607	0.060	.0018	.100	.0032	.068	.0010
92	.047	.0307	0.037	.0030	.159	.0026	.048	.0012
93	.185	.0701	0.039	.0027	.600	.0015	.043	.0011
94	.064	.0301	0.058	.0054	.153	.0012	.052	.0013
95	.142	.0466	0.171	.0137	.487	.0029	.107	.0011
107	.076	.0341	0.084	.0063	.333	.0017	.080	.0012
108	.034	.0056	0.044	.0009	.140	.0006	.052	.0012
109	.039	.0097	0.029	.0024	.110	.0012	.035	.0011
110	.053	.0199	0.039	.0022	.108	.0011	.042	.0012
111	.078	.0357	0.041	.0038	.207	.0023	.049	.0016

Source No.4		AC Amplitude				DC Intensity			
Collection Fiber No.	Without GRIN lens Ratio	Without GRIN lens Std.Dev.	With GRIN lens Ratio	With GRIN lens Std.Dev.	Without GRIN lens Ratio	Without GRIN lens Std.Dev.	With GRIN lens Ratio	With GRIN lens Std.Dev.	
15	.108	.0570	.022	.0061	.200	.0021	.057	.0011	
16	.089	.0641	.014	.0010	.222	.0042	.047	.0012	
17	.026	.0140	.015	.0011	.080	.0013	.036	.0009	
18	.032	.0153	.012	.0010	.052	.0021	.038	.0011	
19	.021	.0060	.007	.0002	.040	.0021	.033	.0006	
20	.012	.0090	.002	.0003	.024	.0052	.021	.0012	
21	.008	.0070	.002	.0001	.026	.0052	.018	.0011	
22	.009	.0092	.002	.0012	.027	.0033	.015	.0011	
23	.017	.0141	.004	.0013	.072	.0040	.015	.0011	
24	.024	.0154	.005	.0011	.112	.0022	.020	.0012	
25	.064	.0391	.012	.0024	.157	.0020	.037	.0010	
26	.154	.0700	.019	.0050	.260	.0021	.061	.0012	
27	.404	.2531	.036	.0112	.370	.0013	.117	.0011	
46	.170	.1130	.041	.0063	.393	.0030	.080	.0012	
47	.068	.0390	.011	.0060	.185	.0022	.037	.0011	
48	.040	.0281	.006	.0012	.107	.0035	.028	.0015	
49	.016	.0061	.005	.0003	.044	.0010	.015	.0012	
50	.009	.0042	.003	.0001	.032	.0012	.014	.0011	
51	.010	.0043	.002	.0004	.024	.0020	.015	.0010	
52	.030	.0172	.007	.0001	.050	.0102	.046	.0011	
53	.010	.0053	.001	.0002	.023	.0040	.016	.0011	
54	.010	.0091	.001	.0002	.024	.0033	.012	.0014	
55	.008	.0072	.002	.0001	.032	.0024	.012	.0007	

56	.020	.0103	.004	.0002	.060	.0023	.020	.0012
57	.035	.0203	.027	.0022	.101	.0030	.057	.0011
58	.115	.0772	.019	.0042	.292	.0042	.031	.0013
59	.135	.0401	.046	.0132	.243	.0010	.097	.0010
63	.993	.3721	.035	.0032	.846	.0022	.116	.0011
78	.224	.1021	.024	.0052	.330	.0020	.061	.0011
79	.148	.0861	.011	.0022	.457	.0032	.045	.0011
80	.079	.0632	.010	.0021	.139	.0020	.029	.0012
81	.032	.0233	.005	.0023	.112	.0032	.021	.0013
82	.016	.0051	.003	.0004	.041	.0010	.015	.0029
83	.013	.0040	.004	.0002	.042	.0022	.018	.0014
84	.011	.0050	.003	.0001	.027	.0020	.016	.0014
85	.011	.0040	.002	.0002	.025	.0022	.012	.0014
86	.015	.0053	.005	.0001	.038	.0010	.019	.0017
87	.015	.0043	.004	.0001	.052	.0012	.024	.0020
88	.076	.0342	.038	.0052	.127	.0030	.075	.0012
89	.055	.0132	.015	.0021	.195	.0012	.043	.0014
90	.131	.0212	.016	.0021	.222	.0010	.049	.0015
105	.073	.0242	.009	.0021	.213	.0012	.045	.0013
106	.058	.0242	.010	.0011	.202	.0010	.054	.0012
107	.037	.0122	.009	.0010	.167	.0012	.045	.0008

Source No.5		AC Amplitude				DC Intensity			
Collection	Without GRIN lens		With GRIN lens		Without GRIN lens		With GRIN lens		
Fiber No.	Ratio	Std.Dev.	Ratio	Std.Dev.	Ratio	Std.Dev.	Ratio	Std.Dev.	
10	.273	.1059	.027	.0063	.691	.0020	.105	.0014	
11	.092	.0359	.042	.0074	.289	.0021	.112	.0011	
12	.031	.0093	.017	.0004	.122	.0014	.046	.0008	
13	.034	.0157	.012	.0021	.110	.0018	.041	.0007	
14	.018	.0104	.006	.0006	.045	.0025	.018	.0010	
15	.011	.0093	.006	.0005	.032	.0041	.023	.0011	
16	.015	.0114	.009	.0003	.035	.0071	.039	.0008	
17	.058	.0386	.034	.0005	.088	.0167	.126	.0011	
18	.037	.0139	.020	.0005	.069	.0053	.063	.0009	
19	.019	.0044	.013	.0006	.050	.0012	.043	.0010	
20	.020	.0123	.009	.0030	.123	.0032	.022	.0011	
21	.051	.0341	.014	.0016	.176	.0028	.041	.0012	
22	.168	.1318	.035	.0050	.451	.0032	.067	.0012	
24	1.140	.2315	.030	.0012	.905	.0013	.111	.0013	
42	.181	.0934	.033	.0077	.347	.0028	.079	.0012	
43	.090	.0461	.030	.0050	.287	.0019	.076	.0013	
44	.042	.0210	.009	.0007	.133	.0028	.031	.0011	
45	.019	.0111	.009	.0004	.051	.0027	.018	.0011	
46	.063	.0456	.035	.0011	.086	.0080	.082	.0012	
47	.010	.0081	.005	.0003	.022	.0046	.018	.0007	



48	.011	.0107	.005	.0001	.023	.0077	.023	.0008
49	.015	.0049	.005	.0000	.028	.0043	.023	.0009
50	.011	.0046	.006	.0002	.027	.0028	.023	.0011
51	.009	.0031	.007	.0006	.032	.0016	.018	.0010
52	.024	.0126	.012	.0005	.053	.0019	.027	.0012
53	.030	.0132	.012	.0022	.116	.0015	.030	.0011
54	.098	.0780	.017	.0024	.196	.0025	.038	.0011
55	.192	.0955	.028	.0077	.457	.0032	.091	.0007
73	.406	.1318	.065	.0123	.761	.0030	.144	.0010
74	.307	.0855	.064	.0107	.418	.0005	.128	.0011
75	.204	.0708	.312	.0219	.235	.0019	.446	.0009
76	.077	.0380	.048	.0031	.188	.0032	.079	.0001
77	.036	.0136	.015	.0017	.081	.0013	.036	.0010
78	.016	.0096	.006	.0001	.065	.0027	.017	.0011
79	.017	.0096	.007	.0003	.051	.0024	.021	.0014
80	.011	.0088	.005	.0012	.043	.0038	.018	.0011
81	.023	.0216	.007	.0003	.046	.0035	.023	.0008
82	.009	.0028	.006	.0006	.040	.0014	.016	.0007
83	.020	.0086	.009	.0009	.052	.0018	.021	.0010
84	.018	.0078	.014	.0010	.080	.0024	.036	.0011
85	.034	.0126	.012	.0028	.109	.0014	.029	.0008
87	.155	.0480	.058	.0118	.458	.0009	.124	.0011
103	.171	.0806	.134	.0183	.515	.0036	.268	.0008
105	.031	.0087	.011	.0015	.150	.0015	.031	.0013

Source No.6		AC Amplitude				DC Intensity			
Collection Fiber No.	Without GRIN lens Ratio	Without GRIN lens Std.Dev.	With GRIN lens Ratio	With GRIN lens Std.Dev.	Without GRIN lens Ratio	Without GRIN lens Std.Dev.	With GRIN lens Ratio	With GRIN lens Std.Dev.	
7	.085	.0479	.023	.0066	.287	.0019	.069	.0015	
8	.046	.0233	.013	.0042	.152	.0024	.041	.0011	
9	.030	.0140	.006	.0004	.117	.0025	.035	.0012	
10	.018	.0089	.002	.0008	.062	.0029	.030	.0031	
11	.061	.0297	.013	.0014	.088	.0072	.084	.0012	
12	.012	.0045	.003	.0002	.028	.0038	.023	.0011	
13	.021	.0137	.005	.0005	.034	.0047	.030	.0011	
14	.010	.0069	.002	.0002	.026	.0035	.018	.0012	
15	.020	.0150	.003	.0009	.046	.0030	.022	.0008	
17	.061	.0290	.012	.0026	.173	.0019	.048	.0010	
18	.100	.0339	.037	.0073	.178	.0010	.066	.0009	
38	.289	.1561	.068	.0194	.346	.0030	.176	.0011	
39	.066	.0267	.012	.0021	.172	.0020	.060	.0013	
40	.097	.0430	.021	.0017	.155	.0023	.101	.0011	
41	.038	.0246	.011	.0014	.114	.0040	.084	.0009	
42	.020	.0104	.004	.0006	.036	.0025	.037	.0011	
43	.034	.0143	.004	.0003	.054	.0037	.046	.0014	

44	.013	.0096	.002	.0003	.030	.0081	.028	.0011
45	.019	.0137	.002	.0001	.032	.0091	.023	.0012
46	.109	.0792	.022	.0014	.146	.0257	.138	.0013
47	.013	.0089	.001	.0003	.032	.0035	.019	.0017
48	.023	.0153	.003	.0004	.069	.0036	.021	.0011
49	.031	.0081	.008	.0017	.104	.0013	.025	.0011
50	.064	.0216	.016	.0043	.207	.0013	.066	.0013
51	.240	.1037	.034	.0046	.351	.0024	.075	.0012
70	.293	.0993	.050	.0155	.826	.0037	.125	.0013
71	.148	.0889	.018	.0016	.391	.0049	.076	.0014
72	.032	.0131	.012	.0016	.081	.0016	.052	.0014
73	.040	.0079	.017	.0011	.094	.0009	.082	.0033
74	.082	.0062	.020	.0015	.106	.0007	.160	.0012
75	.457	.1087	.127	.0051	.568	.0226	3.153	.0014
76	.199	.1115	.024	.0008	.232	.0201	.217	.0014
77	.086	.0292	.004	.0004	.102	.0052	.049	.0012
78	.028	.0219	.003	.0008	.057	.0035	.025	.0012
79	.026	.0144	.005	.0011	.086	.0025	.026	.0010
80	.065	.0454	.006	.0007	.139	.0038	.023	.0013
81	.075	.0492	.012	.0045	.250	.0034	.042	.0014
82	.080	.0283	.015	.0036	.244	.0022	.047	.0015
83	.149	.0461	.033	.0038	.325	.0015	.098	.0010
99	.225	.0398	.020	.0034	.549	.0018	.180	.0014
100	.081	.0620	.022	.0035	.228	.0014	.089	.0012
101	.179	.0506	.058	.0066	.321	.0028	.260	.0011
102	.096	.0430	.024	.0078	.486	.0026	.148	.0011
103	.184	.1175	.051	.0102	.284	.0033	.222	.0080

Source No.7		AC Amplitude				DC Intensity			
Collection Fiber No.	Without GRIN lens Ratio	Without GRIN lens Std.Dev.	With GRIN lens Ratio	With GRIN lens Std.Dev.	Without GRIN lens Ratio	Without GRIN lens Std.Dev.	With GRIN lens Ratio	With GRIN lens Std.Dev.	
6	.009	.0070	.006	.0003	.040	.0028	.025	.0011	
7	.008	.0072	.005	.0001	.028	.0042	.022	.0009	
8	.012	.0083	.005	.0003	.030	.0065	.025	.0008	
9	.010	.0066	.005	.0001	.023	.0043	.020	.0007	
10	.013	.0097	.005	.0003	.028	.0030	.024	.0010	
11	.040	.0191	.016	.0015	.067	.0031	.054	.0011	
12	.013	.0054	.006	.0004	.071	.0016	.029	.0008	
13	.084	.0475	.009	.0013	.264	.0025	.057	.0011	
14	.130	.0776	.012	.0011	.303	.0036	.052	.0009	
15	.199	.0863	.027	.0148	.272	.0013	.071	.0010	
34	.113	.0462	.030	.0044	.313	.0021	.094	.0010	
35	.055	.0352	.013	.0051	.160	.0024	.048	.0012	
36	.029	.0112	.013	.0034	.092	.0018	.043	.0012	
37	.034	.0158	.037	.0023	.077	.0026	.112	.0013	

38	.119	.0865	.100	.0055	.205	.0190	.331	.0012
39	.022	.0134	.013	.0009	.045	.0066	.055	.0013
40	.193	.0938	.134	.0047	.365	.0765	.596	.0011
41	.090	.0796	.078	.0038	.161	.0451	.296	.0011
42	.016	.0090	.006	.0004	.034	.0048	.032	.0012
43	.019	.0075	.010	.0006	.055	.0022	.040	.0007
44	.013	.0084	.010	.0005	.068	.0030	.035	.0008
45	.016	.0079	.011	.0008	.094	.0028	.035	.0009
46	.054	.0288	.022	.0024	.185	.0028	.078	.0011
47	.087	.0634	.024	.0081	.271	.0031	.072	.0010
48	.266	.2529	.046	.0115	.613	.0025	.118	.0012
66	.068	.0120	.023	.0087	.263	.0011	.063	.0011
67	.080	.0444	.017	.0016	.328	.0027	.084	.0011
68	.049	.0215	.012	.0032	.181	.0023	.045	.0007
69	.057	.0487	.014	.0006	.182	.0051	.040	.0011
70	.023	.0141	.013	.0021	.071	.0026	.044	.0011
71	.021	.0199	.012	.0007	.077	.0055	.040	.0009
72	.023	.0099	.010	.0001	.043	.0038	.036	.0001
73	.023	.0067	.014	.0003	.063	.0020	.048	.0010
74	.033	.0025	.016	.0005	.083	.0008	.061	.0011
75	.264	.0690	.271	.0125	.379	.0096	.015	.0006
76	.113	.0654	.060	.0023	.206	.0051	.173	.0005
77	.048	.0160	.031	.0039	.129	.0014	.081	.0011
78	.084	.0490	.011	.0008	.307	.0027	.068	.0011
97	.207	.0581	.050	.0022	.531	.0011	.151	.0014
98	.057	.0209	.018	.0032	.240	.0016	.062	.0011
100	.047	.0230	.014	.0006	.090	.0020	.048	.0013
101	.155	.0505	.098	.0070	.316	.0051	.255	.0012
102	.164	.0754	.028	.0050	.413	.0023	.107	.0014
103	.304	.1039	.070	.0180	.791	.0032	.256	.0007

Source No.8		AC Amplitude				DC Intensity			
Collection Fiber No.	Without GRIN lens Ratio	Without GRIN lens Std.Dev.	With GRIN lens Ratio	With GRIN lens Std.Dev.	Without GRIN lens Ratio	Without GRIN lens Std.Dev.	With GRIN lens Ratio	With GRIN lens Std.Dev.	
5	.010	.0067	.006	.0001	.027	.0061	.020	.0011	
6	.010	.0068	.007	.0003	.023	.0037	.020	.0012	
7	.010	.0082	.008	.0004	.034	.0026	.028	.0009	
8	.017	.0088	.009	.0021	.068	.0023	.033	.0011	
9	.079	.0345	.013	.0014	.186	.0019	.048	.0006	
10	.128	.0747	.038	.0067	.364	.0024	.101	.0012	
12	.339	.0946	.067	.0167	.422	.0009	.206	.0011	
31	.067	.0291	.021	.0016	.181	.0023	.065	.0011	
32	.050	.0383	.009	.0010	.256	.0039	.039	.0011	
33	.027	.0169	.010	.0013	.065	.0026	.035	.0012	
34	.065	.0432	.035	.0011	.114	.0102	.098	.0010	

35	.010	.0088	.006	.0001	.027	.0060	.025	.0012
36	.016	.0080	.011	.0001	.035	.0075	.025	.0011
37	.099	.0511	.039	.0020	.187	.0413	.121	.0012
38	.183	.1383	.160	.0031	.331	.0686	.278	.0011
39	.021	.0128	.016	.0002	.052	.0043	.057	.0015
40	.062	.0279	.043	.0031	.126	.0036	.116	.0012
41	.054	.0306	.025	.0008	.153	.0030	.080	.0011
42	.066	.0323	.019	.0010	.197	.0020	.050	.0010
62	.097	.0341	.068	.0060	.206	.0009	.142	.0011
63	.073	.0260	.026	.0031	.161	.0012	.071	.0011
64	.036	.0136	.011	.0018	.091	.0014	.039	.0014
65	.017	.0080	.007	.0009	.069	.0010	.026	.0007
66	.015	.0057	.007	.0003	.051	.0010	.025	.0012
67	.049	.0285	.020	.0009	.091	.0050	.057	.0011
68	.029	.0130	.014	.0003	.077	.0049	.044	.0013
69	.029	.0329	.019	.0010	.092	.0070	.058	.0010
70	.021	.0128	.017	.0011	.076	.0042	.053	.0011
71	.024	.0160	.016	.0012	.099	.0047	.044	.0011
72	.017	.0061	.014	.0005	.065	.0022	.038	.0011
73	.055	.0094	.029	.0059	.156	.0012	.078	.0012
74	.160	.0553	.045	.0067	.283	.0009	.113	.0013
75	.178	.0257	.103	.0019	.384	.0012	.373	.0029
94	.086	.0244	.046	.0117	.367	.0028	.104	.0014
95	.093	.0363	.049	.0034	.276	.0028	.093	.0014
96	.031	.0091	.019	.0017	.125	.0023	.050	.0014
97	.035	.0115	.028	.0057	.174	.0022	.084	.0017
98	.015	.0050	.009	.0008	.079	.0020	.035	.0020
100	.039	.0211	.016	.0008	.121	.0017	.050	.0012
101	.164	.0621	.066	.0032	.284	.0019	.202	.0014
111	.278	.1412	.050	.0108	.486	.0026	.122	.0015
112	.198	.0636	.074	.0109	.524	.0021	.301	.0013
113	.137	.0886	.022	.0012	.336	.0026	.057	.0012

Source No.9		AC Amplitude				DC Intensity			
Collection Fiber No.	Without GRIN lens Ratio	Without GRIN lens Std.Dev.	With GRIN lens Ratio	With GRIN lens Std.Dev.	Without GRIN lens Ratio	Without GRIN lens Std.Dev.	With GRIN lens Ratio	With GRIN lens Std.Dev.	
27	.037	.0171	.027	.0020	.140	.0818	.073	.0040	
28	.043	.0231	.031	.0008	.098	.0630	.072	.0058	
29	.046	.0137	.035	.0017	.085	.0159	.078	.0026	
30	.047	.0294	.034	.0011	.082	.0663	.084	.0043	
31	.021	.0124	.023	.0014	.074	.0353	.058	.0034	
32	.037	.0284	.020	.0013	.127	.0910	.048	.0030	
33	.027	.0145	.022	.0014	.059	.0380	.055	.0019	

34	.057	.0268	.029	.0009	.127	.0761	.084	.0052
35	.065	.0444	.022	.0053	.116	.0738	.050	.0032
36	.123	.0641	.030	.0026	.234	.1168	.094	.0096
37	.188	.0863	.043	.0045	.406	.1953	.134	.0122
55	.167	.1050	.022	.0055	.283	.1897	.075	.0084
56	.060	.0341	.016	.0067	.188	.0973	.061	.0059
57	.038	.0255	.031	.0021	.144	.0971	.087	.0061
58	.036	.0247	.022	.0016	.075	.0466	.056	.0034
59	.055	.0193	.049	.0023	.115	.0340	.124	.0008
60	.067	.0434	.043	.0021	.129	.0813	.093	.0020
61	.116	.0300	.085	.0008	.237	.0621	.201	.0042
62	.067	.0073	.083	.0011	.131	.0185	.195	.0004
63	.032	.0136	.041	.0014	.072	.0309	.085	.0052
64	.027	.0125	.025	.0008	.048	.0158	.055	.0030
65	.021	.0065	.019	.0006	.055	.0156	.046	.0027
66	.023	.0055	.018	.0016	.101	.0282	.043	.0038
67	.054	.0259	.027	.0013	.173	.0880	.078	.0055
68	.107	.0503	.027	.0061	.206	.1222	.078	.0109
85	.176	.0528	.039	.0049	.491	.1950	.107	.0092
86	.139	.0394	.019	.0020	.187	.0717	.081	.0073
87	.061	.0177	.027	.0051	.203	.0656	.086	.0073
88	.092	.0434	.037	.0023	.156	.0983	.090	.0044
89	.048	.0155	.021	.0019	.091	.0352	.061	.0027
90	.081	.0686	.021	.0008	.084	.0223	.056	.0029
91	.090	.0647	.059	.0012	.158	.1203	.150	.0017
92	.076	.0428	.066	.0005	.149	.0932	.148	.0014
93	.096	.0427	.082	.0022	.207	.0803	.211	.0038
94	.065	.0278	.064	.0003	.138	.0623	.127	.0017
95	.045	.0249	.041	.0002	.092	.0437	.088	.0024
96	.031	.0110	.031	.0011	.063	.0231	.060	.0020
97	.034	.0097	.021	.0008	.078	.0298	.057	.0035
98	.035	.0113	.016	.0032	.120	.0469	.046	.0033
108	.088	.0337	.027	.0085	.287	.0800	.084	.0087
109	.047	.0114	.018	.0009	.132	.0361	.059	.0036
110	.054	.0214	.031	.0012	.097	.0419	.077	.0028
111	.042	.0260	.030	.0011	.078	.0458	.074	.0034
112	.272	.1648	.219	.0056	.463	.3271	.253	.0360
113	.057	.0327	.015	.0026	.205	.1401	.058	.0070

SourceNo.10

AC Amplitude

DC Intensity

Collection Fiber No.	Without GRIN lens		With GRIN lens		Without GRIN lens		With GRIN lens	
	Ratio	Std.Dev.	Ratio	Std.Dev.	Ratio	Std.Dev.	Ratio	Std.Dev.
23	.036	.0277	.009	.0015	.146	.0038	.030	.0010
24	.023	.0163	.009	.0009	.089	.0042	.028	.0012

25	.029	.0226	.014	.0002	.052	.0034	.040	.0012
26	.017	.0097	.009	.0005	.062	.0035	.029	.0015
27	.033	.0178	.021	.0012	.076	.0029	.052	.0016
28	.029	.0177	.013	.0003	.104	.0028	.038	.0011
29	.030	.0064	.012	.0010	.102	.0010	.042	.0009
30	.077	.0430	.019	.0100	.305	.0033	.053	.0011
31	.058	.0228	.019	.0041	.244	.0032	.062	.0013
51	.182	.0530	.032	.0075	.273	.0013	.076	.0013
52	.054	.0269	.015	.0051	.174	.0019	.046	.0013
53	.029	.0145	.009	.0023	.116	.0021	.026	.0011
54	.020	.0133	.006	.0006	.072	.0033	.021	.0012
55	.012	.0076	.006	.0000	.038	.0032	.021	.0012
56	.013	.0108	.010	.0001	.035	.0047	.036	.0011
57	.053	.0410	.069	.0028	.095	.0274	.252	.0012
58	.013	.0096	.007	.0002	.029	.0080	.034	.0015
59	.038	.0127	.032	.0007	.071	.0067	.107	.0012
60	.022	.0126	.009	.0001	.041	.0036	.031	.0011
61	.030	.0079	.008	.0005	.063	.0020	.025	.0012
62	.027	.0076	.012	.0031	.084	.0008	.030	.0011
63	.048	.0207	.014	.0041	.142	.0014	.034	.0009
64	.061	.0307	.029	.0100	.257	.0019	.057	.0008
65	.156	.0504	.022	.0026	.265	.0016	.055	.0013
69	.243	.0582	.051	.0141	2.194	.0026	.362	.0012
70	.330	.1193	.006	.0009	2.182	.0051	.075	.0012
71	.974	.3093	.025	.0044	3.684	.0046	.200	.0012
83	.087	.0318	.023	.0023	.240	.0013	.058	.0011
84	.037	.0161	.018	.0040	.150	.0032	.057	.0014
85	.017	.0071	.006	.0008	.064	.0012	.020	.0012
86	.019	.0069	.008	.0009	.044	.0012	.025	.0011
87	.016	.0051	.006	.0005	.038	.0017	.031	.0011
88	.196	.1111	.077	.0027	.344	.0533	.244	.0010
89	.100	.0375	.025	.0006	.167	.0237	.087	.0012
90	.017	.0041	.008	.0003	.039	.0030	.033	.0011
91	.095	.0655	.049	.0008	.168	.0243	.154	.0013
92	.024	.0114	.011	.0011	.059	.0035	.041	.0011
93	.063	.0244	.012	.0008	.225	.0021	.031	.0012
94	.021	.0087	.009	.0015	.097	.0019	.027	.0012
95	.029	.0121	.015	.0047	.138	.0025	.047	.0011
96	.037	.0115	.020	.0022	.160	.0019	.048	.0012
107	.052	.0168	.010	.0016	.192	.0005	.046	.0016
108	.022	.0084	.007	.0010	.078	.0007	.024	.0006
109	.014	.0062	.006	.0008	.039	.0014	.023	.0009

SourceNo.11		AC Amplitude				DC Intensity			
Collection Fiber No.	Without GRIN lens Ratio	Std.Dev.	With GRIN lens Ratio	Std.Dev.	Without GRIN lens Ratio	Std.Dev.	With GRIN lens Ratio	Std.Dev.	
16	.176	.1168	.024	.0029	.414	.0027	.063	.0011	
17	.091	.0378	.012	.0023	.198	.0022	.044	.0012	
18	.028	.0113	.011	.0026	.083	.0011	.033	.0009	
19	.018	.0028	.008	.0008	.076	.0009	.028	.0011	
20	.015	.0091	.003	.0002	.074	.0038	.012	.0006	
21	.019	.0132	.003	.0005	.050	.0035	.013	.0012	
22	.016	.0134	.003	.0005	.047	.0035	.015	.0011	
23	.023	.0186	.004	.0005	.102	.0048	.017	.0011	
24	.033	.0192	.005	.0006	.125	.0034	.019	.0011	
25	.046	.0273	.006	.0016	.174	.0028	.029	.0012	
26	.080	.0433	.009	.0006	.206	.0021	.034	.0010	
27	.140	.0707	.027	.0055	.433	.0030	.069	.0012	
47	.096	.0669	.019	.0018	.310	.0043	.047	.0011	
48	.070	.0438	.011	.0006	.217	.0045	.035	.0012	
49	.026	.0076	.005	.0004	.071	.0013	.019	.0011	
50	.010	.0031	.004	.0002	.055	.0018	.016	.0015	
51	.010	.0037	.002	.0002	.038	.0022	.012	.0012	
52	.020	.0106	.008	.0002	.036	.0048	.028	.0011	
53	.011	.0061	.002	.0003	.026	.0052	.014	.0010	
54	.009	.0088	.002	.0001	.026	.0079	.015	.0011	
55	.008	.0066	.003	.0004	.022	.0040	.012	.0011	
56	.009	.0076	.003	.0005	.027	.0019	.014	.0014	
57	.029	.0188	.027	.0044	.081	.0045	.072	.0007	
58	.023	.0126	.006	.0008	.117	.0036	.026	.0012	
59	.021	.0077	.015	.0019	.140	.0013	.063	.0011	
60	.094	.0339	.013	.0032	.302	.0027	.049	.0013	
79	.121	.0564	.012	.0004	.372	.0030	.040	.0010	
80	.089	.0566	.010	.0017	.262	.0048	.025	.0011	
81	.023	.0142	.006	.0006	.139	.0035	.024	.0011	
82	.013	.0069	.003	.0004	.048	.0016	.013	.0011	
83	.014	.0067	.004	.0003	.040	.0028	.015	.0012	
84	.013	.0067	.003	.0002	.026	.0042	.015	.0013	
85	.021	.0078	.003	.0001	.037	.0066	.018	.0029	
86	.027	.0103	.010	.0003	.053	.0075	.038	.0014	
87	.012	.0038	.004	.0008	.024	.0020	.019	.0014	
88	.131	.0733	.049	.0023	.194	.0179	.132	.0014	
89	.035	.0138	.010	.0003	.077	.0024	.034	.0017	
90	.019	.0042	.007	.0011	.084	.0006	.028	.0020	
91	.070	.0348	.021	.0036	.169	.0026	.062	.0012	
92	.077	.0393	.019	.0026	.267	.0026	.072	.0014	
105	.042	.0131	.007	.0015	.143	.0018	.026	.0015	

106	.028	.0100	.007	.0010	.110	.0023	.030	.0013
107	.018	.0038	.005	.0006	.061	.0009	.022	.0012

SourceNo.12		AC Amplitude				DC Intensity			
Collection	Without GRIN lens	With GRIN lens	Without GRIN lens	With GRIN lens	Without GRIN lens	With GRIN lens	Without GRIN lens	With GRIN lens	
Fiber No.	Ratio	Std.Dev.	Ratio	Std.Dev.	Ratio	Std.Dev.	Ratio	Std.Dev.	
15	.016	.0097	.005	.0003	.082	.0033	.019	.0012	
16	.016	.0103	.005	.0005	.060	.0029	.019	.0011	
17	.034	.0180	.015	.0008	.059	.0036	.042	.0012	
18	.028	.0103	.012	.0009	.051	.0028	.033	.0031	
19	.021	.0038	.010	.0002	.060	.0011	.028	.0012	
20	.029	.0172	.006	.0007	.096	.0031	.017	.0011	
21	.037	.0257	.009	.0016	.157	.0032	.022	.0011	
22	.086	.0609	.011	.0004	.335	.0047	.048	.0012	
44	.071	.0349	.011	.0009	.229	.0041	.036	.0008	
45	.027	.0131	.006	.0014	.092	.0031	.021	.0010	
46	.046	.0311	.019	.0009	.095	.0052	.048	.0009	
47	.009	.0070	.004	.0002	.026	.0030	.013	.0011	
48	.011	.0090	.004	.0001	.025	.0053	.014	.0013	
49	.015	.0053	.006	.0003	.030	.0046	.021	.0011	
50	.013	.0053	.007	.0003	.030	.0049	.026	.0009	
51	.011	.0048	.005	.0002	.025	.0027	.017	.0011	
52	.018	.0117	.008	.0012	.044	.0037	.024	.0014	
53	.016	.0056	.004	.0003	.061	.0024	.016	.0011	
54	.039	.0272	.005	.0004	.145	.0042	.018	.0012	
55	.048	.0259	.011	.0012	.189	.0033	.032	.0013	
75	.233	.0686	.136	.0084	.276	.0009	.362	.0017	
76	.075	.0308	.022	.0013	.192	.0028	.068	.0011	
77	.036	.0108	.009	.0005	.124	.0018	.024	.0011	
78	.013	.0077	.005	.0007	.068	.0032	.014	.0013	
79	.014	.0077	.005	.0003	.049	.0033	.015	.0012	
80	.014	.0127	.004	.0001	.034	.0054	.016	.0013	
81	.031	.0251	.010	.0004	.057	.0135	.035	.0014	
82	.012	.0042	.006	.0002	.028	.0038	.021	.0014	
83	.015	.0065	.006	.0005	.026	.0029	.020	.0033	
84	.009	.0042	.004	.0005	.032	.0029	.017	.0012	
85	.012	.0033	.004	.0003	.042	.0018	.014	.0014	
86	.025	.0090	.008	.0007	.097	.0013	.026	.0014	
87	.035	.0089	.017	.0008	.178	.0010	.047	.0012	
88.	.105	.0472	.028	.0021	.299	.0040	.080	.0012	
103	.134	.0822	.087	.0056	.393	.0041	.226	.0010	
104	.101	.0549	.028	.0082	.265	.0024	.110	.0013	
105	.014	.0049	.005	.0003	.057	.0018	.017	.0014	
106	.021	.0080	.010	.0012	.088	.0019	.029	.0015	
107	.036	.0064	.013	.0019	.119	.0011	.037	.0010	



108	.070	.0171	.016	.0006	.265	.0002	.059	.0014
119	.056	.0116	.015	.0014	.209	.0009	.048	.0012
120	.164	.0790	.092	.0063	.321	.0035	.237	.0010

Source No.13		AC Amplitude				DC Intensity			
Collection Fiber No.	Without GRIN lens Ratio	Without GRIN lens Std.Dev.	With GRIN lens Ratio	With GRIN lens Std.Dev.	Without GRIN lens Ratio	Without GRIN lens Std.Dev.	With GRIN lens Ratio	With GRIN lens Std.Dev.	
9	.092	.0447	.020	.0032	.311	.0029	.055	.0013	
10	.044	.0226	.016	.0030	.143	.0025	.045	.0011	
11	.044	.0156	.019	.0014	.077	.0022	.051	.0008	
12	.027	.0094	.006	.0005	.049	.0019	.021	.0007	
13	.034	.0200	.008	.0006	.082	.0039	.028	.0010	
14	.018	.0109	.004	.0002	.052	.0042	.017	.0011	
15	.022	.0150	.006	.0006	.047	.0030	.021	.0008	
16	.030	.0197	.007	.0016	.113	.0042	.023	.0011	
17	.038	.0232	.009	.0013	.156	.0026	.039	.0009	
39	.092	.0501	.023	.0026	.256	.0025	.087	.0010	
40	.074	.0199	.036	.0010	.172	.0021	.096	.0010	
41	.059	.0501	.035	.0010	.158	.0042	.086	.0012	
42	.042	.0282	.022	.0012	.079	.0032	.056	.0012	
43	.046	.0159	.024	.0010	.079	.0028	.064	.0013	
44	.035	.0256	.009	.0001	.067	.0114	.031	.0012	
45	.034	.0253	.005	.0002	.058	.0159	.022	.0013	
46	.159	.1163	.066	.0013	.249	.0756	.199	.0011	
47	.016	.0141	.004	.0003	.031	.0070	.019	.0011	
48	.014	.0128	.004	.0004	.037	.0049	.016	.0012	
49	.015	.0040	.004	.0004	.053	.0019	.017	.0007	
50	.030	.0134	.010	.0010	.103	.0019	.030	.0008	
51	.058	.0217	.018	.0067	.192	.0018	.049	.0009	
71	.173	.0996	.033	.0038	.368	.0046	.088	.0011	
72	.046	.0180	.022	.0038	.110	.0024	.060	.0010	
73	.054	.0111	.038	.0032	.133	.0017	.094	.0012	
74	.107	.0082	.063	.0014	.180	.0008	.169	.0011	
75	.430	.1062	.419	.0104	.639	.0370	.209	.0011	
76	.240	.1330	.056	.0012	.371	.0655	.168	.0007	
77	.098	.0360	.010	.0002	.164	.0251	.039	.0011	
78	.029	.0228	.005	.0002	.051	.0140	.021	.0011	
79	.029	.0155	.005	.0001	.046	.0063	.022	.0009	
80	.022	.0200	.003	.0001	.040	.0040	.014	.0001	

81	.028	.0171	.005	.0005	.079	.0037	.020	.0010
82	.021	.0053	.005	.0007	.090	.0016	.020	.0011
83	.026	.0076	.018	.0021	.122	.0015	.047	.0006
84	.089	.0419	.034	.0016	.255	.0028	.082	.0005
103	.185	.1105	.150	.0036	.309	.0145	.237	.0011
104	.068	.0349	.026	.0040	.299	.0040	.107	.0011
105	.036	.0173	.005	.0005	.110	.0021	.025	.0014
106	.076	.0275	.030	.0060	.283	.0028	.077	.0011
118	.051	.0071	.014	.0011	.157	.0005	.047	.0013
119	.032	.0102	.012	.0017	.123	.0013	.050	.0012
120	.218	.0948	.120	.0038	.359	.0044	.273	.0014
121	.063	.0144	.019	.0045	.252	.0010	.057	.0007

Source No.14		AC Amplitude				DC Intensity			
Collection Fiber No.	Without GRIN lens		With GRIN lens		Without GRIN lens		With GRIN lens		
	Ratio	Std.Dev.	Ratio	Std.Dev.	Ratio	Std.Dev.	Ratio	Std.Dev.	
35	.084	.0567	.026	.0013	.227	.0024	.057	.0011	
36	.067	.0365	.017	.0018	.163	.0019	.054	.0012	
37	.050	.0179	.037	.0012	.123	.0024	.082	.0012	
38	.092	.0571	.085	.0024	.137	.0070	.198	.0015	
39	.020	.0142	.009	.0004	.043	.0035	.034	.0016	
40	.116	.0510	.079	.0022	.175	.0198	.127	.0011	
41	.095	.0834	.075	.0026	.145	.0374	.124	.0009	
42	.012	.0078	.008	.0002	.028	.0061	.024	.0011	
43	.027	.0134	.023	.0009	.051	.0035	.033	.0013	
44	.022	.0138	.030	.0008	.054	.0050	.037	.0013	
45	.026	.0164	.026	.0014	.076	.0044	.063	.0013	
46	.057	.0341	.037	.0029	.122	.0036	.085	.0011	
47	.068	.0534	.012	.0004	.199	.0041	.050	.0012	
48	.152	.1104	.028	.0013	.331	.0038	.079	.0012	
66	.111	.0233	.024	.0027	.344	.0012	.065	.0011	
67	.114	.0537	.024	.0032	.318	.0023	.069	.0012	
68	.053	.0245	.016	.0005	.199	.0020	.047	.0015	
69	.059	.0543	.009	.0014	.233	.0048	.032	.0012	
70	.024	.0150	.008	.0022	.090	.0037	.029	.0011	
71	.016	.0108	.007	.0003	.054	.0053	.027	.0012	
72	.014	.0060	.007	.0001	.029	.0043	.025	.0011	
73	.021	.0048	.012	.0001	.038	.0034	.047	.0009	
74	.031	.0032	.023	.0002	.056	.0016	.087	.0008	
75	.444	.1107	.532	.0085	.705	.0666	.257	.0013	
76	.159	.0859	.136	.0043	.227	.0212	.210	.0012	
77	.071	.0248	.052	.0014	.116	.0037	.111	.0012	
78	.037	.0269	.032	.0016	.138	.0042	.079	.0012	
79	.051	.0291	.023	.0009	.282	.0031	.071	.0011	
80	.165	.1129	.022	.0037	.318	.0034	.060	.0014	

97	.143	.0392	.041	.0071	.437	.0011	.126	.0012
98	.048	.0215	.016	.0020	.140	.0011	.048	.0011
99	.221	.0506	.113	.0086	.413	.0013	.340	.0011
100	.030	.0123	.014	.0014	.067	.0032	.046	.0010
101	.253	.1154	.156	.0024	.327	.0181	.147	.0012
102	.051	.0267	.046	.0058	.186	.0035	.122	.0011
103	.128	.0750	.118	.0041	.274	.0039	.201	.0013
115	.065	.0188	.012	.0026	.241	.0010	.069	.0011
116	.122	.0563	.018	.0032	.304	.0025	.081	.0012
117	.110	.0253	.021	.0041	.293	.0009	.084	.0012
118	.037	.0071	.022	.0025	.149	.0007	.062	.0011
119	.048	.0204	.013	.0023	.181	.0014	.054	.0012

Source No.15		AC Amplitude				DC Intensity			
Collection Fiber No.	Without GRIN lens Ratio	Without GRIN lens Std.Dev.	With GRIN lens Ratio	With GRIN lens Std.Dev.	Without GRIN lens Ratio	Without GRIN lens Std.Dev.	With GRIN lens Ratio	With GRIN lens Std.Dev.	
10	.071	.0368	.015	.0027	.214	.0020	.064	.0009	
11	.117	.0429	.035	.0062	.225	.0021	.109	.0010	
32	.253	.2225	.031	.0067	.651	.0043	.069	.0008	
33	.036	.0224	.010	.0004	.106	.0025	.038	.0007	
34	.061	.0319	.031	.0014	.100	.0059	.071	.0010	
35	.011	.0092	.008	.0005	.040	.0053	.026	.0011	
36	.020	.0095	.013	.0002	.038	.0053	.043	.0008	
37	.093	.0455	.112	.0028	.147	.0289	.382	.0011	
38	.335	.2451	.314	.0081	.560	.2038	1.932	.0009	
39	.030	.0177	.018	.0004	.056	.0089	.070	.0010	
40	.089	.0359	.056	.0020	.127	.0089	.142	.0010	
41	.049	.0403	.031	.0009	.107	.0046	.075	.0012	
42	.026	.0132	.012	.0027	.096	.0022	.029	.0012	
43	.056	.0312	.023	.0008	.196	.0013	.061	.0013	
44	.089	.0460	.026	.0049	.317	.0028	.067	.0012	
63	.139	.0506	.042	.0021	.381	.0030	.087	.0013	
64	.061	.0233	.015	.0030	.148	.0016	.054	.0011	
65	.025	.0072	.008	.0005	.079	.0013	.024	.0011	
66	.010	.0026	.007	.0003	.048	.0012	.019	.0012	
67	.053	.0328	.022	.0007	.071	.0060	.056	.0007	
68	.041	.0230	.013	.0003	.072	.0089	.043	.0008	
69	.045	.0504	.029	.0006	.084	.0230	.095	.0009	
70	.025	.0203	.011	.0001	.047	.0117	.042	.0011	
71	.034	.0263	.009	.0006	.046	.0091	.030	.0010	
72	.015	.0055	.008	.0009	.038	.0037	.025	.0012	
73	.017	.0065	.012	.0002	.071	.0014	.037	.0011	

74	.037	.0084	.017	.0006	.144	.0003	.051	.0011
75	.190	.0595	.163	.0088	.325	.0029	.387	.0007
76	.103	.0596	.061	.0038	.267	.0028	.136	.0011
77	.111	.0451	.053	.0079	.404	.0013	.102	.0011
94	.147	.0646	.035	.0023	.313	.0013	.077	.0009
95	.083	.0313	.027	.0042	.223	.0017	.070	.0021
96	.045	.0163	.012	.0012	.139	.0018	.039	.0010
97	.023	.0107	.017	.0020	.093	.0017	.043	.0011
98	.014	.0054	.006	.0004	.045	.0022	.019	.0006
100	.031	.0186	.011	.0004	.065	.0040	.033	.0005
101	.192	.0960	.093	.0023	.305	.0068	.217	.0011
111	.190	.0813	.024	.0060	.538	.0028	.074	.0011
112	.156	.0655	.097	.0055	.493	.0042	.280	.0014
113	.074	.0442	.009	.0035	.171	.0030	.028	.0011
114	.044	.0227	.015	.0011	.188	.0026	.063	.0013
115	.048	.0087	.015	.0025	.191	.0012	.048	.0012
116	.083	.0540	.017	.0048	.333	.0024	.070	.0010
117	.093	.0160	.027	.0033	.473	.0006	.097	.0009

Source No.16		AC Amplitude				DC Intensity			
Collection Fiber No.	Without GRIN lens Ratio	Without GRIN lens Std.Dev.	With GRIN lens Ratio	With GRIN lens Std.Dev.	Without GRIN lens Ratio	Without GRIN lens Std.Dev.	With GRIN lens Ratio	With GRIN lens Std.Dev.	
6	.055	.0335	.018	.0024	.209	.0031	.047	.0011	
7	.092	.0491	.031	.0073	.313	.0020	.081	.0012	
28	.181	.0679	.041	.0065	.413	.0021	.091	.0009	
29	.059	.0151	.029	.0019	.161	.0010	.065	.0011	
30	.041	.0220	.019	.0010	.211	.0035	.050	.0006	
31	.022	.0095	.010	.0014	.071	.0025	.027	.0012	
32	.017	.0128	.011	.0005	.067	.0039	.032	.0011	
33	.033	.0220	.036	.0007	.063	.0154	.105	.0011	
34	.168	.1066	.110	.0026	.267	.0743	.348	.0011	
35	.017	.0147	.018	.0003	.035	.0078	.054	.0012	
36	.018	.0089	.013	.0007	.037	.0032	.034	.0010	
37	.034	.0177	.040	.0014	.079	.0028	.095	.0012	
38	.096	.0613	.075	.0038	.138	.0039	.172	.0011	
39	.056	.0237	.024	.0027	.169	.0023	.056	.0012	
40	.124	.0419	.048	.0117	.288	.0025	.107	.0011	
59	.081	.0241	.045	.0072	.266	.0018	.121	.0015	
60	.037	.0156	.028	.0018	.220	.0034	.054	.0012	
61	.028	.0114	.014	.0010	.091	.0009	.037	.0011	
62	.017	.0044	.015	.0013	.054	.0006	.035	.0010	
63	.013	.0068	.011	.0005	.036	.0019	.030	.0011	
64	.014	.0062	.016	.0004	.025	.0025	.040	.0011	
65	.018	.0051	.027	.0008	.037	.0042	.068	.0014	
66	.020	.0056	.028	.0003	.039	.0042	.072	.0007	

67	.073	.0499	.036	.0009	.115	.0146	.099	.0012
68	.035	.0182	.016	.0005	.069	.0047	.047	.0011
69	.043	.0373	.017	.0014	.126	.0051	.040	.0013
70	.047	.0394	.019	.0009	.150	.0034	.056	.0010
71	.081	.0553	.027	.0041	.242	.0045	.067	.0011
72	.052	.0157	.027	.0035	.161	.0019	.057	.0011
91	.103	.0714	.026	.0028	.373	.0038	.094	.0011
92	.061	.0280	.027	.0045	.241	.0029	.063	.0012
93	.109	.0524	.015	.0017	.396	.0018	.037	.0013
94	.025	.0097	.015	.0010	.059	.0023	.041	.0029
95	.022	.0101	.016	.0007	.042	.0034	.022	.0014
96	.027	.0096	.026	.0007	.044	.0047	.035	.0014
97	.017	.0065	.016	.0011	.047	.0025	.044	.0014
98	.013	.0045	.011	.0014	.046	.0026	.028	.0017
100	.047	.0248	.025	.0050	.137	.0021	.057	.0020
109	.200	.0371	.060	.0048	.610	.0034	.147	.0012
110	.064	.0247	.033	.0009	.273	.0029	.073	.0014
111	.037	.0180	.017	.0022	.140	.0034	.046	.0015
112	.241	.1337	.195	.0068	.386	.0138	.225	.0013
113	.039	.0233	.008	.0011	.228	.0047	.037	.0012
114	.051	.0217	.027	.0020	.191	.0025	.088	.0009

Source No.17		AC Amplitude				DC Intensity			
Collection		Without GRIN lens		With GRIN lens		Without GRIN lens		With GRIN lens	
Fiber No.	Ratio	Std.Dev.	Ratio	Std.Dev.	Ratio	Std.Dev.	Ratio	Std.Dev.	
28	.112	.0605	.038	.0020	.526	.0029	.065	.0011	
29	.059	.0139	.020	.0016	.177	.0009	.045	.0012	
30	.034	.0087	.016	.0010	.187	.0022	.040	.0012	
31	.017	.0078	.008	.0015	.112	.0026	.023	.0015	
32	.039	.0288	.009	.0012	.159	.0036	.022	.0016	
33	.016	.0138	.009	.0003	.048	.0043	.027	.0011	
34	.057	.0323	.035	.0011	.097	.0087	.080	.0009	
35	.015	.0094	.007	.0003	.036	.0028	.019	.0011	
36	.020	.0076	.007	.0000	.060	.0019	.019	.0013	
37	.025	.0083	.035	.0011	.103	.0018	.073	.0013	
38	.088	.0711	.071	.0036	.209	.0034	.127	.0013	
39	.073	.0283	.020	.0035	.249	.0025	.056	.0011	
58	.106	.0572	.021	.0016	.294	.0039	.053	.0012	
59	.036	.0084	.025	.0036	.189	.0015	.059	.0012	
60	.039	.0177	.013	.0017	.123	.0023	.028	.0011	
61	.023	.0055	.011	.0006	.078	.0014	.027	.0012	
62	.012	.0054	.007	.0015	.056	.0010	.020	.0015	
63	.011	.0037	.006	.0012	.037	.0014	.017	.0012	
64	.013	.0059	.005	.0002	.036	.0023	.017	.0011	
65	.012	.0036	.006	.0002	.029	.0032	.025	.0012	

66	.010	.0027	.008	.0043	.023	.0018	.019	.0011
67	.053	.0321	.018	.0002	.108	.0083	.052	.0009
68	.024	.0122	.009	.0002	.059	.0023	.026	.0008
69	.044	.0371	.012	.0009	.161	.0050	.029	.0013
70	.048	.0296	.016	.0021	.169	.0036	.037	.0012
71	.067	.0481	.014	.0028	.261	.0041	.049	.0012
72	.061	.0215	.019	.0037	.154	.0016	.040	.0012
73	.168	.0540	.031	.0058	.488	.0017	.099	.0011
74	.588	.1349	.045	.0017	.768	.0009	.102	.0014
75	.289	.0805	.154	.0289	.659	.0012	.311	.0012
90	.059	.0124	.018	.0061	.187	.0012	.041	.0011
91	.045	.0265	.034	.0011	.143	.0031	.065	.0011
92	.024	.0099	.020	.0031	.114	.0027	.047	.0010
93	.049	.0162	.014	.0003	.236	.0023	.035	.0012
94	.020	.0094	.010	.0006	.040	.0032	.030	.0011
95	.022	.0119	.010	.0004	.046	.0064	.033	.0013
96	.031	.0122	.020	.0005	.055	.0091	.066	.0011
97	.020	.0084	.012	.0002	.037	.0057	.043	.0012
98	.010	.0038	.005	.0001	.025	.0023	.018	.0012
108	.176	.0646	.022	.0046	.432	.0010	.072	.0011
109	.042	.0096	.015	.0012	.190	.0015	.056	.0012
110	.041	.0183	.024	.0002	.100	.0023	.057	.0016
111	.042	.0228	.021	.0018	.083	.0066	.065	.0006
113	.015	.0104	.005	.0006	.064	.0041	.034	.0011
114	.024	.0099	.016	.0027	.067	.0024	.045	.0010
115	.028	.0050	.013	.0012	.106	.0015	.037	.0011
116	.073	.0290	.028	.0016	.257	.0027	.061	.0011
117	.109	.0135	.040	.0046	.439	.0010	.106	.0009
118	.071	.0220	.029	.0022	.297	.0015	.067	.0010
119	.107	.0307	.030	.0061	.294	.0014	.057	.0011
123	.131	.0669	.013	.0027	.281	.0020	.067	.0008
124	.059	.0298	.029	.0037	.232	.0021	.060	.0012
125	.035	.0160	.019	.0017	.251	.0019	.045	.0011
126	.055	.0179	.022	.0039	.165	.0013	.069	.0013
127	.033	.0139	.015	.0008	.096	.0017	.040	.0011
128	.047	.0251	.026	.0007	.178	.0031	.064	.0012

Source No.18 Collection Fiber No.	AC Amplitude				DC Intensity			
	Without GRIN lens		With GRIN lens		Without GRIN lens		With GRIN lens	
Ratio	Std.Dev.	Ratio	Std.Dev.	Ratio	Std.Dev.	Ratio	Std.Dev.	
22	.184	.1259	.024	.0068	.536	.0040	.046	.0012
24	.074	.0412	.010	.0008	.400	.0027	.031	.0011
25	.152	.0886	.010	.0019	.257	.0022	.031	.0008
26	.091	.0530	.015	.0058	.615	.0043	.033	.0007

27	.146	.0544	.022	.0058	.671	.0022	.058	.0010
52	.106	.0401	.021	.0030	.290	.0020	.043	.0011
53	.039	.0194	.007	.0007	.222	.0016	.030	.0008
54	.025	.0169	.006	.0010	.133	.0030	.021	.0011
55	.020	.0128	.006	.0003	.071	.0023	.021	.0009
56	.024	.0185	.007	.0004	.103	.0028	.026	.0010
57	.031	.0231	.013	.0021	.101	.0048	.038	.0010
58	.019	.0103	.006	.0011	.106	.0038	.020	.0012
59	.034	.0108	.009	.0025	.083	.0013	.028	.0012
82	.105	.0333	.016	.0057	.331	.0005	.045	.0013
83	.071	.0223	.013	.0037	.272	.0022	.037	.0012
84	.041	.0170	.008	.0013	.157	.0019	.036	.0013
85	.029	.0090	.007	.0006	.080	.0018	.019	.0011
86	.024	.0068	.008	.0001	.063	.0018	.021	.0011
87	.020	.0078	.011	.0006	.058	.0026	.026	.0012
88	.341	.1904	.036	.0009	.600	.0856	.108	.0007
89	.108	.0380	.022	.0007	.181	.0140	.052	.0008
90	.024	.0068	.011	.0003	.056	.0015	.027	.0009
91	.078	.0595	.014	.0003	.135	.0061	.041	.0011
92	.032	.0166	.011	.0014	.164	.0027	.033	.0010
93	.113	.0474	.010	.0016	.674	.0027	.027	.0012
94	.070	.0232	.010	.0007	.244	.0019	.036	.0011
95	.070	.0251	.021	.0060	.420	.0028	.065	.0011
96	.192	.0769	.021	.0040	.496	.0026	.062	.0007
106	.072	.0282	.011	.0047	.384	.0024	.063	.0011
107	.022	.0052	.009	.0013	.125	.0010	.034	.0011
108	.021	.0026	.014	.0009	.062	.0010	.027	.0009
109	.021	.0063	.016	.0013	.045	.0026	.035	.0011
110	.033	.0146	.013	.0012	.093	.0041	.031	.0010
111	.030	.0207	.009	.0021	.105	.0022	.022	.0011
112	.268	.1263	.053	.0080	.655	.0035	.111	.0006
113	.105	.0649	.014	.0029	.525	.0036	.038	.0005
119	.214	.0337	.025	.0046	.610	.0009	.072	.0011
120	.366	.1446	.027	.0057	.783	.0024	.094	.0011
121	.145	.0241	.028	.0072	.522	.0004	.072	.0014
122	.076	.0162	.016	.0019	.535	.0007	.062	.0011
123	.034	.0165	.011	.0014	.163	.0022	.026	.0013
124	.026	.0105	.011	.0012	.172	.0023	.029	.0012
125	.040	.0121	.010	.0016	.154	.0015	.030	.0014
126	.065	.0309	.012	.0042	.213	.0016	.049	.0008

Source No.19		AC Amplitude				DC Intensity			
Collection Fiber No.	Without GRIN lens Ratio	Without GRIN lens Std.Dev.	With GRIN lens Ratio	With GRIN lens Std.Dev.	Without GRIN lens Ratio	Without GRIN lens Std.Dev.	With GRIN lens Ratio	With GRIN lens Std.Dev.	
19	.060	.0239	.012	.0024	.188	.0013	.046	.0010	

20	.111	.0799	.012	.0014	.500	.0043	.027	.0012
21	.162	.1043	.019	.0013	.654	.0035	.048	.0009
42	.121	.0660	.035	.0144	.353	.0020	.066	.0011
43	.100	.0330	.022	.0012	.275	.0019	.067	.0006
44	.042	.0217	.014	.0014	.169	.0033	.037	.0012
45	.022	.0107	.007	.0004	.092	.0031	.019	.0011
46	.055	.0328	.021	.0019	.120	.0058	.051	.0011
47	.011	.0080	.004	.0009	.046	.0035	.014	.0011
48	.009	.0073	.004	.0002	.036	.0035	.013	.0012
49	.010	.0027	.004	.0001	.034	.0016	.013	.0010
50	.013	.0062	.005	.0003	.045	.0018	.016	.0012
51	.014	.0054	.004	.0008	.070	.0018	.015	.0011
52	.030	.0135	.007	.0007	.106	.0023	.022	.0012
53	.034	.0146	.006	.0010	.168	.0021	.025	.0011
54	.059	.0386	.009	.0029	.360	.0045	.028	.0015
55	.087	.0485	.028	.0033	.359	.0029	.062	.0012
72	.128	.0592	.016	.0046	.251	.0012	.059	.0011
73	.129	.0372	.029	.0011	.403	.0016	.075	.0010
74	.108	.0410	.027	.0024	.298	.0009	.086	.0011
75	.214	.0539	.193	.0079	.271	.0025	.481	.0011
76	.117	.0597	.027	.0021	.162	.0052	.070	.0014
77	.024	.0072	.006	.0008	.069	.0019	.022	.0007
78	.016	.0103	.004	.0007	.040	.0034	.014	.0012
79	.016	.0101	.005	.0003	.041	.0048	.021	.0011
80	.015	.0151	.005	.0003	.037	.0083	.023	.0013
81	.031	.0256	.009	.0002	.062	.0138	.039	.0010
82	.012	.0052	.004	.0002	.028	.0025	.017	.0011
83	.013	.0041	.004	.0001	.041	.0029	.017	.0011
84	.013	.0060	.004	.0004	.046	.0024	.019	.0011
85	.020	.0070	.004	.0009	.062	.0016	.017	.0012
86	.028	.0103	.009	.0007	.122	.0011	.026	.0013
87	.065	.0175	.014	.0011	.228	.0015	.062	.0029
88	.135	.0522	.028	.0084	.333	.0035	.084	.0014
89	.147	.0350	.090	.1175	.358	.0014	.072	.0014
100	.094	.0396	.024	.0051	.326	.0022	.060	.0014
101	.167	.0661	.093	.0096	.353	.0022	.198	.0017
102	.095	.0415	.017	.0037	.295	.0019	.067	.0020
103	.182	.1152	.137	.0039	.347	.0118	.419	.0012
104	.040	.0220	.017	.0007	.121	.0046	.071	.0014
105	.020	.0074	.007	.0005	.044	.0046	.029	.0015
106	.023	.0087	.007	.0014	.061	.0025	.026	.0013
107	.020	.0040	.007	.0005	.103	.0011	.026	.0012
108	.052	.0121	.019	.0017	.254	.0003	.042	.0009
109	.072	.0198	.015	.0015	.436	.0014	.064	.0011
115	.117	.0532	.017	.0016	.386	.0014	.082	.0012



116	.186	.0697	.037	.0021	.610	.0030	.092	.0011
117	.101	.0157	.023	.0025	.375	.0002	.075	.0012
118	.026	.0041	.009	.0006	.149	.0008	.041	.0013
119	.026	.0088	.007	.0020	.090	.0014	.030	.0011
120	.290	.1227	.156	.0036	.492	.0164	.482	.0011
121	.021	.0065	.010	.0012	.090	.0015	.032	.0013
122	.047	.0063	.022	.0013	.164	.0005	.060	.0009
123	.023	.0098	.006	.0009	.175	.0035	.020	.0011
124	.040	.0165	.009	.0009	.200	.0027	.039	.0011
125	.070	.0173	.017	.0063	.258	.0012	.050	.0012

Source No.20		AC Amplitude				DC Intensity			
Collection Fiber No.	Without GRIN lens Ratio	Without GRIN lens Std.Dev.	With GRIN lens Ratio	With GRIN lens Std.Dev.	Without GRIN lens Ratio	Without GRIN lens Std.Dev.	With GRIN lens Ratio	With GRIN lens Std.Dev.	
7	.0662	.022	.0043	.460	.057	.0027	.0462	.0014	
8	.0850	.017	.0061	.494	.05	.0028	.0450	.0011	
9	.1598	.024	.0070	.500	.056	.0008	.0390	.0008	
37	.0381	.031	.0046	.348	.112	.0022	.0381	.0007	
38	.0745	.075	.0040	.286	.189	.003	.0745	.0010	
39	.0124	.007	.0027	.097	.036	.0017	.0124	.0011	
40	.0593	.044	.0015	.199	.135	0.0031	.059	.0008	
41	.0632	.029	.0006	.199	.081	0.0038	.063	.0011	
42	.0255	.013	.0009	.148	.044	0.0026	.025	.0009	
43	.0228	.027	.0050	.220	.073	0.0014	.022	.0010	
44	.0491	.030	.0018	.372	.096	0.0031	.049	.0011	
45	.0693	.023	.0032	.626	.084	0.0045	.069	.0012	
68	.0524	.019	.0033	.441	.058	0.0021	.052	.0012	
69	.1010	.022	.0142	.635	.035	0.0077	.011	.0013	
70	.0284	.009	.0005	.149	.036	0.0034	.028	.0012	
71	.0194	.007	.0017	.068	.026	0.0035	.019	.0013	
72	.0113	.008	.0002	.049	.035	0.0044	.011	.0011	
73	.0092	.013	.0009	.061	.049	0.0016	.009	.0011	
74	.0039	.014	.0001	.117	.058	0.0006	.003	.0012	
75	.0985	.256	.0136	.655	1.006	0.0121	.098	.0007	
76	.0589	.073	.0090	.288	.198	0.0045	.058	.0008	
77	.0351	.033	.0055	.382	.101	0.0016	.035	.0009	
78	.1311	.034	.0069	.803	.093	0.0036	.031	.0011	
98	.0353	.013	.0006	.186	.049	0.0008	.035	.0010	
100	.0211	.017	.0010	.139	.071	0.0068	.021	.0012	
102	.0527	.021	.0020	.307	.130	0.0024	.052	.0011	
103	.1219	.109	.0075	.836	.281	0.0034	.121	.0011	
113	.1476	.024	.0065	.881	.072	0.0024	.147	.0007	
114	.0655	.048	.0051	.667	.192	0.0026	.065	.0011	
115	.0263	.021	.0049	.341	.068	0.0016	.026	.0011	

116	.0471	.028	.0089	.408	.089	0.0027	.047	.0009
117	.0378	.025	.0020	.480	.101	0.0005	.037	.0001
118	.0094	.020	.0051	.276	.065	0.0004	.009	.0010
119	.0245	.025	.0012	.356	.075	0.0014	.024	.0011

Source No.21		AC Amplitude				DC Intensity			
Collection Fiber No.	Without GRIN lens Ratio	Without GRIN lens Std.Dev.	With GRIN lens Ratio	With GRIN lens Std.Dev.	Without GRIN lens Ratio	Without GRIN lens Std.Dev.	With GRIN lens Ratio	With GRIN lens Std.Dev.	
25	.326	.2079	.019	.0020	.404	.0028	.065	.0010	
26	.142	.0772	.017	.0018	.438	.0027	.062	.0009	
27	.229	.1122	.023	.0006	.674	.0057	.067	.0012	
28	.211	.0875	.016	.0050	.372	.0023	.062	.0012	
29	.107	.0513	.021	.0057	.387	.0010	.061	.0011	
30	.148	.0899	.019	.0037	.390	.0030	.062	.0014	
31	.073	.0345	.017	.0036	.272	.0025	.047	.0012	
32	.200	.1476	.016	.0039	.813	.0033	.055	.0011	
33	.053	.0262	.018	.0025	.233	.0038	.044	.0014	
34	.052	.0252	.033	.0064	.234	.0034	.070	.0011	
35	.149	.0993	.016	.0046	.227	.0031	.044	.0011	
54	.115	.0717	.016	.0032	.543	.0050	.046	.0012	
55	.093	.0495	.019	.0019	.232	.0028	.047	.0011	
56	.049	.0223	.012	.0019	.226	.0026	.040	.0012	
57	.055	.0333	.022	.0013	.157	.0039	.061	.0013	
58	.046	.0256	.012	.0022	.152	.0040	.034	.0012	
59	.043	.0115	.025	.0024	.095	.0017	.056	.0012	
60	.032	.0147	.012	.0002	.102	.0025	.033	.0013	
61	.036	.0160	.013	.0017	.117	.0016	.033	.0011	
62	.033	.0081	.013	.0027	.105	.0006	.043	.0015	
63	.042	.0153	.014	.0010	.111	.0017	.033	.0013	
64	.033	.0108	.019	.0019	.118	.0016	.034	.0011	
65	.031	.0072	.013	.0005	.073	.0013	.033	.0012	
66	.023	.0054	.014	.0015	.117	.0015	.036	.0014	
67	.077	.0411	.019	.0023	.223	.0027	.060	.0012	
68	.048	.0212	.015	.0014	.225	.0022	.041	.0007	
69	.248	.1773	.012	.0016	.680	.0067	.043	.0009	
70	.143	.0908	.027	.0025	.504	.0043	.069	.0014	
71	.255	.1394	.026	.0115	.663	.0058	.070	.0012	
72	.125	.0655	.016	.0025	.401	.0025	.052	.0009	
82	.186	.1003	.012	.0059	.401	.0029	.048	.0012	

83	.104	.0450	.017	.0020	.295	.0019	.045	.0013
84	.057	.0237	.015	.0009	.207	.0026	.045	.0012
85	.043	.0165	.010	.0015	.201	.0028	.028	.0004
86	.045	.0105	.011	.0013	.110	.0012	.033	.0011
87	.029	.0081	.013	.0044	.111	.0013	.038	.0012
88	.077	.0341	.038	.0057	.187	.0059	.086	.0014
89	.040	.0141	.015	.0008	.079	.0022	.043	.0011
90	.028	.0075	.015	.0003	.071	.0013	.039	.0013
91	.072	.0508	.037	.0008	.118	.0072	.099	.0014
92	.047	.0216	.024	.0007	.098	.0051	.073	.0012
93	.047	.0172	.021	.0005	.119	.0019	.057	.0006
94	.036	.0177	.019	.0012	.066	.0043	.050	.0008
95	.034	.0196	.020	.0008	.081	.0043	.052	.0012
96	.032	.0107	.019	.0011	.076	.0027	.046	.0013
97	.026	.0085	.020	.0010	.068	.0043	.054	.0012
98	.028	.0109	.010	.0011	.063	.0022	.028	.0011
100	.059	.0200	.013	.0011	.192	.0029	.055	.0013
101	.199	.0694	.058	.0107	.453	.0035	.198	.0007
105	.073	.0211	.008	.0011	.353	.0018	.041	.0006
106	.091	.0295	.013	.0027	.262	.0021	.053	.0012
107	.038	.0148	.009	.0029	.145	.0013	.035	.0012
108	.023	.0065	.009	.0008	.080	.0013	.029	.0012
109	.023	.0074	.010	.0005	.043	.0019	.036	.0008
110	.061	.0285	.043	.0016	.106	.0158	.144	.0024
111	.076	.0477	.050	.0012	.129	.0306	.167	.0029
112	.480	.2791	.350	.0110	.866	.1158	.538	.0079
113	.017	.0159	.007	.0005	.049	.0061	.032	.0005
114	.024	.0128	.015	.0041	.066	.0035	.053	.0011
115	.021	.0056	.011	.0004	.095	.0016	.042	.0013
116	.048	.0191	.011	.0007	.172	.0025	.043	.0013
117	.069	.0110	.013	.0025	.260	.0011	.051	.0012
118	.039	.0146	.011	.0020	.121	.0002	.038	.0011
119	.025	.0051	.007	.0021	.128	.0013	.042	.0011
120	.196	.0774	.060	.0031	.382	.0054	.233	.0038
121	.037	.0099	.011	.0040	.161	.0007	.073	.0006
122	.066	.0103	.013	.0023	.192	.0006	.128	.0013
123	.020	.0091	.005	.0004	.085	.0032	.026	.0012
124	.020	.0110	.008	.0001	.043	.0024	.032	.0013
125	.040	.0110	.015	.0002	.083	.0044	.055	.0014
126	.075	.0260	.038	.0023	.134	.0102	.116	.0019
127	.034	.0133	.016	.0001	.064	.0077	.064	.0004
128	.054	.0296	.025	.0010	.113	.0067	.088	.0014

Source No.22		AC Amplitude				DC Intensity			
Collection Fiber No.	Without GRIN lens Ratio	Std.Dev.	With GRIN lens Ratio	Std.Dev.	Without GRIN lens Ratio	Std.Dev.	With GRIN lens Ratio	Std.Dev.	
46	.078	.0436	.024	.0041	.401	.0024	.055	.0013	
47	.063	.0397	.012	.0022	.248	.0048	.024	.0011	
48	.064	.0455	.009	.0022	.216	.0038	.021	.0008	
49	.034	.0104	.010	.0025	.120	.0015	.015	.0007	
50	.033	.0135	.008	.0011	.102	.0015	.015	.0010	
51	.036	.0154	.009	.0013	.117	.0024	.013	.0011	
52	.034	.0147	.008	.0014	.137	.0037	.015	.0008	
53	.027	.0158	.007	.0005	.117	.0025	.013	.0011	
54	.040	.0255	.006	.0007	.161	.0042	.011	.0009	
55	.032	.0215	.007	.0009	.163	.0037	.014	.0010	
56	.080	.0619	.009	.0017	.170	.0023	.022	.0010	
57	.044	.0251	.025	.0065	.235	.0036	.045	.0012	
58	.085	.0524	.012	.0021	.243	.0032	.029	.0012	
59	.066	.0259	.028	.0011	.243	.0015	.054	.0013	
60	.131	.0500	.026	.0069	.456	.0031	.041	.0012	
76	.075	.0304	.021	.0038	.438	.0027	.054	.0013	
77	.049	.0181	.014	.0011	.172	.0010	.026	.0011	
78	.049	.0283	.008	.0007	.198	.0028	.016	.0011	
79	.031	.0171	.008	.0017	.166	.0028	.018	.0012	
80	.026	.0181	.004	.0018	.155	.0048	.011	.0007	
81	.020	.0138	.008	.0013	.107	.0043	.011	.0008	
82	.013	.0040	.003	.0003	.047	.0016	.007	.0009	
83	.016	.0064	.005	.0008	.051	.0026	.008	.0011	
84	.012	.0065	.005	.0003	.044	.0037	.009	.0010	
85	.011	.0044	.005	.0003	.044	.0026	.007	.0012	
86	.014	.0031	.008	.0013	.051	.0022	.012	.0011	
87	.012	.0039	.008	.0011	.049	.0013	.012	.0011	
88	.091	.0516	.053	.0026	.161	.0066	.058	.0007	
89	.035	.0131	.014	.0009	.115	.0019	.021	.0011	
90	.028	.0050	.009	.0007	.148	.0010	.019	.0011	
91	.057	.0310	.035	.0047	.241	.0038	.047	.0009	
97	.072	.0188	.020	.0030	.237	.0019	.035	.0001	
98	.055	.0204	.018	.0033	.217	.0017	.030	.0010	
100	.082	.0323	.024	.0053	.229	.0021	.039	.0011	
101	.179	.0825	.094	.0109	.505	.0039	.132	.0006	
103	.156	.0843	.133	.0066	.368	.0055	.163	.0005	
105	.013	.0038	.008	.0005	.054	.0030	.009	.0011	
106	.029	.0123	.012	.0010	.060	.0062	.015	.0011	
107	.015	.0028	.010	.0010	.036	.0022	.012	.0014	
108	.014	.0029	.008	.0006	.043	.0014	.011	.0011	
109	.011	.0029	.005	.0015	.037	.0015	.010	.0013	

110	.027	.0132	.016	.0024	.082	.0022	.027	.0012
111	.039	.0179	.016	.0047	.141	.0033	.025	.0014
112	.220	.1117	.162	.0090	.439	.0023	.196	.0007
113	.040	.0238	.006	.0004	.150	.0034	.012	.0012
114	.031	.0136	.010	.0008	.144	.0026	.027	.0011
115	.050	.0096	.019	.0029	.178	.0012	.028	.0012
118	.023	.0027	.017	.0014	.093	.0003	.022	.0012
119	.020	.0048	.011	.0012	.073	.0015	.018	.0012
120	.370	.1702	.339	.0065	.627	.0392	.296	.0015
121	.021	.0049	.014	.0004	.056	.0021	.020	.0004
122	.125	.0104	.088	.0016	.214	.0045	.069	.0010
123	.014	.0084	.011	.0002	.034	.0061	.012	.0011
124	.012	.0058	.010	.0009	.037	.0044	.012	.0010
125	.031	.0077	.016	.0011	.066	.0030	.018	.0011
126	.040	.0178	.024	.0049	.089	.0019	.029	.0006
127	.023	.0082	.012	.0024	.089	.0014	.029	.0012
128	.086	.0411	.017	.0020	.357	.0025	.038	.0013

Source No.23		AC Amplitude				DC Intensity			
Collection Fiber No.	Without GRIN lens		With GRIN lens		Without GRIN lens		With GRIN lens		
	Ratio	Std.Dev.	Ratio	Std.Dev.	Ratio	Std.Dev.	Ratio	Std.Dev.	
12	0.118	0.0449	0.032	0.0050	0.337	0.0017	0.060	0.0011	
14	0.100	0.0554	0.018	0.0014	0.356	0.0025	0.035	0.0011	
38	0.105	0.0510	0.076	0.0066	0.305	0.0031	0.118	0.0013	
39	0.097	0.0558	0.025	0.0021	0.216	0.0021	0.035	0.0011	
40	0.045	0.0243	0.055	0.0068	0.177	0.0022	0.070	0.0014	
41	0.071	0.0469	0.044	0.0025	0.234	0.0037	0.059	0.0012	
42	0.035	0.0172	0.032	0.0022	0.127	0.0027	0.044	0.0011	
43	0.044	0.0140	0.048	0.0031	0.139	0.0013	0.064	0.0006	
44	0.042	0.0226	0.031	0.0021	0.128	0.0034	0.045	0.0014	
45	0.033	0.0177	0.019	0.0013	0.109	0.0037	0.029	0.0012	
46	0.054	0.0442	0.032	0.0027	0.136	0.0038	0.046	0.0013	
47	0.024	0.0173	0.010	0.0015	0.146	0.0046	0.020	0.0012	
48	0.114	0.1150	0.016	0.0041	0.179	0.0047	0.022	0.0011	
49	0.031	0.0126	0.011	0.0009	0.210	0.0015	0.025	0.0011	
70	0.073	0.0446	0.020	0.0040	0.256	0.0035	0.033	0.0012	
71	0.044	0.0280	0.015	0.0005	0.202	0.0049	0.028	0.0011	
72	0.023	0.0086	0.012	0.0003	0.065	0.0024	0.020	0.0012	
73	0.025	0.0069	0.022	0.0012	0.094	0.0016	0.031	0.0012	
74	0.048	0.0106	0.032	0.0030	0.119	0.0006	0.050	0.0006	
75	0.313	0.0754	0.395	0.0062	0.504	0.0160	0.536	0.0045	
76	0.132	0.0772	0.061	0.0016	0.218	0.0161	0.085	0.0012	
77	0.037	0.0124	0.017	0.0003	0.076	0.0036	0.024	0.0012	
78	0.016	0.0094	0.008	0.0003	0.051	0.0038	0.014	0.0009	

79	0.019	0.0099	0.008	0.0002	0.072	0.0031	0.014	0.0007
80	0.026	0.0186	0.007	0.0011	0.092	0.0042	0.013	0.0008
81	0.026	0.0156	0.009	0.0018	0.119	0.0037	0.018	0.0010
82	0.023	0.0054	0.007	0.0009	0.114	0.0018	0.014	0.0010
83	0.043	0.0132	0.012	0.0013	0.157	0.0018	0.020	0.0011
97	0.052	0.0140	0.022	0.0038	0.241	0.0024	0.037	0.0011
98	0.031	0.0101	0.009	0.0006	0.120	0.0020	0.022	0.0012
99	0.199	0.0302	0.055	0.0070	0.463	0.0005	0.080	0.0022
100	0.027	0.0125	0.014	0.0008	0.073	0.0035	0.033	0.0012
101	0.348	0.1478	0.246	0.0051	0.594	0.0505	0.310	0.0025
102	0.019	0.0118	0.017	0.0015	0.063	0.0047	0.050	0.0007
104	0.024	0.0133	0.027	0.0020	0.135	0.0053	0.043	0.0012
105	0.016	0.0084	0.007	0.0003	0.049	0.0017	0.012	0.0010
106	0.039	0.0151	0.015	0.0020	0.157	0.0023	0.024	0.0012
107	0.059	0.0113	0.015	0.0029	0.234	0.0012	0.029	0.0011
108	0.091	0.0276	0.022	0.0085	0.293	0.0008	0.038	0.0012
109	0.090	0.0373	0.018	0.0030	0.267	0.0018	0.050	0.0007
110	0.066	0.0218	0.040	0.0090	0.330	0.0023	0.067	0.0014
111	0.087	0.0417	0.018	0.0034	0.319	0.0027	0.044	0.0007
112	0.205	0.0834	0.249	0.0594	0.707	0.0051	0.306	0.0067
113	0.023	0.0152	0.016	0.0019	0.120	0.0038	0.027	0.0014
114	0.078	0.0088	0.072	0.0059	0.197	0.0025	0.178	0.0038
115	0.015	0.0041	0.012	0.0008	0.081	0.0016	0.023	0.0013
116	0.018	0.0079	0.011	0.0008	0.073	0.0026	0.020	0.0012
117	0.016	0.0026	0.015	0.0004	0.058	0.0011	0.023	0.0011
118	0.033	0.0026	0.029	0.0006	0.064	0.0021	0.039	0.0016
119	0.019	0.0050	0.016	0.0004	0.041	0.0041	0.027	0.0005
121	0.026	0.0042	0.015	0.0011	0.069	0.0021	0.034	0.0014
122	0.056	0.0075	0.031	0.0017	0.139	0.0011	0.049	0.0013
123	0.019	0.0091	0.008	0.0014	0.077	0.0024	0.015	0.0012
124	0.018	0.0113	0.009	0.0004	0.124	0.0031	0.017	0.0011
125	0.024	0.0043	0.010	0.0043	0.172	0.0012	0.034	0.0006
126	0.059	0.0158	0.022	0.0033	0.280	0.0027	0.047	0.0008
127	0.050	0.0271	0.044	0.0097	0.183	0.0019	0.136	0.0011
128	0.150	0.0735	0.030	0.0088	0.564	0.0034	0.060	0.0015

Source No.24		AC Amplitude				DC Intensity			
Collection Fiber No.	Without GRIN lens Ratio	Without GRIN lens Std.Dev.	With GRIN lens Ratio	With GRIN lens Std.Dev.	Without GRIN lens Ratio	Without GRIN lens Std.Dev.	With GRIN lens Ratio	With GRIN lens Std.Dev.	
33	.042	.0196	.010	.0008	.139	.0034	.024	.0011	
34	.056	.0278	.028	.0013	.128	.0034	.045	.0012	
35	.030	.0238	.007	.0006	.079	.0031	.016	.0009	
36	.025	.0126	.008	.0007	.080	.0021	.016	.0011	

37	.034	.0164	.025	.0012	.100	.0024	.057	.0006
38	.094	.0475	.074	.0012	.153	.0044	.121	.0012
39	.028	.0125	.012	.0020	.091	.0023	.021	.0011
40	.065	.0286	.040	.0040	.165	.0025	.063	.0011
41	.063	.0400	.026	.0013	.284	.0045	.047	.0011
63	.071	.0243	.017	.0035	.277	.0020	.026	.0012
64	.033	.0105	.013	.0006	.180	.0019	.025	.0010
65	.015	.0046	.005	.0010	.062	.0013	.012	.0012
66	.010	.0032	.004	.0009	.034	.0009	.011	.0011
67	.043	.0239	.017	.0024	.091	.0049	.030	.0012
68	.018	.0085	.012	.0004	.058	.0032	.024	.0011
69	.027	.0279	.013	.0014	.096	.0064	.023	.0015
70	.016	.0103	.007	.0008	.063	.0041	.017	.0012
71	.017	.0122	.005	.0009	.063	.0040	.014	.0011
72	.014	.0056	.005	.0002	.044	.0020	.012	.0010
73	.019	.0073	.010	.0005	.097	.0011	.023	.0011
74	.042	.0106	.014	.0041	.121	.0004	.030	.0011
75	.213	.0456	.201	.0035	.297	.0021	.323	.0014
76	.098	.0493	.051	.0067	.220	.0035	.080	.0007
77	.063	.0171	.025	.0052	.257	.0017	.039	.0012
78	.154	.0681	.013	.0057	.382	.0033	.030	.0011
93	.348	.1731	.019	.0015	.690	.0018	.033	.0013
94	.034	.0129	.011	.0004	.128	.0020	.024	.0010
95	.025	.0151	.013	.0021	.124	.0025	.021	.0011
96	.023	.0089	.010	.0003	.079	.0020	.022	.0011
97	.012	.0053	.007	.0002	.035	.0025	.015	.0011
98	.008	.0027	.005	.0001	.023	.0033	.011	.0012
100	.040	.0208	.013	.0003	.069	.0092	.026	.0013
101	.283	.1172	.145	.0028	.433	.0234	.264	.0029
102	.043	.0209	.014	.0012	.230	.0026	.044	.0014
109	.056	.0168	.017	.0052	.209	.0019	.022	.0014
110	.034	.0137	.020	.0039	.214	.0029	.030	.0014
111	.037	.0183	.012	.0010	.099	.0030	.030	.0017
112	.296	.1786	.205	.0044	.483	.0179	.388	.0020
113	.010	.0076	.003	.0002	.026	.0038	.010	.0012
114	.016	.0092	.008	.0004	.039	.0059	.019	.0014
115	.017	.0064	.017	.0005	.043	.0034	.034	.0015
116	.015	.0076	.008	.0004	.053	.0041	.019	.0013
117	.011	.0022	.008	.0009	.060	.0006	.022	.0012
118	.016	.0027	.012	.0018	.053	.0007	.024	.0009
119	.013	.0032	.008	.0013	.072	.0012	.019	.0011
120	.243	.0954	.130	.0078	.418	.0082	.231	.0012
121	.038	.0087	.014	.0017	.228	.0014	.032	.0011
122	.089	.0272	.018	.0040	.281	.0003	.059	.0012
123	.055	.0248	.007	.0004	.149	.0025	.018	.0013

124	.030	.0173	.011	.0039	.148	.0023	.021	.0011
125	.022	.0087	.009	.0013	.138	.0017	.025	.0011
126	.039	.0141	.017	.0028	.147	.0016	.035	.0013
127	.018	.0083	.008	.0018	.072	.0019	.020	.0009
128	.033	.0198	.015	.0008	.155	.0039	.033	.0014

Source No.25		AC Amplitude				DC Intensity			
Collection Fiber No.	Without GRIN lens Ratio	Without GRIN lens Std.Dev.	With GRIN lens Ratio	With GRIN lens Std.Dev.	Without GRIN lens Ratio	Without GRIN lens Std.Dev.	With GRIN lens Ratio	With GRIN lens Std.Dev.	
34	.341	.1743	.101	.0096	.447	.0031	.101	.0011	
35	.259	.1738	.045	.0134	.545	.0045	.068	.0012	
36	.226	.0708	.080	.0072	.545	.0010	.070	.0012	
37	.204	.0675	.068	.0094	.611	.0009	.116	.0015	
38	.238	.1482	.077	.0180	.740	.0037	.163	.0016	
39	.143	.0759	.037	.0127	.432	.0020	.066	.0011	
40	.248	.0922	.053	.0070	.390	.0015	.075	.0009	
41	.383	.2022	.064	.0117	.550	.0027	.072	.0011	
42	.155	.0666	.043	.0137	.495	.0031	.066	.0013	
43	.111	.0363	.064	.0028	.400	.0010	.104	.0013	
44	.114	.0543	.033	.0060	.363	.0030	.054	.0013	
45	.064	.0344	.017	.0049	.219	.0025	.039	.0011	
46	.092	.0519	.037	.0072	.297	.0034	.061	.0012	
47	.082	.0500	.019	.0061	.233	.0037	.036	.0012	
48	.087	.0469	.013	.0031	.274	.0035	.037	.0011	
49	.062	.0220	.016	.0045	.220	.0013	.039	.0012	
50	.112	.0436	.015	.0017	.207	.0011	.047	.0015	
51	.136	.0615	.022	.0025	.320	.0021	.046	.0012	
52	.157	.0815	.026	.0017	.393	.0029	.036	.0011	
53	.091	.0393	.022	.0023	.358	.0019	.047	.0012	
54	.142	.0946	.025	.0044	.461	.0031	.037	.0011	
55	.124	.0652	.026	.0083	.435	.0033	.037	.0009	
56	.163	.0807	.032	.0050	.505	.0033	.064	.0008	
57	.134	.0753	.050	.0050	.561	.0040	.079	.0013	
58	.247	.1618	.034	.0122	.492	.0030	.060	.0012	
59	.172	.0466	.042	.0112	.333	.0018	.104	.0012	
60	.166	.1270	.037	.0040	.587	.0027	.061	.0012	
61	.219	.1063	.050	.0112	.483	.0013	.079	.0011	
62	.284	.0221	.053	.0026	.545	.0009	.087	.0014	
63	.389	.1270	.076	.0153	.682	.0019	.089	.0012	
64	.236	.0980	.060	.0117	.718	.0017	.079	.0011	
65	.102	.0292	.017	.0029	.257	.0011	.040	.0011	



66	.111	.0259	.024	.0040	.463	.0019	.033	.0010
67	.143	.0736	.047	.0135	.417	.0030	.060	.0012
68	.112	.0662	.034	.0155	.430	.0028	.062	.0011
69	.176	.1487	.032	.0051	.728	.0074	.047	.0013
70	.148	.1051	.036	.0094	.452	.0046	.056	.0011
71	.102	.0652	.016	.0015	.442	.0043	.048	.0012
72	.053	.0316	.015	.0018	.141	.0019	.028	.0012
73	.054	.0120	.027	.0033	.256	.0013	.051	.0011
74	.102	.0180	.025	.0028	.398	.0004	.060	.0012
75	.234	.0585	.233	.0205	.377	.0038	.364	.0016
76	.100	.0525	.034	.0021	.185	.0029	.076	.0006
77	.044	.0123	.017	.0063	.161	.0018	.030	.0011
78	.054	.0318	.009	.0015	.168	.0035	.023	.0010
79	.042	.0247	.009	.0026	.158	.0027	.022	.0011
80	.040	.0281	.007	.0018	.134	.0030	.019	.0011
81	.036	.0212	.012	.0026	.177	.0038	.023	.0009
82	.024	.0088	.007	.0007	.112	.0015	.017	.0010
83	.019	.0084	.007	.0016	.114	.0023	.024	.0011
84	.027	.0123	.006	.0002	.104	.0023	.026	.0008
85	.023	.0082	.007	.0013	.097	.0015	.018	.0012
86	.035	.0101	.010	.0036	.140	.0017	.027	.0011
87	.039	.0101	.013	.0044	.134	.0010	.036	.0013
88	.078	.0487	.030	.0022	.183	.0025	.065	.0011
89	.063	.0272	.014	.0052	.207	.0014	.039	.0012
90	.062	.0134	.011	.0023	.215	.0006	.042	.0012
91	.150	.0907	.042	.0071	.378	.0035	.079	.0011
92	.131	.0519	.032	.0048	.419	.0040	.053	.0011
94	.068	.0298	.019	.0006	.336	.0025	.038	.0013
95	.101	.0422	.028	.0024	.335	.0029	.051	.0011
96	.119	.0437	.032	.0023	.277	.0027	.038	.0009
97	.035	.0104	.017	.0036	.119	.0017	.035	.0010
98	.026	.0081	.007	.0009	.094	.0020	.021	.0001
100	.020	.0090	.011	.0022	.108	.0029	.034	.0014
101	.253	.1067	.120	.0011	.317	.0069	.237	.0016
102	.054	.0227	.017	.0038	.278	.0041	.045	.0012
103	.176	.1119	.159	.0030	.311	.0079	.308	.0011
104	.050	.0270	.028	.0033	.239	.0035	.068	.0013
105	.016	.0052	.007	.0003	.064	.0024	.019	.0011
106	.018	.0056	.009	.0010	.092	.0025	.027	.0011
107	.019	.0031	.006	.0002	.082	.0013	.018	.0012
108	.020	.0048	.007	.0003	.083	.0010	.024	.0012
109	.024	.0052	.006	.0016	.069	.0011	.024	.0014
110	.029	.0124	.009	.0037	.116	.0024	.056	.0012
111	.022	.0100	.010	.0015	.110	.0029	.038	.0016
112	.154	.0726	.094	.0065	.433	.0071	.294	.0014

113	.014	.0083	.005	.0010	.059	.0040	.014	.0012
114	.018	.0106	.008	.0014	.058	.0026	.025	.0013
115	.011	.0032	.010	.0003	.063	.0016	.028	.0011
116	.017	.0079	.011	.0012	.077	.0025	.026	.0011
117	.017	.0038	.013	.0007	.070	.0007	.031	.0012
118	.028	.0033	.022	.0006	.061	.0009	.043	.0014
119	.023	.0064	.017	.0007	.052	.0039	.042	.0015
121	.029	.0076	.022	.0004	.060	.0040	.053	.0017
122	.136	.0131	.073	.0018	.238	.0045	.132	.0008
123	.014	.0085	.009	.0001	.042	.0053	.022	.0011
124	.014	.0078	.008	.0003	.039	.0036	.022	.0012
125	.028	.0097	.015	.0003	.065	.0027	.035	.0012
126	.037	.0133	.020	.0015	.087	.0025	.052	.0010
127	.016	.0058	.022	.0037	.055	.0019	.041	.0018
128	.042	.0192	.016	.0020	.151	.0022	.048	.0015

Source No.26		AC Amplitude				DC Intensity			
Collection Fiber No.	Without GRIN lens Ratio	Std.Dev.	With GRIN lens Ratio	Std.Dev.	Without GRIN lens Ratio	Std.Dev.	With GRIN lens Ratio	Std.Dev.	
72	.032	.0154	.017	.0028	.140	.0015	.023	.0011	
73	.054	.0125	.032	.0018	.309	.0009	.049	.0011	
74	.084	.0167	.037	.0037	.322	.0002	.056	.0012	
75	.269	.0815	.216	.0188	.520	.0021	.477	.0031	
76	.136	.0535	.059	.0029	.278	.0032	.083	.0012	
77	.064	.0207	.020	.0008	.250	.0020	.040	.0011	
78	.102	.0660	.021	.0049	.317	.0032	.029	.0011	
79	.122	.0611	.023	.0066	.366	.0027	.035	.0012	
80	.130	.0909	.019	.0030	.423	.0048	.027	.0008	
82	.048	.0135	.013	.0033	.253	.0014	.022	.0010	
83	.052	.0185	.025	.0046	.264	.0028	.032	.0009	
84	.053	.0218	.027	.0095	.245	.0019	.042	.0011	
85	.047	.0157	.021	.0078	.243	.0021	.030	.0013	
86	.047	.0129	.025	.0055	.243	.0018	.038	.0011	
94	.061	.0184	.024	.0024	.206	.0028	.041	.0009	
95	.072	.0514	.029	.0076	.277	.0030	.044	.0011	
96	.046	.0163	.029	.0040	.209	.0020	.043	.0014	
97	.017	.0047	.014	.0026	.084	.0018	.030	.0011	
98	.014	.0056	.009	.0007	.061	.0018	.020	.0012	
100	.037	.0221	.018	.0040	.085	.0022	.032	.0013	
101	.277	.1061	.210	.0088	.498	.0117	.281	.0017	
105	.019	.0047	.011	.0019	.108	.0016	.021	.0011	
106	.045	.0144	.014	.0014	.220	.0020	.035	.0011	
107	.034	.0054	.008	.0020	.141	.0007	.024	.0013	
108	.043	.0168	.010	.0011	.129	.0005	.025	.0012	

109	.021	.0047	.009	.0020	.100	.0013	.021	.0013
110	.033	.0156	.027	.0037	.097	.0019	.049	.0014
111	.028	.0151	.019	.0006	.095	.0032	.036	.0014
112	.329	.1851	.245	.0221	.528	.0099	.490	.0033
113	.010	.0097	.005	.0003	.035	.0039	.013	.0012
114	.016	.0097	.010	.0020	.046	.0033	.023	.0014
115	.015	.0043	.011	.0010	.050	.0015	.029	.0014
116	.016	.0074	.010	.0021	.076	.0030	.024	.0012
117	.016	.0060	.011	.0007	.093	.0010	.032	.0012
118	.033	.0022	.023	.0002	.069	.0011	.040	.0010
119	.022	.0071	.013	.0005	.042	.0015	.030	.0013
121	.028	.0049	.014	.0013	.076	.0016	.034	.0014
122	.092	.0077	.051	.0010	.179	.0010	.083	.0015
123	.009	.0050	.006	.0003	.050	.0035	.016	.0010
124	.013	.0079	.007	.0005	.058	.0035	.018	.0014
125	.041	.0103	.017	.0007	.085	.0028	.032	.0012
126	.055	.0174	.036	.0026	.138	.0039	.066	.0011
127	.018	.0077	.011	.0003	.060	.0023	.034	.0011
128	.038	.0202	.026	.0022	.168	.0039	.051	.0080

---

## APPENDIX F

### RAYLEIGH RESOLUTION

Two targets are considered resolved if the image satisfies Rayleigh's criterion<sup>53</sup> as shown in Figure A-5. Rayleigh's criterion requires that the height of the image intensity dip at least 19% between the asperities. In other words, to determine the lateral resolution of targets experimentally, the targets are brought closer and closer together until the image no longer dips by 19% between peaks. In the future studies, we will check if tomographically reconstructed targets can be distinguished as a function of separation distance between targets.

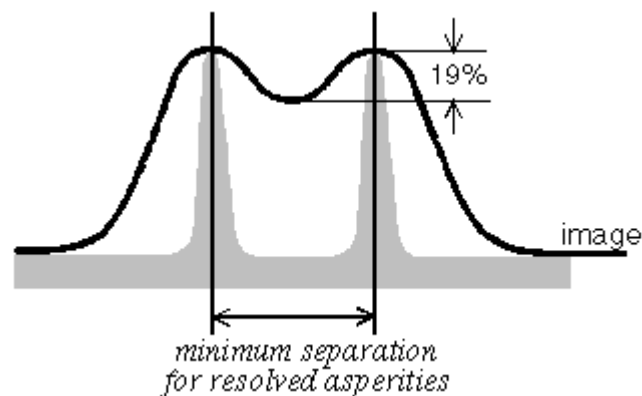


Figure A5 Definition of lateral resolution using Rayleigh's criterion<sup>53</sup>.

## VITA

Kil Dong Hwang was born in Kyunggi, Korea on August 31, 1972. He joined the Department of Chemical Engineering at Chung-Ang University, Seoul, Korea and graduated with honors receiving a Bachelor of Science degree in chemical engineering in February 1998. Kil Dong won the honorable mention at the “Contest of Transport Phenomena for University Students” sponsored by the Korean Institute of Chemical Engineers in 1996. From 1999 to 2001, he worked for the Korea Chemical Company (Research Institute) as a research engineer. Currently, he is working at the Photon Migration Laboratory, Baylor College of Medicine, Houston, Texas, as a researcher. He received his Ph.D. in Chemical engineering from Texas A&M University in December 2006.

Kil Dong Hwang’s permanent address is as follows.

507 Gaybar Avenue

West Covina, CA 91790

The typist for this dissertation was Kil Dong Hwang.